STAR FORMATION AND GALAXY EVOLUTION IN DIFFERENT ENVIRONMENTS, FROM THE FIELD TO MASSIVE CLUSTERS

by

Krystal Tyler

A Dissertation Submitted to the Faculty of the

DEPARTMENT OF ASTRONOMY

In Partial Fulfillment of the Requirements
For the Degree of

DOCTOR OF PHILOSOPHY

In the Graduate College

THE UNIVERSITY OF ARIZONA

2 0 1 2

THE UNIVERSITY OF ARIZONA
GRADUATE COLLEGE

As members of the Dissertation Committee, we certify that we have read the dissertation prepared by Krystal Tyler entitled "Star Formation and Galaxy Evolution in Different Environments, from the Field to Massive Clusters" and recommend that it be accepted as fulfilling the dissertation requirement for the Degree of Doctor of Philosophy.

_____ Date: 16 Nov. 2012
George H. Rieke

_____ Date: 16 Nov. 2012
Dennis Zaritsky

_____ Date: 16 Nov. 2012
Eiichi Egami

_____ Date: 16 Nov. 2012
Edward W. Olszewski

_____ Date: 16 Nov. 2012
Daniel P .Marrone

Final approval and acceptance of this dissertation is contingent upon the candidate's submission of the final copies of the dissertation to the Graduate College.

I hereby certify that I have read this dissertation prepared under my direction and recommend that it be accepted as fulfilling the dissertation requirement.

_____ Date: 16 Nov. 2012
Dissertation Director: George H. Rieke

Statement By Author

This dissertation has been submitted in partial fulfillment of requirements for an advanced degree at The University of Arizona and is deposited in the University Library to be made available to borrowers under rules of the Library.

Brief quotations from this dissertation are allowable without special permission, provided that accurate acknowledgment of source is made. Requests for permission for extended quotation from or reproduction of this manuscript in whole or in part may be granted by the head of the major department or the Dean of the Graduate College when in his or her judgment the proposed use of the material is in the interests of scholarship. In all other instances, however, permission must be obtained from the author.

Signed: Krystal Tyler

Acknowledgments

This thesis most certainly would not exist without help from a lot of people! I thank all of them for their support through the years:

My Collaborators: Lee Armus, Matthew Ashby, Lei Bai, Myra Blaylock, Colin Borys, Richard Bower, Kate Brand, Michael J. I. Brown, Denis Burgarella, Vassilis Charmandaris, Vandana Desai, Arjun Dey, Herve Dole, Buell Jannuzi, James Higdon, Sarah Higdon, Emeric Le Floc'h, Sean McGee, John Mulchaey, Casey Papovich, Laura Parker, Daniele Pierini, Yong Shi, Howard Smith, Dave Wilman.

My Prelim Committee: Jill Bechtold, Romeel Davé, Richard Green.
My Thesis Committee: Eiichi Egami, Ed Olszewski, Dan Marrone, Dennis Zaritsky.

Other Awesome People at Steward: Miwa Block, Erin Carlson, Michelle Cournoyer, Don McCarthy, Peter Strittmatter, and everyone in the business office.

Former Advisors/Mentors: Wei Cui, John Finley, Michael Pahre, Alice Quillen.

Friends from Steward: Vanessa Bailey, Erik Brogt, Richard Cool, Kristian Finlator, Karen Knierman, Jackie Monkiewicz, Moire Prescott, Megan Reiter, Wiphu Rujopakarn, Wayne Schlingman, Nate Stock, Patrick Young.

Friends not from Steward: Rachel Ayers, Jessica Doyle, David Humble, Kat McConnell, Bob & Loren Richey, Ian Seelbach, my D&D groups.

All those involved with the creation and running of *Spitzer*, *Chandra*, *Hubble*, Whipple, VERITAS, and the MMT.

NASA, the NSF, and others who funded my research over the years.

And last, but most definitely not least, I dearly thank George Rieke, hands-down the best advisor a grad student could ever ask for. Without his gentle guidance, endless encouragement, and confidence in my abilities (even–no, especially–when I had little belief in myself), I know, without a doubt, that I would not have finished grad school and this thesis would simply be a pipe dream. For that, no amount of thanks will ever be enough.

Dedication

This thesis is dedicated to those who make life worth living:

My parents, Dale & Marcella Tyler, for their love, encouragement, and faith.

My brother, Kerry Tyler, for his quiet support, computer expertise, and paving the way.

Kim & Scott Baker, for their loving friendship, frequent humor, endless encouragement, and the world's best chicken nuggets.

And my Lord and Savior, Jesus Christ.

Table of Contents

List of Figures 8
List of Tables 10
Abstract 11

Chapter 1 Introduction 13

Chapter 2 Star Formation and AGN Activity in the Galactic Environment of ULIRGs and HyLIRGs 19
2.1 Introduction 19
2.2 Sample & Data Reduction 21
2.3 Analysis 25
2.3.1 Source SEDs 25
2.3.2 Templates 25
2.3.3 Additional Templates 32
2.3.4 IR Bolometric Luminosity 36
2.4 Discussion 39
2.5 Conclusions 44

Chapter 3 The Nature of Star Formation at 24μm in the Group Environment at $0.3 \lesssim z \lesssim 0.55$ 46
3.1 Introduction 47
3.2 Sample & Data Reduction 51
3.2.1 Sample Selection and Photometry 51
3.2.2 Uncertainties and Reliability 54
3.3 IR Properties of Sample Galaxies 55
3.3.1 Methodology 56
3.3.2 Results for IR-Active Galaxies 57
3.4 Discussion 81
3.5 Conclusions 87

Chapter 4 Star-Forming Galaxy Evolution in Nearby Rich Clusters 89
4.1 Introduction 90
4.2 Sample & Data Reduction 93
4.2.1 Infrared Observations 93
4.2.2 Optical Observations 95
4.2.3 UV Observations 96
4.2.4 Sample Selection 96
4.3 SFR Function 100

TABLE OF CONTENTS — *Continued*

4.3.1 Methodology 100
4.3.2 Initial Cluster SFR Function 103
4.4 Passive Early-Type Galaxies 104
4.4.1 The Passive UV- and IR-Emitting Galaxy Population 104
4.4.2 Identifying the E/S0 IR Emission Source 108
4.5 Star-Forming A2029 Galaxies 112
4.5.1 Revised SFR Function 112
4.5.2 Comparison with Stellar Mass 114
4.5.3 Galaxy Distribution 116
4.6 Comparison with Other Clusters & the Field 118
4.6.1 SFR Function 118
4.6.2 Mass–SFR Relation 119
4.6.3 Anemic Coma Galaxies 126
4.6.4 24μm-Emitting Early-Type Galaxies 132
4.7 Discussion 132
4.8 Conclusions 137

CHAPTER 5 STAR FORMATION IN X-RAY UNDERLUMINOUS CLUSTERS . . 139
5.1 Introduction 140
5.2 Observations & Sample Selection 142
5.2.1 Observations 142
5.2.2 Sample Selection 145
5.3 Results 150
5.4 Discussion 157
5.5 Conclusions 160

CHAPTER 6 CONCLUSIONS AND FUTURE DIRECTIONS 162
6.1 High-Redshift ULIRGs and HyLIRGs 162
6.2 Star-Forming Galaxies in Groups 163
6.3 Star-Forming Galaxies in Clusters 164
6.4 Future Directions 167

APPENDIX A EARLY-TYPE GALAXIES WITH 24μM EMISSION IN GROUPS . . 169

REFERENCES 176

List of Figures

2.1 U/HyLIRGs Matched to F00183-7111 29
2.2 U/HyLIRGs Matched to Mrk231 30
2.3 Comparing F00183-7111 and Mrk231 with Source MIPS004 31
2.4 U/HyLIRGs with Star Formation 33
2.5 Star-Forming Sources with IRAS 1525 35
2.6 Blackbody Fitting 40

3.1 L_{TIR}/SFR vs. Redshift 58
3.2 Group Fractional Luminosity Functions 59
3.3 24μm with respect to Group Membership 63
3.4 Mass–SFR Relation 66
3.5 SSFR Distributions 67
3.6 SSFR of Group/Field Galaxies of Different Masses 69
3.7 Fraction of Low/High Activity Galaxies with respect to Mass . . . 70
3.8 Significance Test of Fraction of Low-Activity Galaxies 72
3.9 Asymmetry/Concentration Values 75
3.10 AGN Test using IRAC Colors 78
3.11 Mass–SFR Relation with Morphology 80

4.1 Cluster Velocity Profile 98
4.2 SFR Function 105
4.3 Passive Early-Types Sample Spectra 106
4.4 SDSS Images of Passive Early-Types 107
4.5 L_{24} vs. K_S Luminosity 111
4.6 Revised SFR Function 113
4.7 Mass–SFR Relation for A2029 and the Field 115
4.8 R_{proj} Distribution 117
4.9 SFR Function using 24 μm Only 120
4.10 Mass–SFR Relation for A2029 and Coma 122
4.11 Offset of Cluster Galaxies from Field Mass–SFR Relation 124
4.12 Hα Aperture Corrections 125
4.13 Coma Offset from Field Mass–SFR Relation in Mass Bins 127
4.14 WISE AGN Diagnostic 131
4.15 Completeness-Corrected Mass–SFR Offsets 133
4.16 L_{24} vs. K_S Luminosity with Coma Early-Types 134

5.1 Mass–L_X Relation for XUCs 143
5.2 Galaxy Velocity Distributions 147
5.3 BPT Diagram 149
5.4 Distribution of R_{proj} 152

LIST OF FIGURES — *Continued*

5.5 SFR Functions 153
5.6 Mass–SFR Relations 155
5.7 Mass–SFR Offsets 156
5.8 Combined Mass–SFR Relation and Offset 158

A.1 Images of Early-Type Galaxies with IR Detections 171
A.2 SEDs for Star-Forming E/S0 Galaxies 175

List of Tables

2.1 U/HyLIRG Source Data 23
2.2 $L_{IR,bol}$ Template Measurements 38
2.3 Constraints on $L_{IR,bol}$ 41

4.1 A2029 Member List 99
4.2 Anemic Coma Cluster Galaxies 129

A.1 Early-Type Group Galaxies Matched with IR Sources 170

Abstract

This thesis focuses on how a galaxy's environment affects its star formation, from the galactic environment of the most luminous IR galaxies in the universe to groups and massive clusters of galaxies.

Initially, we studied a class of high-redshift galaxies with extremely red optical-to-mid-IR colors. We used *Spitzer* spectra and photometry to identify whether the IR outputs of these objects are dominated by AGNs or star formation. In accordance with the expectation that the AGN contribution should increase with IR luminosity, we find most of our very red IR-luminous galaxies to be dominated by an AGN, though a few appear to be star-formation dominated.

We then observed how the density of the extraglactic environment plays a role in galaxy evolution. We begin with *Spitzer* and HST observations of intermediate-redshift groups. Although the environment has clearly changed some properties of its members, group galaxies at a given mass and morphology have comparable amounts of star formation as field galaxies. We conclude the main difference between the two environments is the higher fraction of massive early-type galaxies in groups.

Clusters show even more distinct trends. Using three different star-formation indicators, we found the mass–SFR relation for cluster galaxies can look similar to the field (A2029) or have a population of low-star-forming galaxies in addition to the field-like galaxies (Coma). We contribute this to differing merger histories: recently-accreted galaxies would not have time for their star formation to be quenched by the cluster environment (A2029), while an accretion event in the past few Gyr would give galaxies enough time to have their star formation suppressed by the cluster environment.

Since these two main quenching mechanisms depend on the density of the intracluster gas, we turn to a group of X-ray underluminous clusters to study how star-forming galaxies have been affected in clusters with lower than expected X-ray emission. We find the distribution of star-forming galaxies with respect to stellar mass varies from cluster to cluster, echoing what we found for Coma and A2029. In other words, while some preprocessing occurs in groups, the cluster environment still contributes to the quenching of star formation.

Chapter 1

Introduction

As with many of science's greatest discoveries, galaxy clusters were originally found by accident. Charles Messier, in the eighteenth century, was looking for comets, which appeared as fuzzy objects on the sky. He found that some of these fuzzy objects were not comets and were in the same place every night. Not wanting to confuse these with the comets he was looking for, he called them "nebulae" and organized them into the now well-known catalog that bears his name (Messier, 1784). This catalog included objects both inside and outside our own galaxy, from true nebulae to galaxies and, in one case, a massive cluster of galaxies, known today as the Virgo cluster. At the same time, Sir Friedrich Wilhelm Herschel was also observing these nebulae, though he was more interested in the nebulae themselves than Messier. In 1785, he noted a collection of nebulae in Coma Berenices, which would later be known as the Coma cluster (Herschel, 1785).

Hubble's classifications, along with proof that these nebulae (galaxies) were outside of our own, opened the door for the study of large collections of galaxies (Hubble 1926; Hubble 1929). It wasn't until the 1950s, however, when cluster research truly took off. Thanks to Abell's famous catalog of nearby galaxy clusters—a sample that is still used to this day—it became easier to study global trends in these densest regions of the universe (Abell, 1958). (For more about the history of cluster research, see the much more comprehensive overview of Biviano 2000.)

Astronomers began to confirm trends from prior research using a much larger sample of clusters. Several groups noticed that clusters tended to contain more

early-type galaxies than the field (e.g., Hubble & Humason 1931; Spitzer & Baade 1951; Morgan 1961; Oemler 1974). More specifically, Abell (1974) noted that clusters with a large, central elliptical (cD) tended to be more spherical in shape, with a well-defined center. Clusters with more spiral galaxies were, overall, more irregularly-shaped without a well-defined center or density gradient (Abell 1974; Oemler 1974). The increased fractions of early-type and decreased fractions of late-type galaxies from the least to most dense regions in the universe has become known as the morphology–density relation (e.g., Dressler 1980; Whitmore et al. 1993; van der Wel et al. 2007; Tempel et al. 2011).

At the time of Hubble's classifications, it was known that spiral galaxies housed young, blue stars and elliptical/lenticular galaxies (E/S0) were dominated by older, red stars. As expected given the morphology–density relation, astronomers found that cluster galaxies tended to be redder, more massive, and have less star formation than galaxies in the field, even at higher redshifts (Kennicutt 1983a; Balogh et al. 1997; Hashimoto et al. 1998; Poggianti et al. 1999; Lewis et al. 2002; Gómez et al. 2003; Christlein & Zabludoff 2005; Bai et al. 2009; Tempel et al. 2011).

Clearly, the dense environment of clusters had an effect on the galaxies that fell into the potential, but what part of the cluster environment was responsible for these changes?

Spitzer & Baade (1951) suggested collisions between galaxies stripped interstellar material (ISM) from the galaxies themselves, preventing them from becoming spirals with young stars and, instead, turning them into galaxies with only older stars. This would explain the much larger fraction of S0 galaxies in clusters. Indeed, mergers and tidal interactions between galaxies—and between galaxies and the cluster—can greatly affect galaxy morphology and star formation rates

(SFRs; Barnes & Hernquist 1996; Henricksen & Byrd 1996; Mihos 2004; Conselice 2006).

Once Limber (1959) considered that there must be excess gas among the galaxies of clusters (and subsequently discovered in Coma by Meekins et al. 1971 and Gursky et al. 1971), others began to wonder how such an intracluster medium (ICM) might affect galaxies captured by the cluster potential. Cowie & Songaila (1977) suggested the ICM could heat the gas in a galaxy enough for it to evaporate. A galaxy radially falling into a dense cluster could have almost all of its gas removed by the ram pressure from the ICM (Gunn & Gott 1972; Kinney et al. 2004; van Gorkom 2004; Sivanandam et al. 2010) or perhaps only its hot outer halo of gas removed (Larson et al. 1980; Balogh et al. 2000; Kawata & Mulchaey 2008; McCarthy et al. 2008). All of these mechanisms would cause star formation in a spiral galaxy to cease in anywhere from several Myr to a few Gyr and form either a passive spiral or an S0. (See Boselli & Gavazzi 2006 for a more complete assessment of the various star-formation quenching mechanisms.)

Not all clusters have strong X-ray emission, however. Recent studies have shown that X-ray selected clusters show a trend in terms of their mass and X-ray luminosity (L_X), but there is a population of clusters (typically optically-selected) with lower L_X than expected given this relation (e.g., Balogh et al. 2002; Basilakos et al. 2004; Lubin et al. 2004; Popesso et al. 2007; Dietrich et al. 2009; Castellano et al. 2007). Whether these clusters are X-ray underluminous because they are in the process of forming (Balogh et al. 1997; Popesso et al. 2007) or experiencing a massive merger event (Barrena et al. 2002; Clowe et al. 2004; Popesso et al. 2007), the star forming galaxies may react differently in these environments.

But, as it turns out, clusters aren't the only environment where galaxy morphology, color, and SFR can be affected. Galaxy groups have been found to

be intermediate between isolated and cluster galaxies in more than just density. Zabludoff & Mulchaey (1998), Wilman et al. (2009), and others have found that the proportion of early-type galaxies in groups can range from typical values of the field to those of clusters. These findings agree with prior ones that show galaxies can be "pre-processed" in groups before they enter the cluster environment (Zabludoff et al. 1996; Zabludoff & Mulchaey 1998; Lewis et al. 2002; Gómez et al. 2003; Kawata & Mulchaey 2008). Just et al. (2010) confirmed the increase in S0s with decreasing redshift occurs in moderate-mass groups and poor clusters.

Despite all the research up to this point, it is still unknown not only what mechanism is most responsible for these galaxy transformations but in what environment they are most likely to occur or where most of the changes take place.

Many new telescopes and instruments have aided in the search for answers to these questions. The *Hubble Space Telescope*'s sensitive cameras provide a clearer view of distant galaxy morphologies. Multi-object spectrographs (MOS) allow researchers to determine the redshifts of large numbers of galaxies, which is necessary for accurately identifying cluster and group members.

The *Spitzer Space Telescope*, however, opened wide the door to mid- and far-infrared (MIR and FIR, respectively) astronomy that has up until recently remained mostly closed. While SFRs can be estimated using other wavelengths, such as optical (e.g., Hα) and the ultraviolet (UV), they require corrections for dust obscuration that are often uncertain at best. IR observations do not require such corrections, and the 24 μm waveband, specifically, correlates with total IR luminosity (L_{IR}; integrated luminosity from $\sim$8 to 1000 μm), making it a good estimator of the total SFR in a galaxy (Rieke et al., 2009). The Infrared Array Camera (IRAC; Fazio et al. 2004) and Infrared Spectrometer (IRS; Houck et al. 2004) al-

low us to identify star-forming galaxies and active galactic nuclei (AGNs) with photometry (3.6, 4.5, 5.8, and 8.0 μm) and spectra (5.2 to 38 μm), respectively. The Multiband Imaging Photometer for *Spitzer* (MIPS; Rieke et al. 2004) probes total star formation and the Wien side of the IR peak (24, 70, and 160 μm).

Still, the IR can underestimate SFRs at very low levels due to higher fractions of unobscured star formation in such systems, so to accurately estimate star formation from the lowest levels to the brightest IR galaxies, it is best to use a variety of wavelengths, if possible. Here, we focus on the MIR ($\sim$5 to 40 μm) for higher-redshift galaxies ($z > 0.3$) and include optical/UV wavelengths with the IR for nearby galaxies, where observing in multiple bands is both easier and more useful for detecting low levels of star formation.

In this thesis, we begin by studying the brightest IR objects in the universe: a sample of ultraluminous and hyperluminous infrared galaxies (ULIRGs and HyLIRGs) with very red optical-to-mid-IR colors, making them true "IR galaxies." These galaxies are most common at higher redshifts ($1.5 < z < 3.0$) and extremely rare locally. What powers the IR emission in these extreme galactic environments is up for debate. The brightest are found to have at least some AGN component. But how much of the IR emission is from AGNs and how much from pure star formation? In Chapter 2, we select eleven of the brightest IR galaxies (with respect to optical emission) in the Boötes field to try to identify the dominant source of their IR emission.

The thesis then turns to galaxy properties in large-scale environments. Chapter 3 focuses on a selection of galaxy groups at $0.3 \lesssim z \lesssim 0.55$ from the Second Canadian Network for Observational Cosmology (CNOC2) survey. Our goal is to see just how groups at intermediate redshift differ from the field and clusters in terms of their morphologies and IR star-forming galaxies.

Chapter 4 moves up another notch on the density scale to massive clusters (M $> 10^{15}$ $M_{\odot}$). Here, we study star formation in Abell 2029 and Coma using Hα, far-UV (FUV), and MIR. The multiwavelength SFRs give us a more complete picture of star formation in these clusters than focusing on one wavelength alone.

We then switch to a sample of XUCs for Chapter 5 to probe how the lower levels of X-ray emission in these clusters affect star forming galaxies differently than in bright X-ray-emitting clusters (if at all). This and the previous chapter should narrow down the mechanism by which star formation is quenched in these most dense environments.

Finally, in Chapter 6, we summarize our findings and look to future observations and technologies to further our understanding of galaxy environments and how these regions affect the populations therein.

CHAPTER 2

STAR FORMATION AND AGN ACTIVITY IN THE GALACTIC ENVIRONMENT OF ULIRGS AND HYLIRGS

(Tyler et al. 2009, ApJ, 691, 1846)

We present new 70 and 160 μm observations of a sample of extremely red (R-[24] $\gtrsim$ 15 mag), mid-infrared bright ($f_{24\mu m} \gtrsim 1$ mJy), high-redshift ($1.7 \lesssim z \lesssim 2.8$) galaxies. All targets detected in the far-IR exhibit rising spectral energy distributions consistent with dust emission from obscured AGN and/or star-forming regions in luminous IR galaxies. We find that the SEDs of the high-redshift sources are more similar to canonical AGN-dominated local ULIRGs with significant warm dust components than to typical local star-forming ULIRGs. Fitting modified blackbody curves to the data, the inferred IR ($8 - 1000\mu$m) bolometric luminosities of the high-z sources are found to be $L_{bol} \sim 3 \times 10^{12}$ to 3×10^{13} $L_\odot$ (ULIRGs/HyLIRGs), representing the first robust constraints on L_{bol} for this class of object.

2.1 Introduction

The *Spitzer Space Telescope* (Werner et al., 2004) has revealed a large number of Luminous, Ultraluminous, and Hyper-luminous Infrared Galaxies[1] out to $z \sim 3$. These objects have some of the highest IR luminosities known. Initially studied at mid-IR wavelengths from the ground by Rieke & Low (1972), this class of source has since been studied and catalogued using facilities like *IRAS, ISO,* SCUBA, and *Spitzer* (Soifer et al. 1987; Smail et al. 1997; Blain et al. 1999; Elbaz et al.

[1]LIRGs: 10^{11} $L_\odot \lesssim L_{IR} \lesssim 10^{12}$ $L_\odot$, ULIRGs: 10^{12} $L_\odot \lesssim L_{IR} \lesssim 10^{13}$ $L_\odot$, and HyLIRGs: $L_{IR} \gtrsim 10^{13}$ $L_\odot$, respectively, where L_{IR} is determined from 8 to 1000 μm.

1999; Sergeant et al. 2001; Dole et al. 2001; Farrah, et al. 2003; Le Floc'h et al. 2005; Brand et al. 2007). While rare in the nearby universe, they contribute significantly to the cosmic infrared background (CIRB) and star formation density at high redshifts (Chary & Elbaz 2001; Franceschini et al. 2001; Blain et al. 2002; Lagache et al. 2003).

To better understand galaxy evolution, especially the high-redshift stages, we need to better understand these IR-luminous sources. However, the mechanism that powers such intense IR emission in these objects remains ambiguous. In the local universe, ULIRGs tend to consist of interacting galaxies and are often powered by both AGN and star-formation activity (Genzel et al. 1998; Lutz et al. 1998; Laurent et al. 2000; Armus et al. 2006, 2007). The most luminous sources are typically dominated by AGN. Are the high-redshift, IR-luminous sources simply analogs to their local counterparts? Are they powered by a mixture of obscured AGN and embedded star formation? Or is the trend toward AGN dominance with increasing luminosity continued with the very energetic sources accessible at high redshift (Lutz et al. 1998; Tran et al. 2001)?

AGN and starbursts are characterized by quite different spectral signatures. The mixture of these signatures in ULIRGs and HyLIRGs leads to complex SEDs, and it can be hard to make predictions of their behavior due to the difficulty of separating the AGN and star-forming components. Observations throughout the electromagnetic spectrum are needed to get an accurate understanding of the respective contribution of star-forming and nuclear activity powering their bolometric output. In particular, it is crucial to observe these objects in the mid- and far-IR since this is the wavelength range where the bulk of their bolometric luminosity is released.

Previous studies have used spectra from the Infrared Spectrometer (IRS) on

Spitzer (Houck et al., 2004) to predict the excitation mechanism and far-IR emission of these high-redshift, IR-luminous objects (Houck et al. 2005; Yan et al. 2005). While this may be reasonably accurate for heavily star-forming galaxies, the mixture of AGN and star-formation in ULIRGs results in a more complex IR SED that may not be accurately reflected at the mid-IR wavelengths accessed by IRS. Far-IR observations are needed to constrain the behavior of these sources more completely.

This paper reports far-IR (70 and 160 μm) measurements of one of the most elusive subsets of these galaxies: objects with extremely high mid-IR luminosity but that are exceptionally faint in the observed visible region, located at high redshift (at $1.7 \lesssim z \lesssim 2.8$). Assuming the high-redshift objects have similar SEDs as nearby objects with similar AGN and star-forming components, we estimate the roles of these components in the high-redshift objects from fitting the low-redshift SEDs. In analyzing their properties, we assume the cosmological parameters H_0 = 70 km s^{-1} Mpc^{-1}, $\Omega_M = 0.3$, $\Omega_\Lambda = 0.7$.

2.2 Sample & Data Reduction

The Boötes field of the NOAO Deep Wide Field Survey (NDWFS; Jannuzi & Dey 1999) has been observed using the Multiband Imaging Photometer for *Spitzer* (MIPS; Rieke et al. 2004) to search for IR-bright galaxies with faint or no optical counterparts ($R \gtrsim 25$ mag; Houck et al. 2005). We identified 30 objects characterized by very red optical-to-mid-IR colors ($R - [24] \gtrsim 15$) and identified by IRS to have redshifts from $1.7 \lesssim z \lesssim 2.8$ (Houck et al., 2005). These galaxies were selected to be, on average, 5 to 10 times brighter in the mid-IR ($f_{24\mu\mathrm{m}} \gtrsim 1$ mJy) than sources pre-selected by SCUBA/VLA, but they inhabit a comparable redshift range (Chapman et al. 2003, 2005; Egami et al. 2004; Pope et al. 2006).

We report deep observations[2] with MIPS at 70 and 160 μm of 20 sources randomly distributed to be generally representative of this sample. Nineteen have detections or upper limits at 70 or 160 μm, of which 11 have known redshifts and IRS spectra (Houck et al., 2005).

The data for these 20 sources were reduced using version 3.06 of the MIPS Data Analysis Tool (DAT; Gordon et al. 2007). In addition to the standard processing discussed in this paper, additional corrections for the 70 μm data were applied as described in Gordon et al. (2007). We measured the flux density of each source at 70 μm and 160 μm using the PSF fitting routine ALLSTAR in the IRAF[3] environment. At 70 μm we chose a source aperture (radius) of 16 arcsec and sky aperture of 39-65 arcsec and corrected for flux lost in the wings of the PSF (Gordon et al., 2007). Similar procedures were used at 160 μm, with a source aperture of 30 arcsec, a sky annulus from 32-56 arcsec, and correction for lost signal as described in Stansberry et al. (2007). Errors were estimated by measuring background flux in apertures outside the source PSF but inside the area of the image with complete coverage (full exposure). Upper limits for undetected sources were estimated at the 3σ noise level. These measurements are summarized in Table 1.

Twelve of the sources listed in Table 1 have powerlaw IRS spectra with no obvious spectral features. All but one of these sources, from Weedman et al. (2006), have unknown redshifts, though we still include them in our sample. They will be discussed in more detail in later sections.

[2]PID 20303

[3]IRAF is distributed and supported by the National Optical Astronomy Observatories (NOAO).

Table 2.1. U/HyLIRG Source Data

GO2 ID[a]	Dataset[b]	IRS[c]	z	α[d]	F24μm (mJy)	F70μm (mJy)	F160μm (mJy)	F20cm[e] (mJy)	Template Fit[f]
1	H05-13	31	1.95	$\cdots$	2.30	9.1 ± 2.5	43 ± 12	5.06	F00183
2	D06-22	$\cdots$	$\cdots$	1.0	0.99	*	*	$\cdots$	$\cdots$
3	D06-11	$\cdots$	$\cdots$	0.4	1.40	9.9 ± 2.7	< 40	$\cdots$	$\cdots$
4	H05-9	8	2.46	$\cdots$	3.83	9.3 ± 2.3	65 ± 11	0.42	F00183
5	H05-8	7	2.62	$\cdots$	2.65	< 8.1	< 38	< 0.15	F00183
6	D06-6	$\cdots$	$\cdots$	1.8	2.40	~ 9 **	*	$\cdots$	$\cdots$
7	H05-1	19	2.64	$\cdots$	1.24	< 9.2	61 ± 13	< 0.15	F00183
9	H05-17	18	2.13	$\cdots$	1.23	10.8 ± 2.6	< 43	< 0.15	Mrk231
10	H05-5	4	2.34	$\cdots$	0.87	< 9.4	< 51	< 0.15	F00183
11	D06-4	$\cdots$	$\cdots$	1.0	0.91	$\cdots$	$\cdots$	$\cdots$	$\cdots$
12	D06-24	$\cdots$	$\cdots$	-0.1	1.05	< 9.7	< 46	$\cdots$	$\cdots$
14	H05-16	16	2.73	$\cdots$	1.04	< 8.1	< 47	< 0.15	F00183

Table 2.1—Continued

GO2 ID[a]	Dataset[b]	IRS[c]	z	α[d]	F24μm (mJy)	F70μm (mJy)	F160μm (mJy)	F20cm[e] (mJy)	Template Fit[f]
15	···	···	···	···	···	< 9.3	38 ± 10	···	···
16	D06-23	···	2.0	1.4	0.98	5.2 ± 2.4	56 ± 15	···	···
17	H05-15	···	1.75	···	1.05	5.4 ± 2.2	31 ± 13	< 0.15	Mrk231
19	H05-12	12	2.13	···	1.12	< 9.1	46 ± 12	0.20	Arp220
21	D06-16	···	···	2.0	2.29	···	···	···	···
24	D06-10	···	···	0.9	0.82	···	···	···	···
25	D06-9	···	···	1.7	0.88	···	···	···	···
26	D06-8	···	···	1.7	0.92	···	···	···	···
27	D06-7	···	···	-0.6	0.87	< 9.7	< 53	···	···
28	H05-7	23	1.78	···	0.78	< 8.3	25 ± 11	< 0.15	Arp220
29	D06-5	···	···	1.3	1.12	< 8.7	47 ± 13	···	···
30	H05-4	21	2.59	···	1.08	< 8.5	< 51	0.24	F00183

2.3 Analysis

2.3.1 Source SEDs

We created SEDs for the 11 sources with known redshifts using the measured 70 μm and 160 μm fluxes and the IRS and 24 μm data from Houck et al. (2005). The 20 cm fluxes were from the Boötes field measurements by de Vries et al. (2002). The SEDs are displayed in Figures 1–4.

2.3.2 Templates

Previous analyses of high-z IR sources (e.g., Houck et al. 2005; Yan et al. 2005) relied on the observed mid-IR to constrain the bolometric IR luminosity. Further insights can be obtained by comparing the observed mid- and far-IR emission and understanding the contributions of AGN and star formation to the bolometric IR emission. To interpret this comparison requires use of template SEDs from local galaxies.

Initially, we used the four templates employed by Houck et al. (2005): NGC 7714, Arp220, Mrk231, and F00183-7111. Brief descriptions of the templates are as follows.

NGC 7714 (Brandl et al. 2004; Marshall et al. 2007) has an unobscured nuclear starburst with relatively shallow silicate absorption and a relatively flat far-IR peak.

Arp220 (Armus et al. 2007; Spoon et al. 2004; Imanishi & Dudley 2000; Silva et al. 1998) is a well-known, local ULIRG heavily dominated by embedded star formation, as can be seen by its prominent aromatic features and very luminous far-IR peak.

Mrk231 (Armus et al. 2007; Weedman et al. 2005; Ivison et al. 2004) is a local AGN (classified as a Seyfert 1) with a relatively flat spectrum and weak aromatic

Table 2.1—Continued

GO2 ID[a]	Dataset[b]	IRS[c]	z	α[d]	F24μm (mJy)	F70μm (mJy)	F160μm (mJy)	F20cm[e] (mJy)	Template Fit[f]
31	H05-2	20	1.86	$\cdots$	0.89	9.1 ± 2.7	41 ± 16	< 0.15	NGC 7714

[a]GO2 MIPS designation.

[b]H05 indicates sources from Houck et al. (2005); D06 indicates sources from Weedman et al. (2006).

[c]IRS spectra ID.

[d]The 14 to 33 μm powerlaw index (Weedman et al., 2006).

[e]Flux densities at 20 cm (de Vries et al., 2002).

[f]Best-fit template fits from Houck et al. (2005).

Note. — Multiwavelength data for all of our sources with 24 μm flux > 1.0 and $R - 24 > 15$. Included are the 11 sources used in our analysis as well as the 12 powerlaw sources. Single asterisks (*) indicate where the data is probably useless due to nearby contaminating source(s). Double asterisks (**) indicate similar cases where sources were deblended but the uncertainty in measured flux densities is high.

features, though it is known that this source has a certain amount of ongoing star formation.

F00183-7111 (Spoon et al. 2004; Armus et al. 1989) is a deeply obscured ULIRG, classified as a radio-loud LINER/Seyfert ≥ 1.5. The source is dominated by the AGN; Spoon et al. (2004) set an upper limit on the IR star-formation component at 30 percent.

We compared these templates with our source SEDs in the manner of Houck et al. (2005): we matched each template to the IRS spectra of our objects and observed how well the templates predicted the far-IR emission. We mostly focused on the IRS continuum, not on the silicate absorption feature, due to the difficulty of determining the source of the absorption.

Figures 2.1 and 2.2 show eight source SEDs best matched by the two AGN templates, F00183-7111 and Mrk231, respectively. In Figure 2.1, the data points for F00183-7111 are plotted as asterisks. Dashed lines connecting the data points are shown to make both the data points and the important features of the template more visible and are not indicative of the actual shape of the template SED beyond $\lambda \lesssim \sim 100$ μm. Filled circles indicate source detections while downward arrows indicate upper limits, where the base of the arrow is the 2σ value of the upper limits. For three of the sources, MIPS 001, 004, and 005, the template overestimates the rest-frame far-IR emission despite that the IRS spectra are reasonably well-matched to the template. One source, MIPS 0010, is slightly underestimated by the AGN template and has possible aromatic features, though the rest of the SED is indicative of AGN emission. Figure 2.2 shows the four sources best-fit by Mrk231. As with the previous figure, filled circles are detections while arrows are 2σ upper limits. Three of the objects (MIPS 014, 028, and 030) are fit within the errorbars of the measurements (or upper limits); one is slightly underestimated

at 70 μm. For this second group of objects, the IRS spectra predict the far-IR emission more accurately than those objects fit by F00183-7111.

The main difference between these two templates in the mid- and far-IR wavelengths is the silicate absorption feature. F00183-7111, known to be highly obscured, has much deeper silicate absorption than Mrk231. Due to the similarities between the templates from the IRS wavelengths to 160 μm, however, F00183-7111 and Mrk231 can be used almost interchangeably (though most of our sources have radio emission more similar to Mrk231 than the radio-loud F00183-7111). Figure 2.3 shows this more clearly by plotting one of our sources, MIPS 004, with the two templates, which have been matched to the IRS spectrum of MIPS 004. Although F00183-7111 is mostly incomplete beyond rest-frame 160 μm, the far-IR peaks of the templates are comparable.

With F00183-7111 and Mrk231 being similar, AGN-dominated sources with very little obvious star formation contributing to the IR ($\lesssim 30$ percent for F00183-7111; Spoon et al. 2004), it appears that at least 8 of our 11 sources are dominated by AGN emission in the observed mid- and far-IR. Significant embedded star formation in these objects would be detected at 160 μm, resulting in brighter emission in the far-IR than permitted by our detections and upper limits.

One additional object (MIPS 007) was fitted with Mrk231; however, this template drastically underestimates the 160 μm detection for that source, leading us to believe that obscured star formation in this object contributes significantly to the bolometric IR luminosity. The final two sources, MIPS 019 and 031, are approximately equally well fit by both Arp220 and NGC 7714. Template matching for these three objects is shown in Figure 2.4. Because Arp220 unrealistically overestimates the far-IR data for MIPS 019 and 031, we plot NGC 7714 with the SEDs. This also shows us that these two objects have significant star formation, though

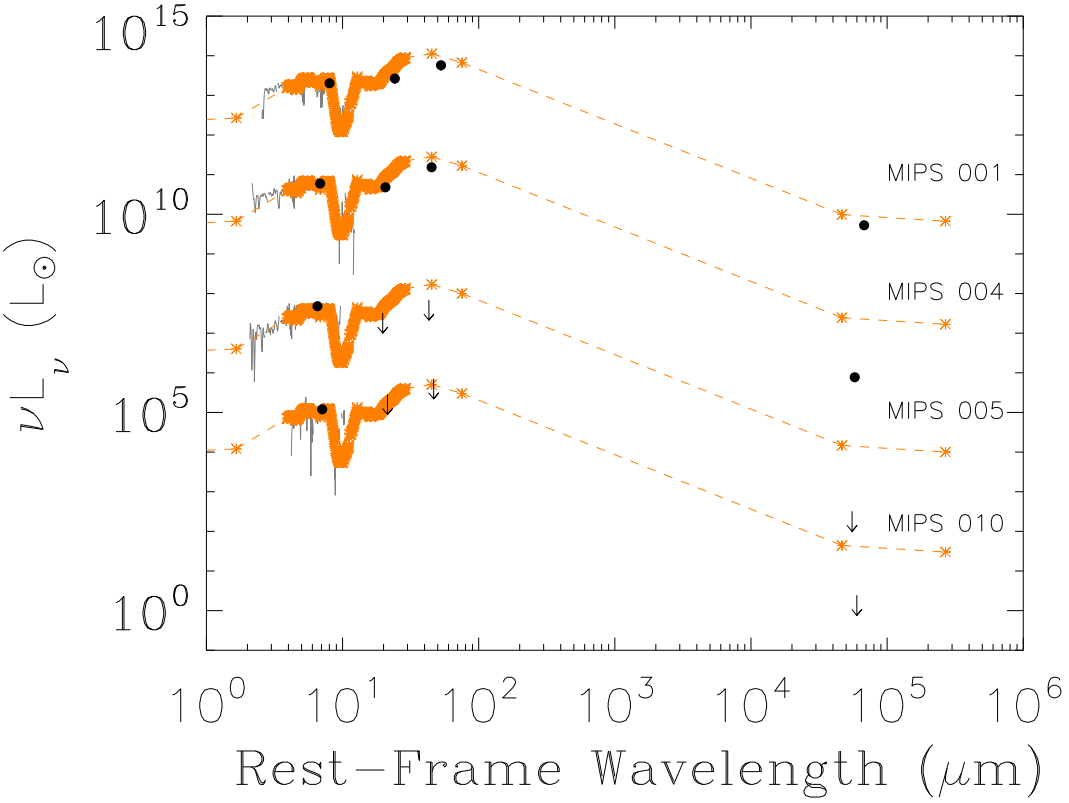

Figure 2.1 The four sources with the best IRS match to the F00183-7111 template (colored orange in the electronic version), MIPS 001, 004, 005, and 010, multiplied by $10, 10^{-2}, 10^{-5}$, and 10^{-7}, respectively. The 70 and 160 μm upper limits have been set at 2σ and are indicated by arrows with the base of the arrow set to the values of the upper limits. The template itself is indicated by asterisks and connected with a dotted line to show the far-IR peak more clearly. The template typically overestimates the far-IR SED, which, along with the lack of aromatic features, is consistent with the IR emission from these objects being mostly due to an embedded AGN. MIPS 010 appears to have weak aromatic features, however, which indicates some star formation occurring in this object.

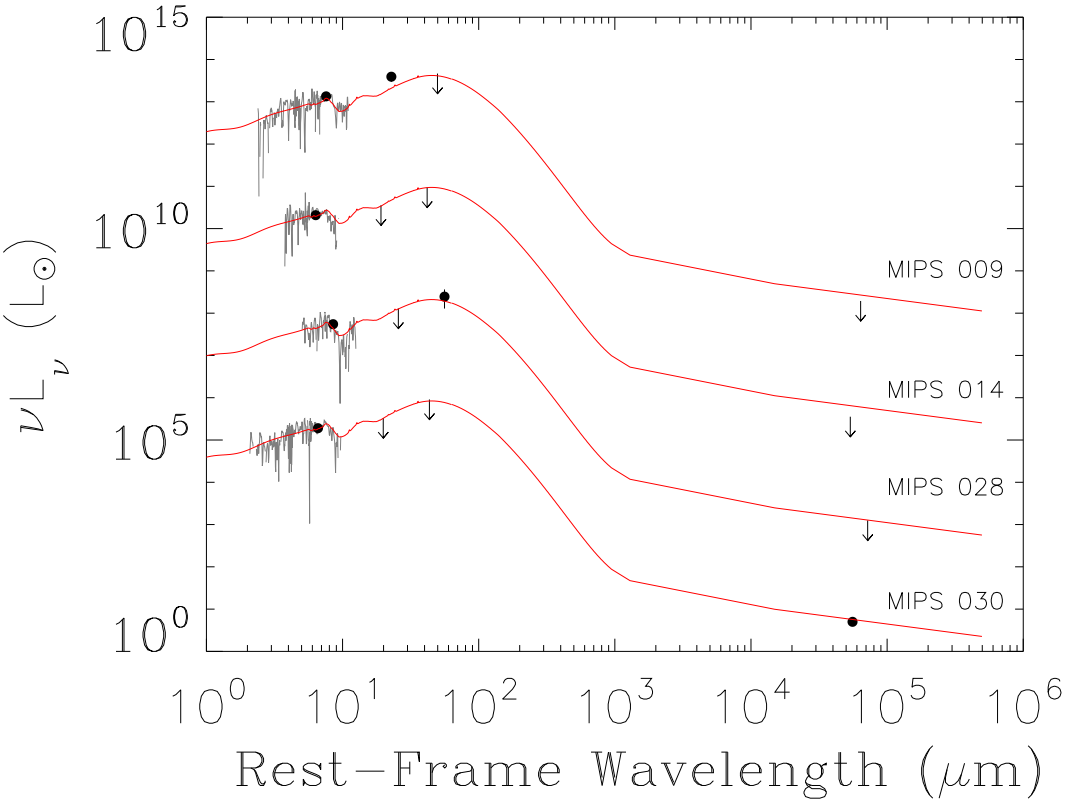

Figure 2.2 The four sources best matched by the Mrk231 template (red), MIPS 009, 014, 028, 030, multiplied by $10, 10^{-2}, 10^{-4}$, and 10^{-7}, respectively. Again, the arrows indicate the 2σ upper limits with the value of the upper limit at the base of the arrows. The IRS spectra have no obvious aromatic features, and the template fits the far-IR and radio portions of the SED fairly well. Like Figure 2.1, these objects are probably dominated by reprocessed AGN emission rather than star formation.

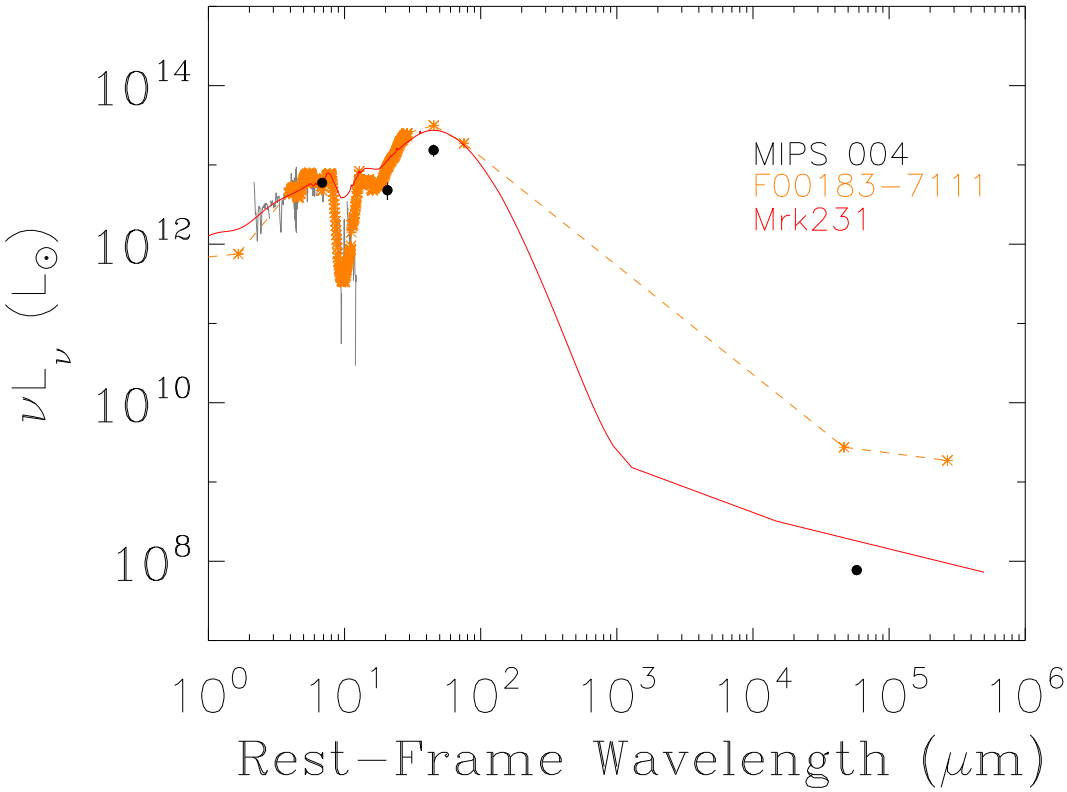

Figure 2.3 A comparison of the templates F00183-7111 (orange) and Mrk231 (red), matched to the IRS spectrum of MIPS004. The major differences are F00183-7111's deeper silicate absorption feature and the loud radio emission due to the AGN (Spoon et al. 2004, Armus et al. 1989). However, these two templates are nearly idential in the wavelength ranges most important for our results. Because of this and Mrk231's more complete far-IR and sub-mm data, we use it to estimate L_{bol} for the eight sources best matched by both templates. There will be additional errors for the sources matched by F00183-7111 due to the object's loud radio emission, but these errors should be small with respect to L_{bol}.

like MIPS 007 and MIPS 010, we cannot be sure how much of the bolometric IR luminosity comes from obscured star formation.

2.3.3 Additional Templates

Our initial template fits suggest that 8 out of 11 objects are strongly dominated by AGN. However, the four templates used so far are somewhat limited in scope: one star-formation dominated object most do not consider a "representative" ULIRG, a nearby starburst, and two AGN-dominated objects that turn out to be rather similar in the mid- and far-IR.

We used additional templates of NGC 1068 (Imanishi & Dudley 2000; Le Floc'h et al. 2001; Spinoglio et al. 2005), CXOJ1417 (Le Floc'h et al., 2007), and NGC 4418 (Spoon et al., 2001) to test this conclusion. Most of the templates have emission consistent with a mixture of both AGN activity and star formation. However, none of the templates fit our sources as well as F00183-7111 and Mrk231 for the AGN-dominated sources, supporting the conclusion that the IR emission from these eight objects is mostly from AGN.

It is possible, however, we are looking at star formation obscured at a much higher level than any of the templates we have so far tested. Given the subdued far-IR outputs of most of our sample, we also compared their SEDs with that of IRAS 15250+3609 using the same method as the previous templates. IRAS 15250+3609 is star-formation dominated, as judged by its lack of high-excitation fine structure lines and minimal X-ray emission (Armus et al., 2007). However, it has some attributes that in other sources are associated with an AGN: deep silicate absorption and a SED with strong output in the mid-IR relative to the far-IR. This latter behavior is of interest in a template, given suggestions that the IR luminosities of bright 24 μm sources at $z \sim 2$ are lower than previous estimates when longer wavelength data are considered (Papovich et al. 2007; Rigby et al.

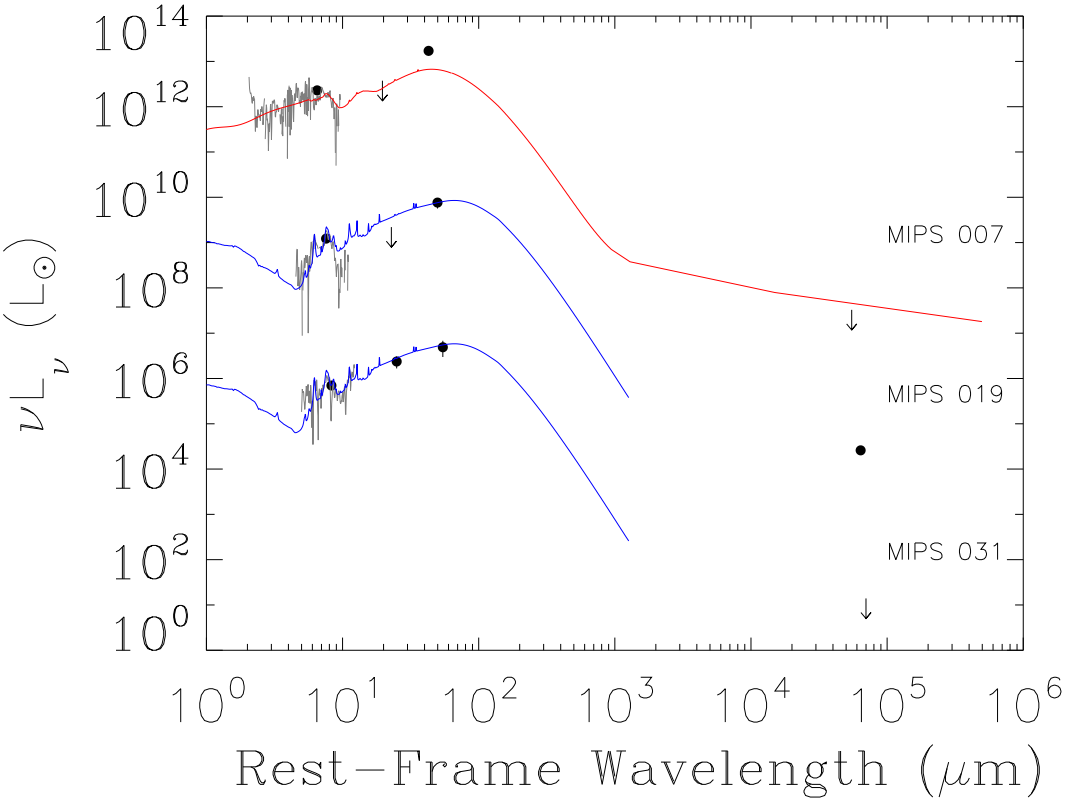

Figure 2.4 Three sources (MIPS 007, 019, and 031, multiplied by $10, 10^{-3}$, and 10^{-6}, respectively) with possible embedded star formation and their best-matched templates, Mrk231 (red) and NGC 7714 (blue). The upper limits (arrows) are indicated as in previous figures. While the IRS spectrum of MIPS 007 is best matched with the AGN Mrk231, the template clearly underestimates the 160 μm detection This leads us to suspect that this source has a significant fraction of embedded star formation contributing to the far-IR emission. MIPS 019 and MIPS031 have similar IRS spectra and aromatic features as NGC 7714. The far-IR reflects this similarity as well, demonstrating the likely star formation occurring in these two objects.

2008). The aromatic features are present in its spectrum but strongly modified in shape by interstellar absorption.

Figure 2.5 shows four of our sources matched with the IRAS 15250+3609 template. The top three objects are those that had additional far-IR emission compared with Mrk231. The top source (MIPS 007) is clearly not well-fit in the IRS wavelengths, though the far-IR measurements are consistent with the template. The IRS spectra of MIPS 019 and 031 appear to have features consistent with star formation (as shown by both this template and previous fitting); however, the far-IR is still somewhat overestimated. These sources could have significant star formation as compared with the AGN emission, though the star formation is probably highly obscured. The bottom object, MIPS 028, is one of the AGN-dominated sources with the largest 160 to 24 μm fraction. This source is clearly fainter at 70 and 160 μm than IRAS 15250+3609, indicating that even the brightest of our 160 μm-detected objects is most likely dominated by AGN emission rather than star formation.

We conclude that the mid- and far-IR from the majority (eight) of our objects are dominated by emission from an obscured AGN; dust-reprocessed emission from star formation, if present, plays only a minor role. The other three objects have evidence of a larger fraction of star formation as compared with the AGN. For them, can we narrow down what fraction of the IR is emitted from star formation?

We could combine a prototypical starburst SED—say, M82 (Devriendt et al., 1999)— with an AGN—say, Mrk231—and estimate what percentage of the IR emission of MIPS 007, 019, and 031 is from embedded star formation. We could also combine Mrk231 with IRAS 1525 and get upper limits on the amount of star formation contributing to L_{bol}. However, fitting a combination of AGN and

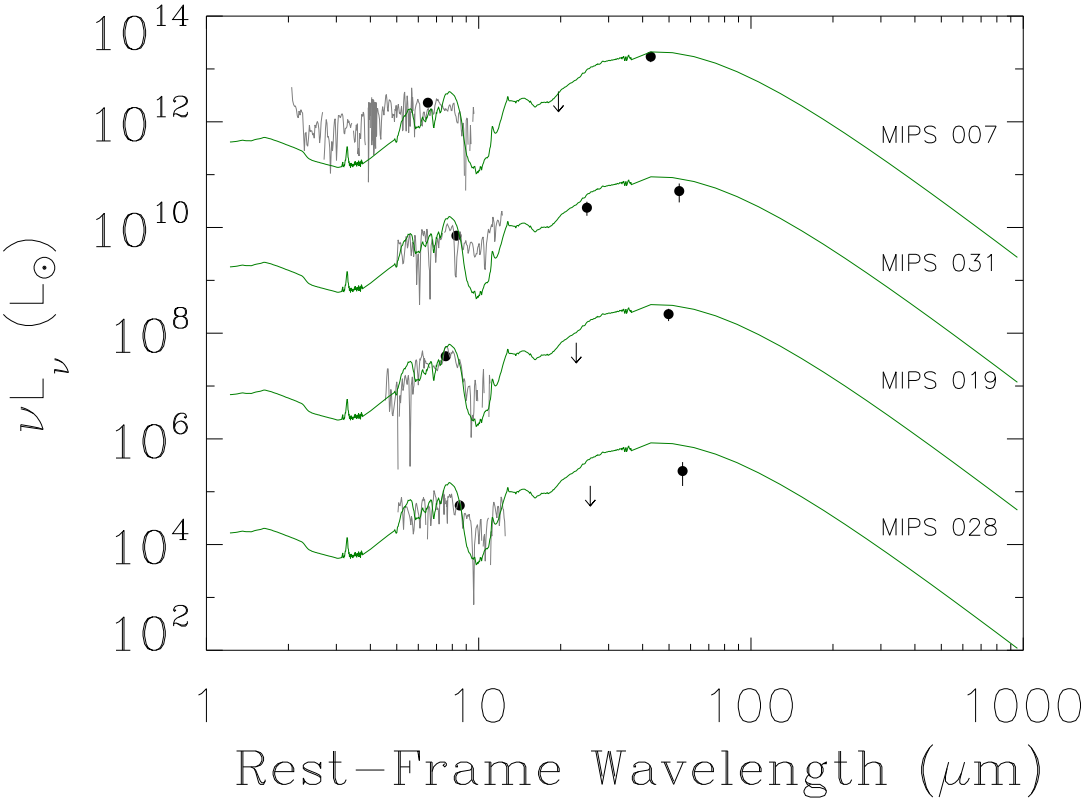

Figure 2.5 IRAS 15250-3609 template fitting. The top three sources (MIPS 007, 019, and 031, multiplied by $1, 10^{-2}, 10^{-5}$ and 10^{-7}, respectively) are those we identified as having a significant fraction of star formation heating the obscuring dust and producing the observed far-IR emission. Our 70 and 160 μm measurements are better matched by this template than those used in Figure 2.4, though they are still somewhat overestimated. The IRS spectra of MIPS031 and MIPS019 are fit reasonably well by IRAS 1525 (green), though the far-IR is still overestimated. The bottom source is MIPS 028, a source we labeled as being dominated by an AGN in the mid-IR. This source has the highest relative 160 μm emission, providing an "upper limit" for our AGN-dominated sources. As expected, the observed far-IR is overestimated, implying that the majority of our sources (including MIPS007) are most likely not extremely-obscured star-forming galaxies misidentified as AGN.

star-forming templates, whether by reduced chi-square or by hand, is subject to large errors, making it nearly impossible to get reasonably accurate estimations with this method. The only thing we can say about these three objects, with any certainty, is that there is significantly more star formation than in Mrk231 or F00183-7111.

2.3.4 IR Bolometric Luminosity

2.3.4.1 Template Fitting

The bolometric IR (8–1000 μm) luminosity of our sources is another important property. Because many objects in our sample have 70 and 160um data and a spectroscopic redshift, we have two points on the blackbody emission from thermal dust, which allows us to make reasonable estimates of the total IR luminosity using the source templates.

Since most of our templates over- or underestimate the far-IR data, we shift the templates in νL_ν until they match the 70 and 160 μm data as closely as possible (almost all were within the error bars). We then truncate and match the template at the longest wavelengths of the IRS spectra so we include both the IRS spectra and the template. We then integrate from 8–1000 μm over the IRS spectra and the shifted template to estimate the bolometric luminosity. Due to F00183-7111's limited far-IR data and its similarity with Mrk231, we use Mrk231 for all eight AGN-like sources. For two of the three sources with significant star formation (MIPS 007 and 019), we use a combination of Mrk231 and M82 to match the 70 and 160 μm data and then integrate over IRS plus the combined Mrk231/M82 template. NGC 7714 fit the far-IR SED of the third star-forming object (MIPS 031) more closely than the Mrk231/M82 combination, so we used that template to estimate the bolometric luminosity for that object. These templates and the resulting L_{bol} are listed in Table 2. Our measurements show that the majority of

the sources are borderline ULIRGs/HyLIRGs with L_{bol} ranging from $3.2 \times 10^{12} L_{\odot}$ to $3.3 \times 10^{13} L_{\odot}$.

2.3.4.2 Blackbody Fitting

While the template fitting provides us with indications of the dominant IR power source as well as a rough estimation of L_{bol}, we also need error bars to constrain the luminosity measurements. We use the 70 and 160 μm data to constrain the far-IR peak by fitting modified blackbodies to the data and examining the resulting range of luminosities.

We use three modified blackbodies with a dust emissivity wavelength dependence proportional to $\lambda^{-\beta}$ with β = 1.5. We started by setting the temperature of the coldest blackbody curve and allowing the warmer two curves to vary. The summed curve was allowed to vary within the error bars of the 70 and 160 μm data (or up to 3σ below the upper limit if there were no detections) and within the endpoints of the IRS spectra. We calculated L_{bol} for each set of temperatures, selecting the minimum for the set of modified blackbody curves resulting in a realistic SED curve that reasonably fit the continuum of the IRS spectra. Estimating the maximum L_{bol} is more difficult since we do not know how luminous the IR peak is for our sources, but we can make the assumption that our sources are not going to deviate significantly from the templates. (Though, it is unlikely that any of our sources are going to have far-IR peaks comparable to that of Arp220.) From our three-blackbody fitting method, we found that cold dust temperatures $\lesssim 30\ K$ usually result in extremely luminous far-IR peaks—far more luminous than we expect with these sources. Using very similar blackbody fitting procedures on local ULIRGs, Armus et al. (2007) find 30 K to be approximately the lowest temperature required, agreeing with our determination that a cold blackbody temperature $\lesssim 30\ K$ results in an over-luminous far-IR peak. Using 30 K

Table 2.2. $L_{IR,bol}$ Template Measurements

GO2 ID[a]	Best-Fit Template[b]	FIR Template[c]	$L_{IR,bol}$[d] ($L_\odot$)
1	F00183-7111	Mrk231	$8.7^{+10.7}_{-2.0} \times 10^{12}$
4	F00183-7111	Mrk231	$2.1^{+6.5}_{-0.33} \times 10^{13}$ *
5	F00183-7111	Mrk231	$1.3^{+5.0}_{-0.76} \times 10^{13}$ *
7	Mrk231	Mrk231+M82	$3.3^{+9.2}_{-1.6} \times 10^{13}$ *
9	Mrk231	Mrk231	$6.6^{+17}_{-1.9} \times 10^{12}$ *
10	F00183-7111	Mrk231	$1.1^{+3.3}_{-0.90} \times 10^{13}$ *
14	Mrk231	Mrk231	$1.5^{+8.4}_{-1.0} \times 10^{13}$ *
19	NGC 7714	Mrk231+M82	$7.1^{+14}_{-0.060} \times 10^{12}$
28	Mrk231	Mrk231	$3.2^{+6.1}_{-0.82} \times 10^{12}$
30	Mrk231	Mrk231	$1.3^{+6.4}_{-1.1} \times 10^{13}$ *
31	NGC 7714	NGC 7714	$9.3^{+5.6}_{-4.0} \times 10^{12}$

Note. — Estimated IR luminosities from our template fitting.

[a]GO2 MIPS designation.

[b]Templates used to fit the IRS spectra.

[c]Templates used to fit only the far-IR portion of the source SEDs and thereby estimate the IR luminosities

[d]IR bolometric luminosities. The lower and upper limits were estimated from fitting modified blackbodies to our total SEDs. Upper limits are found by limiting the cold component to 30 K; asterisks indicate sources where the FIR peak was much higher than expected with these sources, and therefore the maxima are probably overestimated by a large amount.

as a limiting temperature for the cold blackbody, we can estimate upper limits for L_{bol}. An example of our blackbody fitting is shown in Figure 2.6 with all of our results listed in Table 3. Asterisks in the table denote those sources where even the 30 K limit appeared to result in an unrealistically luminous IR peak, indicating that the actual upper limit for the bolometric luminosity is likely to be significantly lower than the given upper limit.

As mentioned at the beginning of this section, we used an emissivity coefficient (β) of 1.5. The lack of data in the sub-mm means we cannot constrain the emissivity to specific values for the individual sources. However, we ran our blackbody fitting script for emission coefficients of 1.0, 1.5, and 2.0 and measured the changes in the IR luminosity. While the minimum/maximum IR luminosity did change, the magnitudes of the changes were not significant, so we adopted the median value of $\beta = 1.5$. We conclude that these sources lie in the ULIRG/HyLIRG regime with L_{bol} typically ranging from a few $\times 10^{12} L_{\odot}$ to a few $\times 10^{13} L_{\odot}$, which is consistent with what we found using the templates..

2.4 Discussion

Our template comparisons reinforce previous findings (Houck et al. 2005; Yan et al. 2005; Brand et al. 2007) that these sources are dominated in the mid-IR by obscured AGN emission rather than embedded star formation. If star formation contributed to a higher fraction of the overall far-IR emission, there would be a stronger cold dust component, resulting in higher 160 μm flux densities (for the sources detected) and more overall detections (for those not detected) at that wavelength. While it is possible to get this stronger component by modeling a colder ($\lesssim 30\ K$) blackbody, our source templates and Armus et al. (2007) show that this is unlikely. Also, most of the L_{bol} upper limits for each source using a

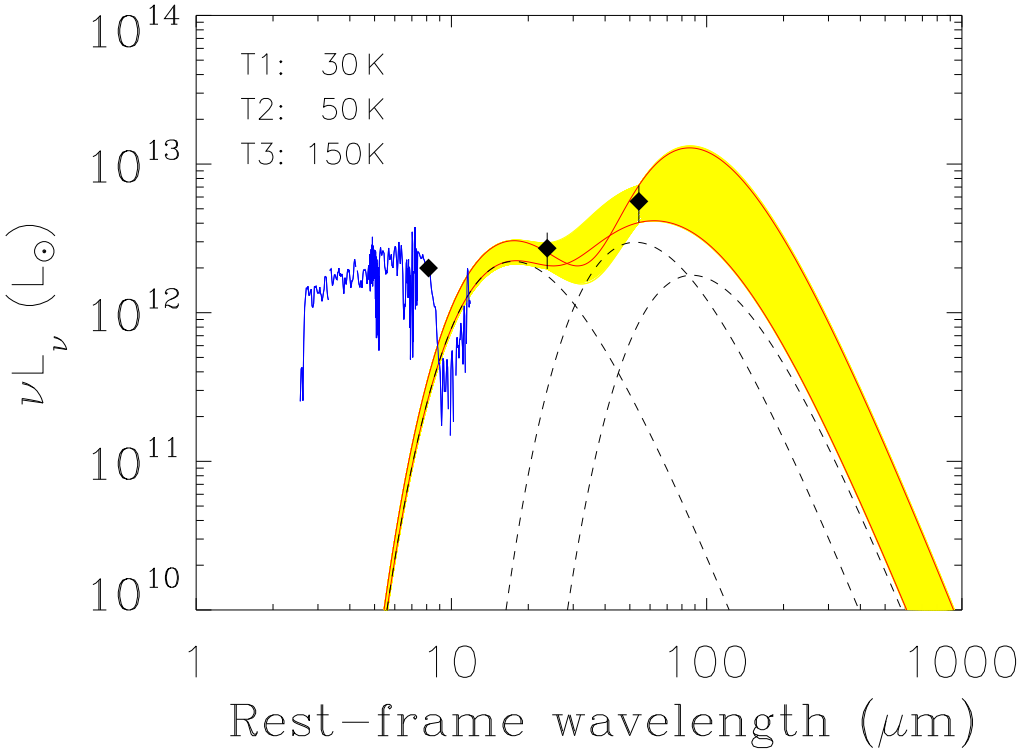

Figure 2.6 Three-blackbody fit for MIPS 001 with a cold dust peak (T1) at 30 K. Plotted are the IRS spectrum (blue) with 24, 70, and 160 μm data points (black diamonds) fit with three modified blackbody curves (dashed lines). The maximum and minimum luminosity curves (red) are plotted, as well as all possible fits to the data at varying luminosities between the minimum and maximum (yellow).

Table 2.3. Constraints on $L_{IR,bol}$

GO2 ID[a]	log(LIR) (60 K)[b]	log(LIR) (50 K)	log(LIR) (40 K)	log(LIR) (30 K)	log(LIR) (radio)[c]	q[d]
1	12.83-13.07	12.84-13.07	12.86-13.12	12.91-13.29	14.25	-0.3
4	13.25-13.41	13.27-13.44	13.31-13.56	13.38-13.93*	13.4	1.0
5	12.86-13.25	12.75-13.28	12.80-13.40	12.94-13.80*	< 13.20	> 1.1
7	13.22-13.45	13.27-13.49	13.30-13.64	13.36-14.10*	< 13.17	> 0.8
9	12.66-13.09	12.69-13.09	12.70-13.15	12.74-13.38	< 12.97	> 0.8
10	12.21-13.20	12.22-13.22	12.27-13.31	12.30-13.64*	< 13.11	> 0.6
14	12.62-13.33	12.64-13.38	12.69-13.53	12.72-13.99*	< 13.23	> 0.7

[a]GO2 MIPS designation.

[b]Columns 2 through 5 indicate IR luminosity (8–1000 μm) ranges for our modified blackbody fitting with the coldest blackbody set at the temperature indicated in the column header.

[c]IR luminosity as estimated from the 20 cm radio flux from each source.

[d]q is defined as the log of the ratio of the 24 μm flux with the 20 cm flux (Houck et al., 2005).

Note. — Minimum and maximum IR luminosities for each of our sources with respect to the coldest blackbody curve used in the fitting. The complete table is available in electronic format.

30 K blackbody reveal it is highly improbable that these objects have such strong emissivity from cold dust, even at wavelengths beyond what we have observed. Owing to a lack of data in the far-IR, we cannot completely constrain emission from cold dust in these sources; however, unless the SEDs of our objects are vastly different from the typical, nearby sources, it is unlikely that there is sufficient star formation to boost the luminosities above $3 - 10 \times 10^{13} L_{\odot}$.

Additionally, we can compare our objects to the de Grijp et al. (1987) classification of IRAS sources. The authors define "warm," AGN-like colors to be in the range $-1.5 \lesssim \alpha(25, 60) \lesssim 0.0$, where $\alpha(25, 60)$ is the spectral index between the 25 and 60 μm flux densities using the conversion $F_{\nu} \propto \nu^{\alpha}$. We calculated the equivalent IRAS25/IRAS60 colors from the MIPS70/MIPS160 measurements, which is a reasonable estimation since our sources are at $z \sim 2$. The original 11 sources have spectral indices of $-1.2 \lesssim \alpha \lesssim -0.78$, easily falling into the warm, AGN-like color range.

It is possible to recreate a warm SED like our sources with an atypical dust distribution, such as a large amount of obscuring material very near a nuclear starburst. This could result in objects with warmer than expected IR emission and subdued far-IR. However, such objects could still have a cold dust peak more similar to what we expect for obscured star-forming galaxies. Even with a warm dust component from a central starburst, we would also expect to see stronger aromatic features. While we cannot completely rule out the possibility, there is little evidence from our data that these objects are dominated by star formation rather than obscured AGN emission.

The conclusion that AGN power the mid-IR is strengthened if we take into account the 12 powerlaw sources. At IRS wavelengths, these objects appear identical to pure AGN—there are no obvious features in the spectra, like aromatic

emission or silicate absorption. It is plausible that most of the powerlaw sources are at similar distances as the sources with known redshifts (Donley et al., 2007). Some may even be of higher redshift, so the mid-IR features are redshifted out of the IRS range. However, Donley et al. (2007) show that even an extreme object similar to Arp220 would appear to be a powerlaw source at $z = 2.8$ only if log $L_{bol} > 13.3\ L_{\odot}$. It would probably require a significant fraction of IR emission from an embedded AGN to reach such high luminosities. Assuming the majority of the pure power law sources are at similar redshifts as the ones with spectral features, as many as 20 of the 23 objects in our sample have their rest mid-IR emission (5–20 μm) dominated by AGNs.

The other three sources exhibit faint aromatic emission features in their IRS spectra or the AGN templates vastly underestimate their far-IR luminosities, suggesting significant star-formation power. We combined an AGN template (Mrk231) with a star-forming galaxy template (M82) in an attempt to model these sources, which appear to have a mixture of AGN and star-formation. While this two-component "model" better matched the aromatic features and overall shape of two sources at than the AGN templates at mid- and far-IR wavelengths, we were unable to account for all of the emission near 160 μm. Despite the large percentage of objects that appear to be AGN-dominated, there are still a few objects with significant star formation.

It is still unknown, however, what role in galactic evolution these objects play. If AGN activity and feedback do indeed stifle star formation activity, this class of objects could give us information on when these sources ceased large-scale star formation. Perhaps we are looking at a time in galaxy evolution where the AGNs in these galaxies are beginning to "turn on." It is also possible that the apparent AGN activity is not continuous but transient, and we are seeing a brief period in

the evolution of these objects.

A similar group of objects as those studied in this paper appears in several SCUBA observations (Chapman et al. 2003, 2005; Egami et al. 2004; Pope et al. 2006). A collection of sub-mm galaxies in a similar redshift range was observed to have comparable luminosities as our objects. However, the 24 μm luminosities of these sources are 5 to 10 times lower than our sources, despite the aromatic emission detected in some of them (Lutz et al. 2005; Rigby et al. 2008). There is a possibility that we are studying two different populations of IR-bright, high-redshift galaxies. As indicated in Chapman et al. (2005), Figure 3, selection effects might be able to explain this dichotomy. SCUBA has a higher probability of detecting cooler sources in the sub-mm range, while *Spitzer* more easily detects the warmer sources in the mid- and far-IR regimes due to the IR peak being shifted to shorter wavelengths (Egami et al., 2004). What is needed to fully understand and explain these two apparent populations of galaxies is observations of similar objects by both SCUBA and *Spitzer* in the same field. It could then be determined if these sources are indeed two distinct populations or similar types of objects merely observed with instruments that only detect sources of particular IR temperatures.

2.5 Conclusions

We observed 20 galaxies from the sample of luminous infrared galaxies from Houck et al. (2005) with the MIPS 70 and 160 μm arrays on *Spitzer* and we computed SEDs for these sources from the mid-IR to radio wavelengths. We fit templates of similar nearby sources to our SEDs to estimate their IR luminosities and to study the possible mechanisms for this emission. We also fit modified blackbodies to our SEDs to estimate the errors in the IR luminosities. We conclude

that virtually all of our sources have luminosities in the 3×10^{12} to $3 \times 10^{13} L_{\odot}$ (ULIRG/HyLIRG) range and that the majority have mid-IR emission dominated by AGNs, with only three displaying a significant amount of star-formation activity in this wavelength region.

CHAPTER 3

THE NATURE OF STAR FORMATION AT 24μM IN THE GROUP ENVIRONMENT AT $0.3 \lesssim z \lesssim 0.55$

(Tyler et al. 2011, ApJ, 738, 56)

Galaxy star formation rates (SFRs) are sensitive to the local environment; for example, the high-density regions at the cores of dense clusters are known to suppress star formation. It has been suggested that galaxy transformation occurs largely in groups, which are the intermediate step in density between field and cluster environments. In this paper, we use deep MIPS 24 μm observations of intermediate-redshift ($0.3 \lesssim z \lesssim 0.55$) group and field galaxies from the GEEC subset of the CNOC2 survey to probe the moderate-density environment of groups, wherein the majority of galaxies are found. The completeness limit of our study is $\log(L_{TIR}/L_\odot) \gtrsim 10.5$, corresponding to SFR $\gtrsim 2.7$ $M_\odot$ yr^{-1}. We find that the group and field galaxies have different distributions of morphologies and mass. However, individual group galaxies have star-forming properties comparable to those of field galaxies of similar mass and morphology; that is, the group environment does not appear to modify the properties of these galaxies directly. There is a relatively large number of massive early-type group spirals, along with E/S0 galaxies, that are forming stars above our detection limit. These galaxies account for the nearly comparable level of star-forming activity in groups as compared with the field, despite the differences in mass and morphology distributions between the two environments. The distribution of specific SFRs (SFR/M_*) is shifted to lower values in the groups, reflecting the fact that groups contain a higher proportion of massive and less active galaxies. Considering the distribu-

tions of morphology, mass, and SFR, the group members appear to lie between field and cluster galaxies in overall properties.

3.1 Introduction

In a ΛCDM universe, galaxies, on average, move from areas of lower density to areas of higher density, merging and combining to form larger and larger systems like the massive galaxy clusters we see in the local universe. Galaxy evolution, therefore, cannot be understood without considering the influence of environment on galaxy properties. The importance of environment on galaxy evolution is demonstrated by the differences between galaxies in clusters and those in the field. For example, the fraction of blue galaxies in clusters has been decreasing since $z \sim 1$, and local clusters are dominated by red galaxies (Butcher & Oemler 1978; Kennicutt 1983; Hashimoto et al. 1998; Andreon et al. 2004; Poggianti et al. 2006; Cooper et al. 2007; Loh et al. 2008; Cucciati et al. 2010). Dressler (1980) found a dramatic increase in the proportion of early-type galaxies with local density inside rich clusters, i.e., the morphology-density relation. This relation has also been shown to extend down to the group environment (Postman & Geller 1984). Most of these cluster early-type galaxies have not had appreciable star formation in gigayears, though as we move outward from the centers of the clusters, we see more late-type galaxies overall and more early-type galaxies that have had more recent star formation (Balogh et al. 1997; Balogh et al 1999, Bai et al. 2009).

Environment is expected to influence the rates of both gas exhaustion and interactions. The drop in star-forming activity in dense environments might be due to interactions with the inter-galactic gas, such as through ram-pressure stripping of cold gas in galaxies (Gunn & Gott 1972; Larson et al. 1980; Kinney et al. 2004) or stripping of the hot gas through strangulation (Balogh, Navarro &

Morris 2000; Kawata & Mulchaey 2008; McCarthy et al. 2008). Alternatively, the lower fraction of star forming galaxies might arise through galaxy-galaxy interactions, either major mergers or harassment (frequent high-speed encounters of galaxies that do not lead to mergers), both of which would accelerate the star formation and lead to early exhaustion of the interstellar material. Tides raised by the overall gravitational potential of dense clusters may also play a role (Henriksen & Byrd 1996). It has been proposed that the morphological transformation into early-type galaxies may occur first, suppressing star formation by stabilizing the gas against fragmentation (Martig et al. 2009), although other recent studies question this idea (Kovač et al., 2010).

Explaining the behavior of galaxies in different environments in terms of consistent theories for the growth of galaxies in the early Universe has proven challenging (Bower et al. 2006; Kaviraj et al. 2009). Therefore, an intense observational approach is needed to help develop an understanding of the relation between environment and galaxy evolution. It should be possible to disentangle environmental influences by comparing galaxy behavior in different environments, though just as the mechanisms for galaxy transformation are not fully understood, the environments where these processes operate also need to be explored and defined. Additionally, most of the previous work regarding star formation with respect to environment focused on rich clusters (e.g., Dressler et al. 2009a; Bai et al. 2009; Haines et al. 2009, and references therein); relatively few studies have focused on groups (e.g. Zabludoff & Mulchaey 1998, 2000; Balogh et al. 2004; Johnson et al. 2007; Marcillac et al. 2008; Bai et al. 2010).

Simard et al. (2009) argue that cluster-centric processes are not the dominant factor in galaxy morphological transformation. The majority of galaxies live in the less-dense group environment (Geller & Huchra 1983; Eke et al 2004), and

because clusters probably form from coalescing groups and field galaxies, much of the evolution apparent in cluster galaxies may have occurred in groups prior to their assimilation into clusters. Zabludoff & Mulchaey (1998) found that the proportion of early-type galaxies in groups ranged from that typical of the field ($\sim$25%) to that found in dense clusters ($\sim$55%), suggesting that much of the morphological transformation of galaxies from field to cluster properties occurs in groups. Just et al. (2010) show that an increase in the proportion of S0 galaxies with decreasing redshift occurs in moderate-mass groups/poor clusters ($\sigma < 750$ km s^{-1}), and Wilman et al. (2009) find that for groups at intermediate redshifts, the fraction of S0s is as high as in clusters, even at fixed luminosities. Additionally, because most galaxies reside in groups—and, therefore, galaxies spend most of their time in groups—uncovering the effects of these lower-density environments can help us understand the evolutionary path of the global galaxy population over cosmic time (McGee et al., 2009).

If morphological transformations frequently occur at intermediate densities, is this also the location where star formation is cut off? Previous studies of star formation in groups have mostly focused on optical indicators such as Hα or [OII]λ3727 emission lines or ultraviolet continuum. These measures can extend to low levels of star formation, and they indicate a significantly lower level of activity in groups and clusters than in the field (Wilman et al. 2005a; Gerke et al. 2007; Balogh et al. 2009; Iovino et al. 2010; Peng et al. 2010). Such first-order comparisons are usually made under the assumption that the extinction is similar in groups and clusters (and that star formation is not deeply obscured). However, corrections are required to convert these optical indicators to accurate star formation rates (SFRs). At z $\gtrsim$ 0.3, Hα moves out of the range of optical spectroscopy and SFR estimates rely on [OII], where the extinction is large and uncertain. The

[OII]$\lambda 3727$ line has additional problems of being sensitive to dust reddening and metallicity, thus being relatively weak in high-mass systems, although empirical corrections have been suggested to correct for this and other effects (Moustakas et al. 2006; Gilbank et al. 2010).

The infrared (IR) is advantageous for probing high levels of star formation. While SFRs determined in the IR are only sensitive to dust-obscured star formation, the correction to the total star formation in objects at moderate to high luminosities ($L_{TIR} \gtrsim 1 \times 10^{10}$ $L_\odot$) is small (Rieke et al., 2009). Nonetheless, previous IR studies have not reached consistent conclusions about star formation in groups. Marcillac et al. (2008) found no significant dependence on the incidence of luminous infrared galaxies as a function of field or group environment at z $\sim$ 0.8. At lower redshifts, Wilman et al. (2008) find a dearth of star formation in group galaxies at z $\sim$ 0.4, while Tran et al. (2009) find a similar incidence of SFRs in massive groups (for galaxies forming stars $> 3M_\odot$ yr^{-1}) as in the field at z $\sim$ 0.37. For local groups, Bai et al. (2010) report rates of star formation somewhat lower than in the field (by $\sim$30%).

This paper is a step toward understanding the influence of the group environment on star formation and resolving some of the apparent discrepancies in previous studies of the same topic. Some of these discrepancies, especially in cluster studies, may arise from "field" samples contaminated by groups. To compare groups with actual field galaxies, we need a clean field sample with as many galaxies as possible. Here, we present 24 μm measurements of 232 group galaxies and 236 field galaxies from 0.3 $\lesssim$ z $\lesssim$ 0.55 in the Second Canadian Network for Observational Cosmology (CNOC2) survey.

The paper is organized as follows. In Section 2, we discuss the sample, data reductions, and errors. Section 3 covers the construction of fractional IR luminosity

functions and compares the IR luminosities, morphologies, and masses of group and field galaxies to estimate what effect (if any) environment has on star formation at these redshifts. We discuss the implications of our results in Section 4. For all cosmological corrections, we assume the parameters H_0 =70 km s^{-1}Mpc^{-1}, $\Omega_M = 0.3,\ \Omega_\Lambda = 0.7$.

3.2 Sample & Data Reduction

3.2.1 Sample Selection and Photometry

The CNOC2 survey is a photometric and spectroscopic survey of faint galaxies covering more than 1.5 deg^2 over four widely-spaced patches of sky (Yee et al. 2000; Carlberg et al. 2001a). The original survey included five-color photometry in I_C, R_C, V, B, and U to $R_C \sim 23.0$ (Vega) mag and spectroscopic redshifts (to $R_C \sim 21.5$ mag) for an unbiased sample of ∼6000 galaxies with the purpose of studying galaxy clustering, dynamics and evolution at intermediate redshifts ($0.1 \lesssim z \lesssim 0.6$). The survey is spectroscopically incomplete, but the selection function is very well defined for this redshift range (Lin et al. 1999; Yee et al. 2000).

The groups themselves were originally selected by using a friends-of-friends algorithm to find overdensities of galaxies in 3-D space (Carlberg et al. 2001a,b). Follow-up LDSS2 spectroscopy (to $R_C \sim$ 22.0) targeted 26 of these Carlberg groups at $0.3 \lesssim z \lesssim 0.55$, creating a sample of group and field galaxies to a greater depth than the original sample, with increased and unbiased spectroscopic completeness (Wilman et al., 2005b). Additional group members were carefully selected to ensure that the resulting sample would be unbiased with regard to color using the method outlined in Wilman et al. (2005a). This subset of the original CNOC2 survey—26 groups at 0.3 $\lesssim$ z $\lesssim$ 0.55 to $R_C \sim$ 22.0—was followed up by

the Group Environment and Evolution Collaboration (GEEC), and hereafter, we refer to these as the GEEC groups. Visual (Wilman et al., 2009) and automated (McGee et al., 2008) morphological classifications were made using deep, high-resolution HST ACS images of the same 26 groups (Wilman et al. 2009). Additional multiwavelength coverage includes GALEX UV (McGee et al., 2011), and IRAC (Balogh et al. 2007, 2009; Wilman et al. 2008). X-ray properties of a subset of the groups have been measured with XMM-Newton and Chandra observations (Finoguenov et al., 2009).

We present observations of these GEEC groups (as defined by Wilman et al. (2005a)) using the MIPS 24 μm band on the *Spitzer Space Telescope* (Rieke et al., 2004). We used MIPS in single-source photometry mode (field of $5' \times 5'$) due to the compact nature of the groups, and long exposure times allowed us to detect relatively low SFRs (< 10 $M_\odot$ yr^{-1}). All but five of the groups have either complete coverage of their members with MIPS or are only missing one or two member galaxies. All galaxies assigned to groups using the algorithm described by Wilman et al. (2005a) and within the MIPS field of view are considered group members in this paper. The MIPS 24 μm field of view corresponds to $\sim$1.3 Mpc ($\sim$2 Mpc) on a side at $z = 0.3$ (0.55).

The data from these observations were reduced using version 3.10 of the MIPS Data Analysis Tool (DAT; Gordon et al. 2007). Fields with overlapping regions were mosaicked for better coverage near the image edges. Sources 3σ above the standard deviation of the background were identified using DAOFIND (Stetson, 1987) in the IRAF[2] environment. Flux densities were calculated using a PSF made from bright sources in one of the larger mosaicked fields and the IRAF PSF-fitting routine ALLSTAR, correcting for flux lost in the wings of the PSF as described by

[2]IRAF is distributed and supported by the National Optical Astronomy Observatories (NOAO).

the Spitzer Science Center[3].

Our initial field sample consisted of all galaxies not identified as residing in a group. Given the completeness of the group sample, it has been estimated that ∼21% of this field sample is contaminated by unidentified groups (Carlberg et al. 2001a, McGee et al. 2008). To reduce the amount of group contamination in the field, we plotted a running-average histogram of redshifts for the LDSS2 pencil-beam fields with a bin size of z = 0.001. Any galaxies that fall in a bin with five or more galaxies at any point in the running average were removed from the field sample as possible group contaminants. This method will obviously remove some true field galaxies, as it does not account for the spatial positions of the possible group galaxies; however, this is a quick, simple method for removing galaxies that are likely to live in groups. We removed a total of 78 galaxies—or ∼25%—of our original field sample.

These observations of groups and the "cleaned" field sample (referred to simply as the "field" from this point on) result in 24 μm measurements or upper limits for 232 group galaxies and 236 field galaxies from $0.3 \lesssim z \lesssim 0.55$, of which 79 group galaxies and 65 field galaxies are detected. Our absolute detection limit (3σ) is 119μJy, corresponding to the 24 μm observations with the highest background. These observations result in a detection limit for the groups of of $L_{TIR} \sim 3.5 \times 10^{10}$ $L_\odot$ (SFR $\sim$ 3.3 $M_\odot$ yr^{-1}), where L_{TIR} is the total IR luminosity as defined by Rieke et al. (2009). However, only two groups (20 galaxies) have detection limits at this level; ∼91% of our group sample (and ∼93% of the field sample) have 24 μm coverage to a lower detection limit: $L_{TIR} \sim 2.9 \times 10^{10}$ $L_\odot$ (SFR $\sim$ 2.7 $M_\odot$ yr^{-1}). We use this lower value as our detection limit for the rest of the paper. At a

[3]The Spitzer Science Center (http://ssc.spitzer.caltech.edu) is supported by NASA, the Jet Propulsion Laboratory, the California Institute of Technology, and the Infrared Processing and Analysis Center.

typical redshift for our groups (z $\sim$ 0.43), L^*_{TIR} corresponds to SFR $\sim$ 10 $M_\odot$ yr^{-1} (Rujopakarn et al., 2010). The typical optical surface density of the GEEC groups is $\sim$3 galaxies Mpc^{-2} for galaxies with $M_{B_J} <$ -20, though it ranges from $\sim$1 to $\sim$6.5. Cluster surface densities can range from these values in the outskirts to as high as several hundred galaxies Mpc^{-2} in the dense cores (Dressler, 1980).

3.2.2 Uncertainties and Reliability

We cross-correlated the sources detected at 24 μm (almost 2000 objects over all fields) with the GEEC spectroscopic catalog to within 3 arcseconds; if multiple optical sources were located within 3 arcseconds of a 24 μm source, the nearest optical source was used (only 20 instances of such multiple matches using the entire 24 μm and CNOC2 catalogs were recorded). Any GEEC galaxy not matching this criterion was given a 3σ upper limit. To estimate the 1σ errors (and 3σ upper limits for non-detected sources) in the 24 μm flux densities, we put down apertures in blank areas of the fields and took the standard deviation of the nearest 20 background apertures to a given source.

Because of the depth of our observations and the size of the MIPS 24 μm PSF, it is necessary to know the fraction of false detections—in other words, the fraction of 24 μm sources incorrectly attributed to an optical source in our catalog. We therefore placed a random number of fake sources (up to 300 sources per pointing, which at z = 0.55 equates a surface density of 4 Mpc^{-2}) on each image and matched the 24 μm detections to both the fake source catalog and our GEEC spectroscopic catalog. We use three different match radii—4, 3, and 2.5 arcsec—and found the mean fraction of false detections to be 3.1, 1.8, and 1.3%, respectively, for each match radius. As expected, the number of false detections per unit area is relatively constant and does not change significantly for each match radius. We could use any of the listed match radii and not change the number of false

matches substantially (i.e. from $\sim$3 to $\sim$7 for the group and field samples individually, out of $\sim$230 galaxies in each environment, and from $\sim$2 to $\sim$5 for the cleaned field). However, if we use too small a match radius ($\lesssim$ 2.5 arcsec), we risk eliminating real matches. At our typical detection levels of $\sim$4–5σ, the RMS positional errors at 24 μm are $\sim$1.5 arcsec. Additionally, from examination of our HST ACS images (see the Appendix for more information), we discovered that using a matching radius of 4 arcsec could introduce more false detections than anticipated due to the crowded nature of our group-dominated fields. For these reasons, we used the 3 arcsec matching radius. A 3 arcsec matching radius results in $\sim$4.2 incorrectly matched galaxies for the groups and $\sim$2.7 for the cleaned field for all galaxies. If we assume that all of the mis-matched galaxies are detected at 24 μm, we would have upper limits that $\lesssim$ 5.6% and $\lesssim$ 6.5% of detected group and field galaxies, respectively, are incorrectly matched.

We also need to keep in mind that we are comparing group and field galaxies en masse, not individually. False detections will affect the groups and field each the same way, and so will not bias our results provided the number of false detections remains low, which we have already shown to be the case. As such, the matching technique (and match length of 3 arcsec) is sufficient for our purposes.

3.3 IR Properties of Sample Galaxies

Extreme environments, such as the interior regions of clusters, clearly quench star formation in galaxies and reduce their IR outputs (e.g., Bai et al. 2009). Based on the ages of their dominant stellar populations and distributions of morphologies, galaxies in rich groups and clusters must have a similar evolution, at least at low redshift (Balogh & McGee, 2010). This suggests that galaxy transformation occurs in groups as well as in clusters. To test for such behavior, we compare the frac-

tional IR luminosity function in groups with that of field galaxies at intermediate redshifts.

3.3.1 Methodology

To compare the IR output and SFR of group and field galaxies, we estimated the SFR and total IR luminosity (L_{TIR}) from the 24 μm flux densities using the method described by Rieke et al. (2009), who use *Spitzer* data to create a group of luminous star-forming galaxy templates more complete in the near- and mid-IR than previous templates.

Our method for determining SFR and L_{TIR} is only accurate for purely star-forming galaxies. Obscured AGN can also emit a significant fraction of their light in the mid-IR. To identify possible AGN contaminants in our sample, we compared our 24 μm-detected galaxies with *Chandra* detections. Four of the galaxies in the CNOC2 sample were identified as AGN with clear X-ray detections, though all four were field galaxies outside of our redshift range (i.e. not in our GEEC sample). However, some AGN may be so buried that we are not able to detect them at our current X-ray detection threshold. More importantly, slightly less than half of the groups targeted by MIPS have X-ray coverage, so there may still be some AGN contaminating our sample. Given the few AGN detected with the existing data and in previous studies of AGN activity in groups (Dwarakanath & Nath 2006; Silverman et al. 2009), we expect this number to be small.

To correct for the different redshifts of our group and field galaxies, we used the derived luminosity evolution of IR galaxies from Le Floc'h et al. (2005), who show that IR galaxies as a whole evolve in luminosity as $(1+z)^{3.2}$ from $z \sim 0$ to $z \sim 1.2$. We evolved our group and field galaxy IR luminosities to a fiducial redshift ($z = 0.5$) to remove redshift bias in our sample. This IR luminosity evolution is for all IR galaxies regardless of environment; however, the Le Floc'h et al. (2005)

sample (as for most field samples) is expected to be ∼50% groups, ∼50% true field galaxies, making this model reasonable for our purposes. This conclusion is supported by the lack of significant differences in the field and group fractional luminosity functions as discussed below.

3.3.2 Results for IR-Active Galaxies

3.3.2.1 IR Luminosities and Star Formation Rates

In Figure 3.1 we present L_{TIR} (left axis) and SFR (right axis) with respect to redshift for all galaxies in the CNOC2 survey for which we have MIPS 24 μm detections. Group galaxies are shown as solid red circles, while field galaxies are open blue circles and the X-ray identified AGN are overplotted as green triangles. The average detection limit for all of our 24 μm fields is shown by the solid black curve; the redshift limits of our GEEC group and field sample are denoted by dashed lines ($0.3 \lesssim z \lesssim 0.55$). The group and field IR-active populations do not appear significantly different.

Figure 3.2 gives us a clearer picture of the group and field populations in terms of L_{TIR}. We plot histograms of the normalized distributions of L_{TIR} (which we will refer to as fractional luminosity functions, fLFs, from here on) for the group and field galaxies (red filled circles and blue open circles, respectively). The dashed line indicates our 24 μm detection limit for all field galaxies, while the dotted line is the detection limit for all group galaxies. The fractions in each bin (y-axis values) are normalized by the number of 24 μm-detected galaxies in each environment and corrected for spectroscopic incompleteness as a function of magnitude. Weights were computed using the method outlined in Appendix A of Wilman et al. (2005a), except in this case we do not correct for any radial dependent selection, which tends to overweight galaxies on the outskirts of groups.

We have also corrected for completeness with respect to the 24 μm data. We

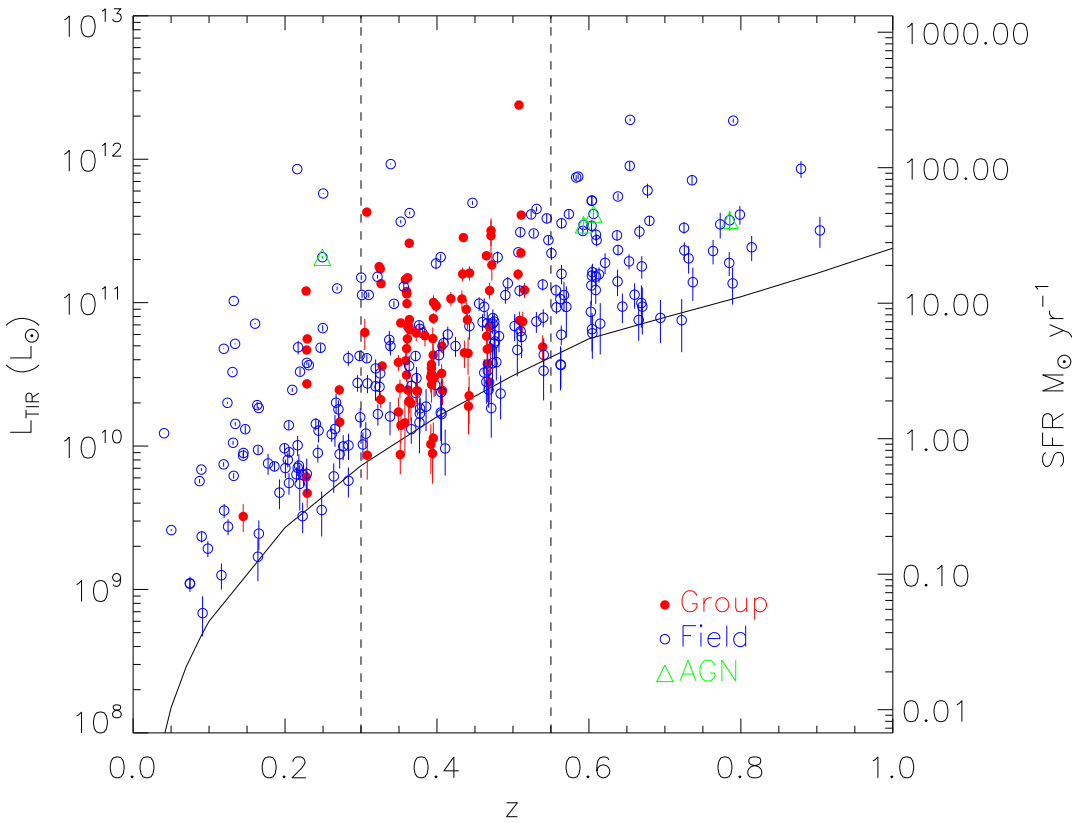

Figure 3.1 L_{TIR} and SFR versus redshift for all galaxies detected at 24 μm. The red filled circles are group members, the open blue circles are field galaxies, and the overplotted green triangles are X-ray-detected AGN. The dashed lines indicate the redshift range of our group and field sample ($0.3 \lesssim z \lesssim 0.55$). The solid line indicates the average 24 μm 3σ detection limit for our observations.

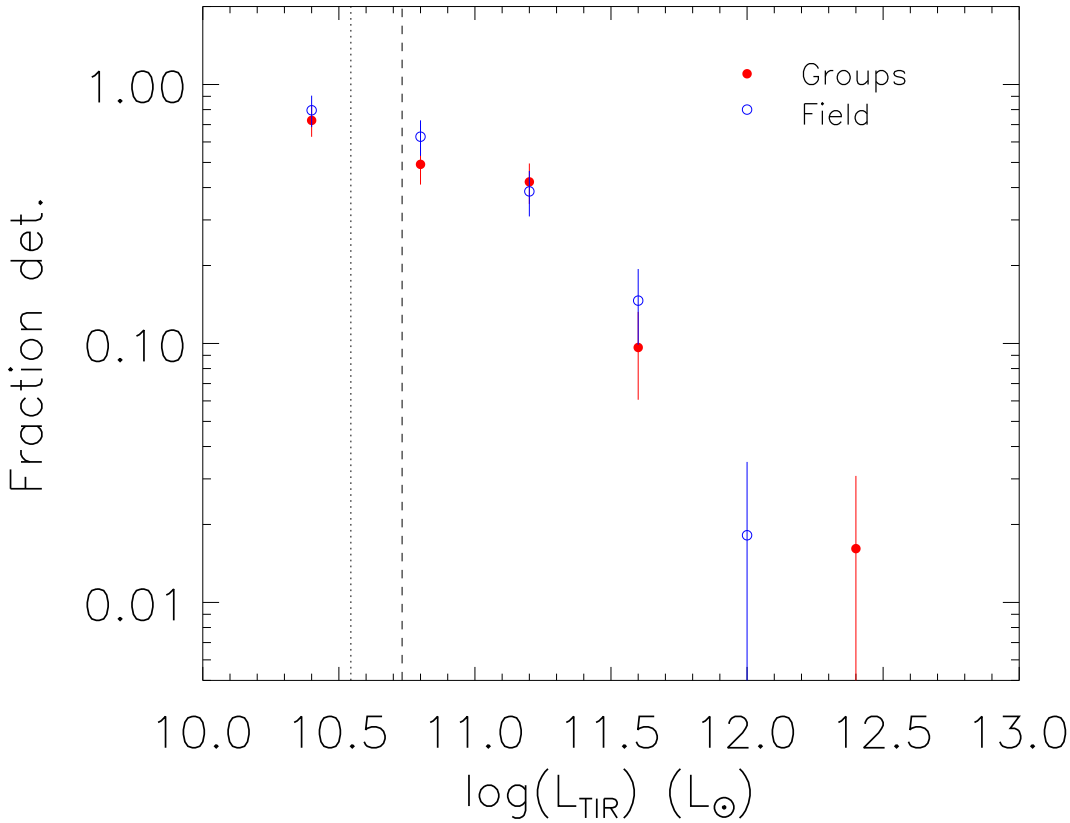

Figure 3.2 L_{TIR} histograms (what we refer to as fractional luminosity functions, fLFs) for the groups (red filled circles) and field galaxies (blue open circles) with Poisson errors. The galaxies included are those detected at 24 μm in the redshift range $0.3 \lesssim z \lesssim 0.55$. Each fLF is corrected for spectroscopic and 24 μm completeness and has been normalized by the number of IR-detected galaxies in each environment. The vertical dashed line is the detection limit for the field galaxies; the vertical dotted line is the detection limit for all the group galaxies. Up to $\log(L_{TIR}/L_{\odot}) \sim 12$, the group and field fLFs are almost identical, given the error bars. The data for the group and field galaxies below the detection limits are also in agreement, though there will be some bias as the group and field galaxies are not equally complete. Above $\log(L_{TIR}/L_{\odot}) \sim 12$, we are limited by low number statistics, as there are only a couple group and field galaxies at these luminosities.

calculated the 24 μm incompleteness by estimating the SFR corresponding to the detection limits for all galaxies in each image. We then found the fraction of group and field galaxies (separately) with SFR detection limits below a given SFR; the inverse of this fraction in each bin corresponds to our 24 μm completeness weighting. The completeness corrections for the points shown above both of these limits are small: factors of $\lesssim 1.7$ for both the group and field galaxies.

The group and field galaxy fractional luminosity functions are identical within the error bars up to $\log(L_{TIR}/L_{\odot}) \sim 12$. The last two bins contain few galaxies, so we cannot compare the bright end with much certainty. The measurements slightly below our detection limit should not be significantly biased given the care to avoid bias in the sample selection (Wilman et al., 2005a) and that the vast majority of the group and field galaxies have detection limits below the indicated limit; therefore, we can say that these data also agree within the error bars with some certainty. Overall, the fLFs suggest there is little difference between the groups and the field (with respect to L_{TIR}). Given that there are similar numbers of spectroscopically-identified galaxies in the groups and field in this redshift range, even the overall normalization will be the same. This seems to indicate that the group environment is not responsible for suppressing or enhancing star formation amongst the actively star-forming population. To confirm the apparent similarity of the group and field samples, we performed a two-sample Kolmogorov-Smirnov test on the unbinned fLFs (the raw L_{TIR} distributions) in both environments. The K-S test indicated a $\sim$99% probability that the two distributions can come from the same parent sample. Due to the coupling between L_{TIR} and SFR through L(24 μm) (Rieke et al., 2009), the results are the same if we plot SFR instead of L_{TIR}.

To better quantify the two LFs themselves, we fit both with a Schechter func-

tion, minimizing χ^2. Log($L^*/L_\odot$) for the groups and field, respectively, are 11.9 $\pm$ 0.5 and 12.3 $\pm$ 0.3, a difference of $\sim$0.4 dex, though, given the error bars, the two environments are similar. Tran et al. (2009) find the opposite trend: their supergroup L^* is $\sim$0.4 dex higher than the field. The faint-end slope alpha does not differ significantly between the two environments either. We find alpha to be 2.9 $\pm$ 1.1 and 4.3 $\pm$ 1.2 for the groups and field, respectively.

Figures 3.1 and 3.2, and our statistical analysis of the results, suggest that the group environment does not substantially quench or enhance star formation at intermediate redshifts for the IR luminosities we are studying. Could the environmental effects be more prominent in the larger groups? To test this possibility, we plot the number of group members brighter than M_{B_J} = -20 versus L_{TIR} (luminosity-evolved to z $\sim$ 0.5) in Figure 3.3. The open circles are individual galaxies, and the filled red circles show the mean L_{TIR} in three bins for all detected group galaxies with 1σ error bars. For reference, most groups have velocity dispersions less than 500 km s^{-1} while the largest group is $\sim$740 km s^{-1}([4]). We see no trend in 24 μm-detected galaxies with respect to group size, and the differences between the mean IR luminosity values is not significant. Therefore, within the L_{TIR} limit of our sample, group size does not strongly affect the IR luminosity of the member galaxies. This is interesting given that interactions are thought to be a major source of star-formation quenching in groups (given that higher densities are needed for other quenching mechanisms like ram-pressure

[4]The group membership determination to the limiting magnitude is complete to the $\sim$70-90% level, so variations in the completeness are not large enough to affect the basic result shown in the figure. Ideally, we would compare L_{TIR} directly with group mass determined from the velocity dispersions, but for values below $\sim$350 km s^{-1} the velocity dispersions can significantly underestimate the group mass (Nolthenius & White, 1987). Additionally, for small groups, the orientation angle of the group on the sky may add uncertainty in translating the velocity dispersion to the mass (Plionis & Tovmassian, 2004). The velocity dispersions for some of our groups have large formal errors, and a significant fraction of the groups may also not be virialized (e.g., Bai et al. 2009, Hou et al. 2009).

stripping and strangulation), and the number of galaxies that have experienced past interactions and mergers should be larger in more massive groups, which have more members.

Our results are in agreement with many recent studies of clusters. At similar redshifts to our groups ($0.4 \lesssim z \lesssim 0.8$), Finn et al. (2010) find that clusters have IR LFs very similar to the field. This seems to be true with local clusters, as well (Bai et al. 2006, 2009), indicating that IR-active galaxies in clusters have been recently-accreted and have not yet had time to become affected by the more dense environment of the cluster. Cortese et al. (2008) find that the UV LF of the Coma cluster is indistinguishable from the field; however, they argue this is due more to color selection effects than environmental processes. We believe that the GEEC R_C selection does not cause significant selection effects, but further study would be needed to determine how this R-band selection might affect our results.

3.3.2.2 Star Formation with Respect to Mass

While the total IR luminosities and SFRs of the group galaxies do not appear different from the field, there could be trends with stellar mass. The most massive galaxies in dense regions of the local universe, such as cluster cores, are old ellipticals, whereas the most massive field galaxies are blue spirals. What about groups at intermediate redshifts?

The stellar masses used here are presented in McGee et al. (2011), but briefly, we use spectral energy distribution (SED) fitting of all available photometry. The details of the photometry were presented in Balogh et al. (2009) but typically involved K, i, r, g, u, NUV and FUV. We compare this observed photometry to a large grid of model SEDs constructed using the Bruzual & Charlot (2003) stellar population synthesis code and assuming a Chabrier initial mass function. We follow Salim et al (2007) in creating a grid of models that uniformly samples the al-

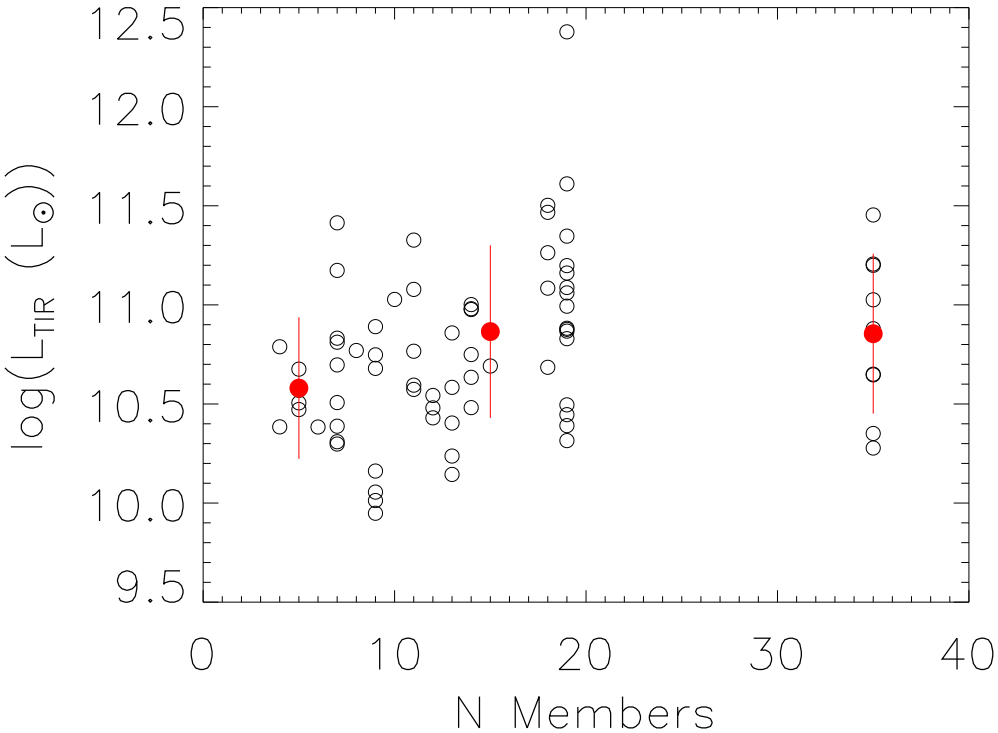

Figure 3.3 L_{TIR} of group galaxies detected at 24μm (luminosity-evolved to z $\sim$ 0.5) versus the total number of members in each group brighter than M_{B_J} = -20. The open black circles are individual galaxies; the red filled circles are the mean L_{TIR} and 1σ error bars for groups in three different bins. The total IR luminosity for individual group galaxies does not depend on the size of the group. In other words, we see no trend in star-formation levels with group richness.

lowed parameters of formation time, galaxy metallicity, and the two components of the Charlot & Fall (2000) dust model. The star formation history is modeled as an exponentially declining base rate with bursts of star formation randomly distributed in time, which vary in duration and relative strength. We produce model magnitudes by convolving these model SEDs with the observed photometric bandpasses at 9 redshifts between 0.25 and 0.6. Finally, we minimize the χ^2 while summing over all the models and taking account of the observed uncertainty on each point. By comparing to other estimates of stellar mass we estimate that 1σ uncertainties are on the order of 0.15 dex.

We investigate SFR with respect to stellar mass in Figures 3.4 through 3.6. Figure 3.4 shows SFR plotted with respect to stellar mass for the group (red filled circles) and field (blue open circles) galaxies. Only galaxies above our 24 μm detection limit (dashed line) are shown. Because our sample is only unbiased for $\log(M_*/M_\odot) \gtrsim 10$, we average the SFRs for each environment in three mass bins above this limit. These averages are plotted as black filled triangles for the groups and black open triangles for the field. Unlike the previous figures, the field has a different distribution than the groups. Noeske et al. (2007) compare SFR and stellar mass for 24 μm-identified "field" galaxies in a similar redshift range ($0.2 \lesssim z \lesssim 0.7$) and find a linear relation between SFR and stellar mass with a slope of $\sim$0.67. They did not distinguish between group and field galaxies, however, so their "field" is a combination of the two environments. We compared our galaxies with theirs by plotting this relation as a solid, black line (with an arbitrary normalization). Our group and field galaxies, combined, seem to echo the Noeske et al. (2007) relation, with the suggestion that galaxies in the field obey a steeper mass-SFR relationship than those in groups (mainly driven by the lack of high-mass galaxies with SFR just above our detection limit in the field, a region

populated by group galaxies).

In Figure 3.5, we plot a "specific SFR function" (SFR M_*^{-1}) in the same manner as Figure 3.2, though only including galaxies with SFR $\gtrsim$ 2.7 $M_\odot$ yr^{-1}. Each histogram has been normalized so that its total is 1. Differences between the group and the field are suggested; a two-sample K-S test reveals that the two distributions have only a 27% probability that they are drawn from the same parent sample. The groups have more IR-active galaxies with less star formation per stellar mass than the field galaxies, as expected given the overall higher masses of the group galaxies. Put another way, for the IR-detected galaxies in the groups, the on-going star formation makes a smaller relative contribution to the stellar mass than for galaxies in more isolated environments. Thus, the average timescale for growth of the stellar mass ($M_*/\dot{M}_*$) is currently smaller in the field than in group galaxies by a factor of $\sim$3. In the past, however, it is possible that this timescale was shorter in the groups given their galaxies have shifted to higher masses by z $\sim$ 0.5.

Figure 3.6 compares stellar mass and SFR in a slightly different way. The top plot shows the fraction of 24 μm-detected field and group galaxies as a function of specific SFR (sSFR) with $\log(M_*/M_\odot) < 10.5$, labeled as blue dashed and red solid lines, respectively. The lower panel is the same plot except for galaxies with $\log(M_*/M_\odot) > 10.5$. The histograms in this figure have been normalized in the same manner as Figure 3.5. We see that group and field galaxies have similar ranges of sSFRs in either mass bin, but the higher-mass galaxies in the field tend to form stars at higher rates (higher-mass group galaxies have lower relative SFRs). A two-sample K-S test results in a $\sim$3% probability that the low-mass ($\log(M_*/M_\odot) < 10.5$) group and field galaxies come from the same parent sample and a $\sim$89% probability for the high-mass group and field galaxies ($\log(M_*/M_\odot)$

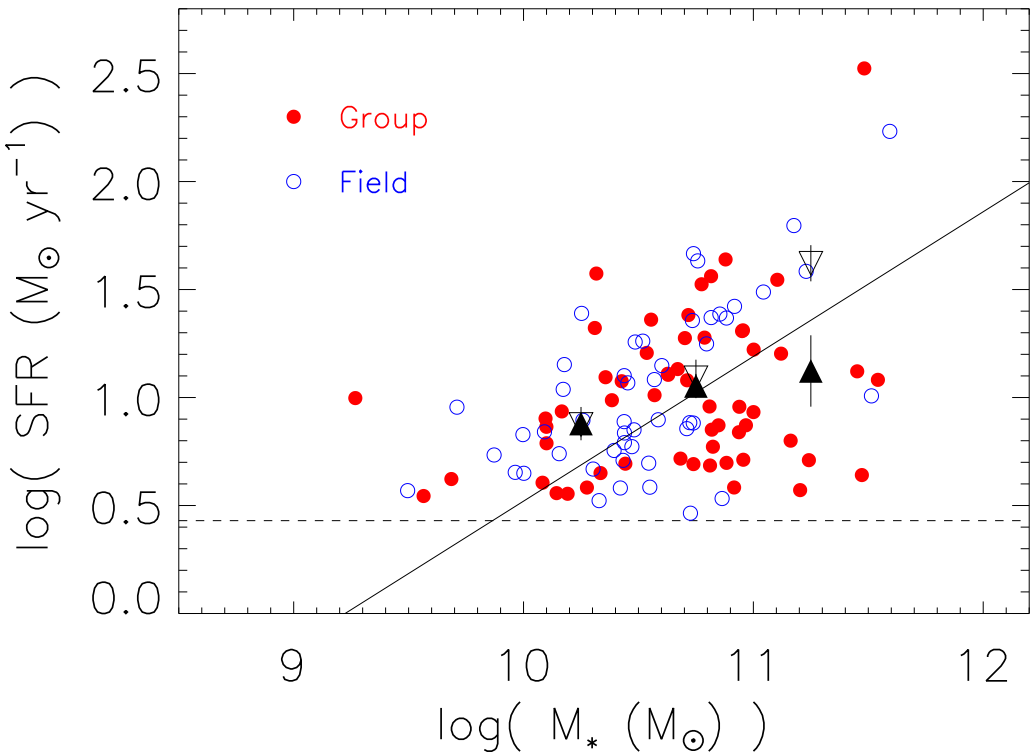

Figure 3.4 Stellar mass versus SFR for IR-detected galaxies in groups (red filled circles) and the field (blue open circles). We only show galaxies above our 24μm detection limit, which is shown by the dashed line. The black filled triangles (black open triangles) are the mean SFR for the groups (field) in three mass bins above $\log(M_*/M_\odot) = 10$. The field and group galaxies have different distributions. The solid line represents the trend found by Noeske et al. (2007) for 24 μm identified "field" galaxies at $0.2 \lesssim z \lesssim 0.7$ (plotted here at an arbitrary normalization). Because Noeske et al. (2007) did not distinguish between group and field galaxies, their trend is likely a combination of the two environments.

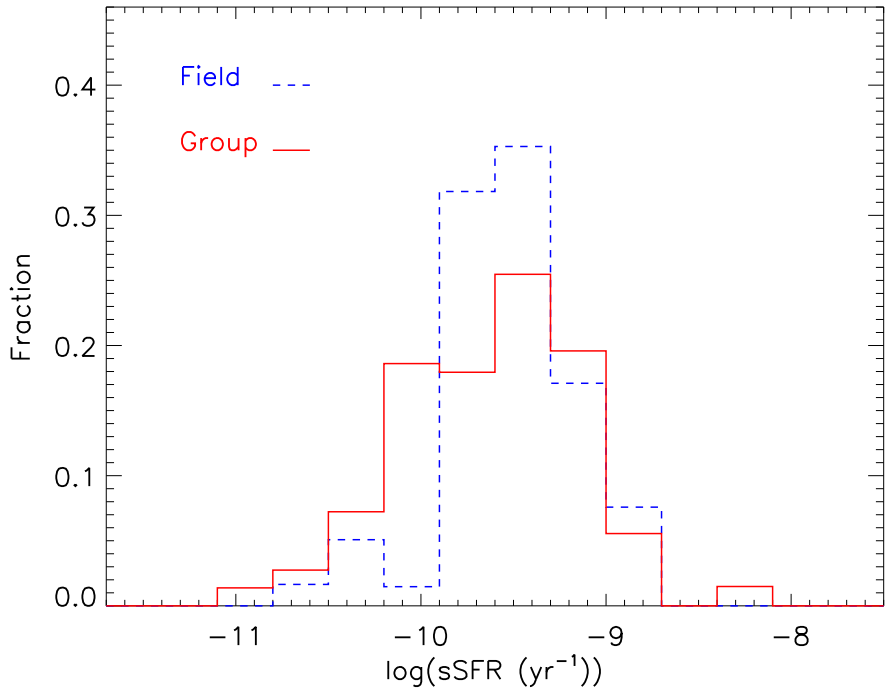

Figure 3.5 Histograms of specific star formation rate (SFR M_*^{-1}) for IR-detected galaxies (SFR $\gtrsim$ 2.7) in groups (red solid line) and the field (blue dashed line), all corrected for spectroscopic and 24 μm incompleteness. Each histogram has been normalized so its total value is 1. The groups have more galaxies at higher masses than their field counterparts, resulting in lower specific SFRs for the groups. This difference is not highly significant, however: a two-dimensional KS test results in a 27% probability that these two data sets come from the same distribution.

> 10.5). While neither of these cases indicate a 3σ result, it makes sense given Figure 3.4, which shows a trend of higher-mass group galaxies having significantly lower SFRs as compared with the field. The subtle trends seen in Figure 3.5 and Figure 3.6 may be showing the beginning stages of suppression of star formation in the groups.

In Figure 3.7, we split our group and field galaxies in terms of their SFRs with respect to stellar mass. The top plot shows the fraction of what we call "low-activity" galaxies (SFR < 2.7 $M_\odot$ yr^{-1}) normalized by the total number of galaxies per mass bin in the groups (red solid line) and field (blue dashed line). The two highest mass bins in the groups house a total of three galaxies, all of which are in groups with 10 or fewer members, so any trend in the number of low-activity, high-mass group galaxies does not appear to be significant. As a result, the group and field galaxies are similar in terms of the fraction of low-activity galaxies for a given stellar mass. The bottom plot shows the fraction of galaxies in each environment with SFR > 10 $M_\odot$ yr^{-1} with the same normalization as the top plot. We do potentially see a stronger difference between the group and field galaxies at these higher SFRs: the groups have galaxies forming stars at this high rate at a variety of masses, while the field galaxies peak at $\log(M_*/M_\odot) \sim 11$. This may be another indication of a stronger mass-SFR relation in the field than in the groups, though the differences between the group and field galaxies here are of low significance.

We performed a Monte Carlo analysis of the data in the top plot of Figure 3.7 to estimate whether the overall fraction of low-activity galaxies, at constant stellar mass, is significantly higher for group galaxies. We found the total number of group galaxies per mass bin and randomly selected the same number of galaxies per mass bin from the field, making a fake group sample. We then made the

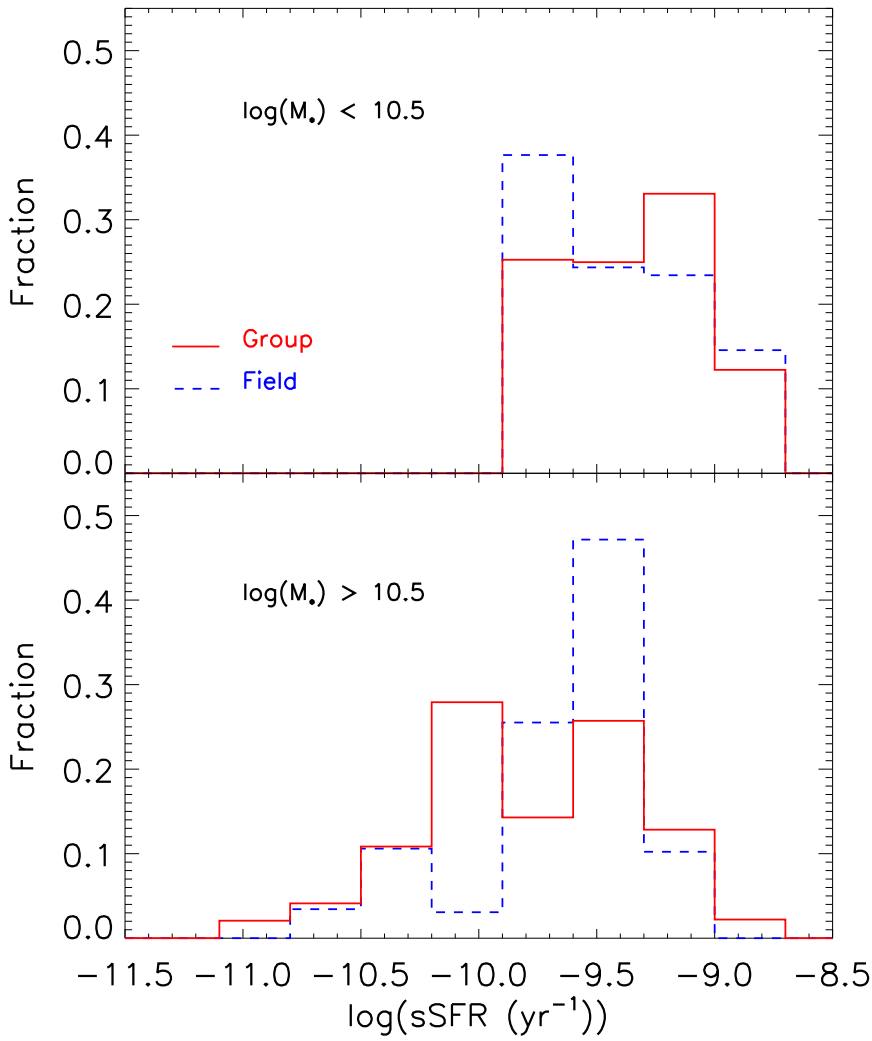

Figure 3.6 Histograms of specific SFR for the field and group galaxies with $\log(M_*/M_\odot) < 10.5$ (top plot) and > 10.5 (bottom plot), with the same normalization and completeness corrections as the previous figure. While the ranges of sSFRs for both environments are similar, we can see a weak trend whereby massive field galaxies have higher sSFRs than the groups. This same trend was evident in Figure 3.4, where we can see that the groups tend to have more massive galaxies with lower SFRs than the field. A two-sample K-S test comparing the high-mass group and field galaxies results in a $\sim$3% probability that the two populations come from the same distribution, and the low-mass group and field galaxies have an 89% probability of coming from the same distribution.

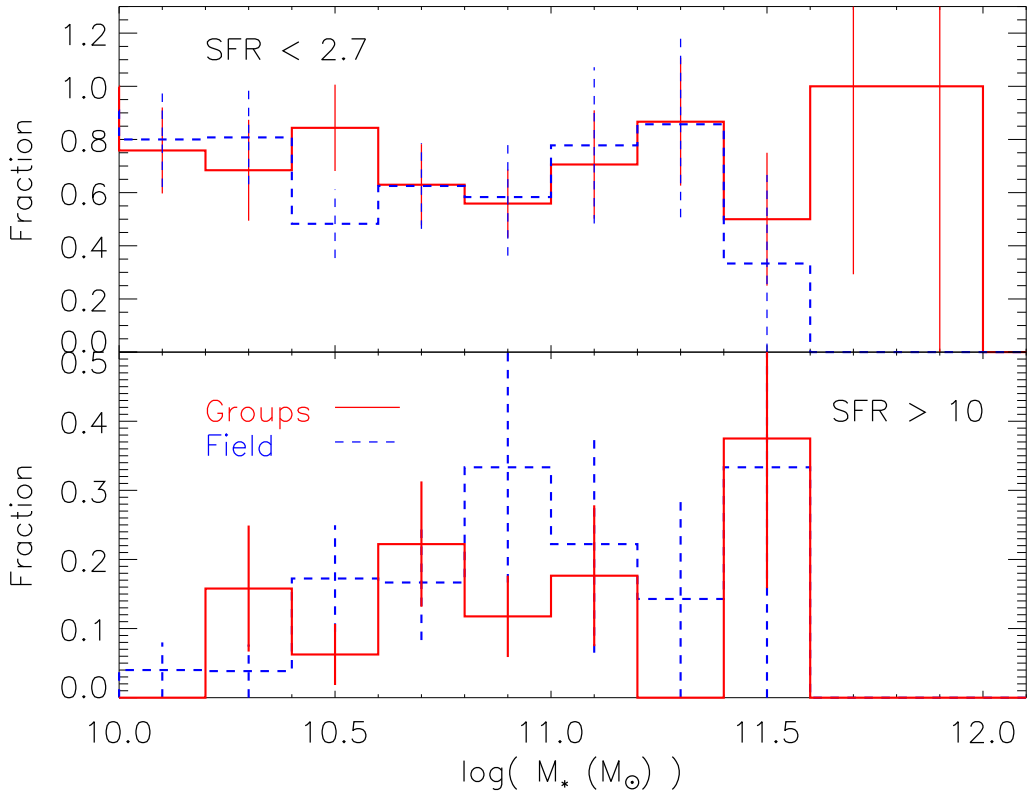

Figure 3.7 Fractions of low- and high-activity galaxies with respect to environment. The top plot shows the fraction of galaxies with SFR < 2.7 $M_\odot$ yr^{-1} normalized by the total number of galaxies in each environment, respectively, per mass bin. For stellar masses below $\sim$11.5, the groups and the field are nearly identical; above this limit, however, the groups have a few massive, low-activity galaxies while the field has none. (This is not significant, as there are only three galaxies in the two highest mass bins for the groups.) The bottom plot shows the fractions of galaxies with SFR > 10 $M_\odot$ yr^{-1} for each environment, respectively. We see a stronger difference between the group and field galaxies here than in the top plot: the groups have galaxies forming stars at this high rate at a variety of masses, while the field galaxies peak at $\log(M_*/M_\odot) \sim 11$. This may be another indication of a stronger mass-SFR relation in the field than the group galaxies, though the significance is small.

same plot as the top part of Figure 3.7 using the fake group galaxies: the fraction of fake low-activity galaxies normalized by the total number of galaxies per mass bin. We repeated this 500 times, each time calculating the mean fraction of low-activity galaxies from $10 \lesssim \log(M_*/M_\odot) \lesssim 11.6$. (Higher masses were not possible given the lack of field galaxies in the highest mass bins.) Because the fraction of low-activity galaxies in the groups and field in this mass range is fairly constant with mass, the average is an accurate way of comparing the fake and real group galaxies. This distribution of fake group averages is plotted as a histogram in Figure 3.8; it is fit well by a Gaussian (solid curve). The mean of the real groups (real field) is shown as a dashed (dotted) line. The fake groups have consistently low averages as compared with the real groups, though this difference is only significant to a 1σ level. Interestingly, the resampled field (matched in mass to the group population) has a mean low-activity fraction equivalent to the non-resampled field, indicating that the dependence of low-activity fraction on mass within this range is negligible (also evidenced by the lack of a trend in Figure 3.7).

Another way to describe these results is that, if we use the field mass-SFR relation to determine the expected IR luminosity distributions in groups, we would conclude that the groups are slightly under-luminous because of their higher proportion of high-mass galaxies. Marcillac et al. (2008) study the environment of $0.7 \lesssim z \lesssim 1.0$ luminous and ultra-luminous IR galaxies (LIRGs and ULIRGs, respectively), and they find that, at similar masses, 32% of all the galaxies in their sample reside in groups, and 32% of their LIRGs and ULIRGs also reside in groups. Where we find a small and barely significant difference, their study indicates none. That is, this reinforces our conclusion that the group environment does not suppress or enhance star formation in the galaxies as a whole. Though we do see indications of suppression in the groups when we compare sSFRs, the difference

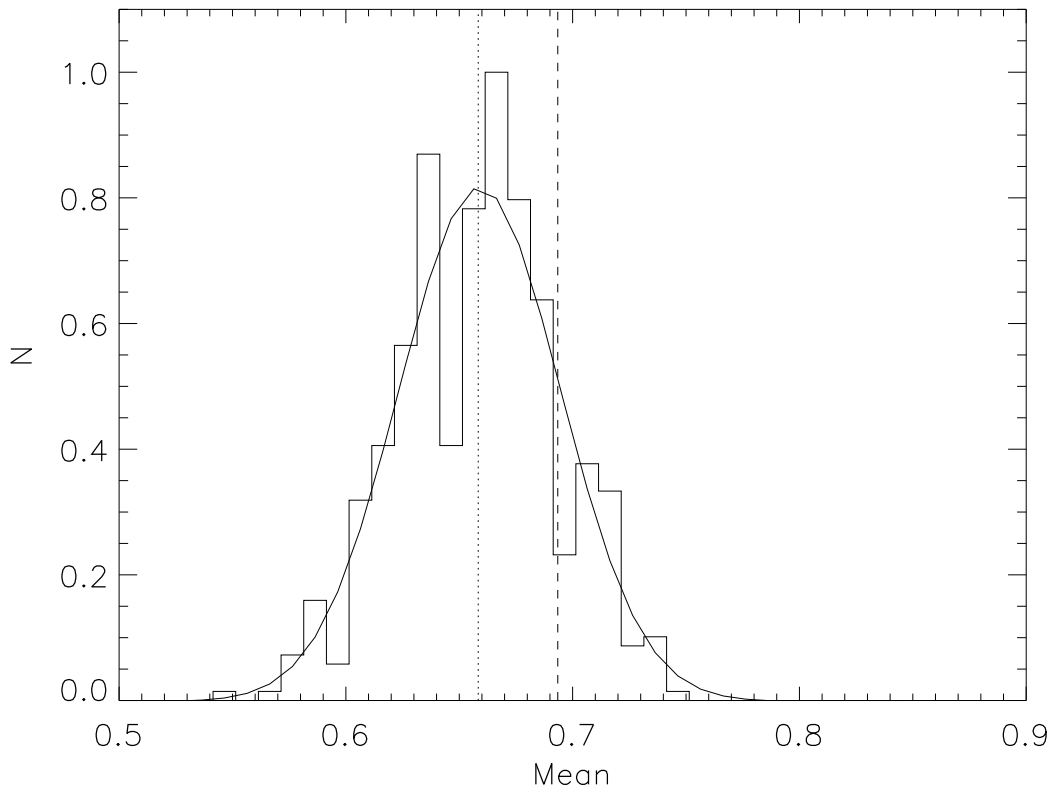

Figure 3.8 A quantitative assessment of the top plot in Figure 3.7 (see text for a more specific explanation). We created fake group samples from the field and calculated the average fraction of low-activity galaxies from $10 \lesssim \log(M_*/M_\odot) \lesssim 11.6$. The histogram shows the distribution of these averages for 500 fake group samples. The dashed (dotted) line is the average fraction of low-activity galaxies in the real groups (field). The fake groups have consistently low averages as compared with the real groups, but this difference is only significant at a 1σ level, as shown by the Gaussian fit to the distribution (solid curve).

is subtle and might depend on the low-mass regime where we are incomplete (galaxies with lower SFRs than we were able to detect with MIPS), or other variables.

3.3.2.3 Morphologies

Another parameter subject to transformation in dense environments is galaxy morphology. Is there any difference in morphology types with respect to star formation between the group and field galaxies? Wilman et al. (2009) report on the visual morphologies of the GEEC groups and field galaxies using high-resolution ACS data. They find the two environments tend to harbor different types of galaxies: S0 galaxies are more prevalent in groups than in the field at a fixed luminosity, indicating that suppression of star formation and bulge growth have been more common in the group environment. Overall, for galaxies brighter than $M_{r_0} =$ -21, they find that the groups have about 1.5 times the number of E/S0 galaxies as the field (Wilman et al., 2009).

We compared the visual morphologies with our IR SFRs using the Wilman et al. (2009) classifications. Thus, "early-type spirals" (eSp) are galaxies classified as Sa through Sbc (including barred spirals), and "late-type spirals" (lSp) are classified as Sc through Sm (including barred spirals). The fractions of IR-detected galaxies with optical classifications (both groups and the field) are as follows: 13% of ellipticals, 10% of S0s, 60% of eSps, 33% of lSp, 15% of irregulars, 17% of mergers, and 61% of galaxies identified as "peculiar." It is perhaps a surprise that eSps are twice as likely to be detected at 24μm as lSps, but this difference may arise because of the lower masses of the later galaxy types.

These conclusions can be tested with quantitative morphology metrics, such as the Concentration, Asymmetry, Clumpiness (CAS) method (Abraham et al. 1994, 1996; Conselice et al. 2000, 2003; see also McGee et al. 2008 for other meth-

ods). At z $\sim$ 0.5, surface brightness dimming might become a problem when identifying spirals, particularly late-types, as the fainter spiral features become indistiguishable from the background. Shi et al. (2009) have shown how to correct concentration and asymmetry (referred to as CA from now on) for the effects of surface brightness dimming to provide unbiased metrics at and above the redshifts of our groups. We have used their methodology to calculate CA for our sample of field and group galaxies, as shown in Figure 3.9 (small black dots). In the top plot, the average values (and error bars) for the groups and field galaxies are given by the red square and blue star, respectively. The dashed line is an arbitrary division roughly separating early- and late-type galaxies that we discuss below. Consistent with Wilman et al. (2009), our results indicate a tendency for group galaxies to have, on average, a higher concentration and lower asymmetry (indicative of E and S0 galaxies) than in the field.

Of 144 galaxies detected at 24 μm, seven are Es and four are S0s. Three of the galaxies are classified as "peculiar," which means they have been visually identified as either having an interacting neighbor or a morphology slightly disturbed from the given classification, and one galaxy is listed as an S0/Sa (most likely an S0 but also has Sa qualities). Still, it is unusual to find any E or S0 galaxies with SFRs at these levels. To be certain the early-type galaxy detections are robust, we investigated other possibilities for the IR emission.

The first issue concerns our source matching: is it possible there are nearby (projected) neighbors that are being mis-matched with the E/S0 galaxies? As discussed in the appendix, inspection of the ACS images shows that a few of the early-type galaxies have close neighbors, making identifying which galaxy in the field of view is responsible for the IR emission difficult. To be conservative, we rejected any early-type galaxies where the IR emission could be coming from an-

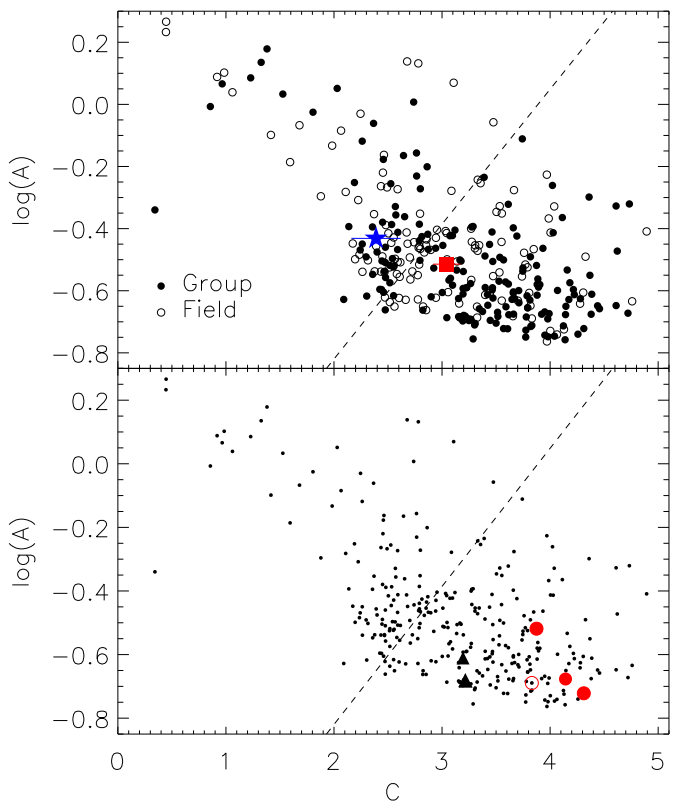

Figure 3.9 Top: Asymmetry versus concentration for group (black filled circles) and field (black open circles) galaxies, calculated in the same manner as Shi et al. (2009). These two parameters allow quantitative assessments of galaxy morphology (as opposed to qualitative visual classifications that can be biased by surface brightness dimming). Average values are shown as a red square (groups) and blue star (field), with error bars. The dashed line in both plots is an arbitrary division between the majority of the group and field galaxies, where most of the galaxies below this line are visual early-types and most of the galaxies above this line are late-types. This plot confirms the trend in the visual morphologies: the groups have a higher fraction of early-type galaxies than the field. Bottom: Same galaxies as the top figure (small black dots) with certain galaxies highlighted. Our six IR-active E/S0 galaxies are shown as red circles/black triangles, respectively, with group early-types having filled symbols and field galaxies having open symbols. All six E/S0 galaxies fall in the area of the plot populated by early-type galaxies, showing that these IR-active galaxies are indeed early-types.

other object. After removing these ambiguous E/S0 detections, we were left with four ellipticals and two S0s firmly detected at 24 μm. We also double-checked our matching of the 24 μm positions with the IRAC 3.6 μm coordinates. Four of the six E/S0 galaxies have IRAC coverage, and all of them match the IRAC coordinates within 1.5 arcsec or less. Because we have imposed very stringent requirements to claim a detection, six detected E/S0 galaxies represents a lower limit.

As a double-check on the morphologies, we again plot asymmetry and concentration for all galaxies with CA values (small, black circles) and the six IR-active early-type galaxies (red circles for ellipticals and black triangles for S0s, with filled points indicating a group galaxy and empty points indicating a field galaxy) at the bottom of Figure 3.9. All six galaxies fall in the "early-type" area of the plot, and they also all fall well under our early-/late-type dashed line. It appears that these six E/S0 galaxies are indeed early-types with bright 24 μm emission.

There is one other culprit that could be masquerading as star formation, however: AGN. Of the six early-type galaxies with confirmed IR emission, only two have X-ray coverage, though neither of them are detected down to $L_X \sim 10^{41}$ erg s^{-1} (Mulchaey et al., in prep). As an additional test for AGN, we look to the IRAC data. The intersection of the stellar light and the warm/cool dust components produces a dip in the SED at rest-frame $\sim$5 μm for normal star-forming galaxies. Buried AGN heat the dust to higher temperatures, which "fills in" this dip. If our IR-detected early-type galaxies have similar colors at IRAC wavelengths to the typical galaxies in our sample, then AGN are probably not contributing significantly to the mid-IR emission. In Figure 3.10 we plot IRAC [3.6]-[4.5] and [3.6]-[5.8] versus redshift for all galaxies with IRAC coverage in our sample. Most

of the galaxies fall into a narrow color range in both plots, indicating that we are probing the Rayleigh-Jeans tail of the stellar bump. If the 24 μm emission were dominated by an embedded AGN, these colors would be more positive due to the warm dust filling in the "dip" in the SED, causing the SED to brighten as we move through the IRAC bands. None of the early-type galaxies detected at 24μm (with IRAC coverage) show the signature of an AGN in the IRAC colors.

Two of our six IR-bright early-type galaxies do not have X-ray or complete IRAC coverage. We have enough SED coverage of one of these two to make out some of the stellar bump and the increase in dust emission in the IR, which seems to indicate star formation instead of an AGN, but it is difficult to say with certainty. The other source has too few photometric data points to make any solid conclusion; however, given the lack of AGN we have found so far in our entire sample, it seems that AGN are a rarity. While we cannot be certain these two galaxies do not host AGN, it seems unlikely.

Thus, even by these stringent tests, we have detected four elliptical and two S0 galaxies at 24 μm, none of which have an obvious AGN contribution. Five of these galaxies (3 ellipticals and 2 S0s) are in groups. We cannot tell whether the groups and field are different in this regard at a statistically significant level. However, among the IR-detected group members, $\gtrsim$ 6% are early types. That is, some early-type galaxies in groups were forming stars at significant levels around z $\sim$ 0.5. We can compare this behavior with that of local early-type galaxies using the study of Devereux & Hameed (1997). They extracted IRAS 60 μm detections of galaxies in the Nearby Galaxies Catalog (NBGC; Tully 1989), which contains 2367 galaxies within 40 Mpc ($H_0 = 75$ km s^{-1} Mpc^{-1}). After eliminating ones not covered by IRAS or compromised for other reasons, 2094 remained in this study, of which 1215 were detected by IRAS (including 22% of the 151 ellipticals). We

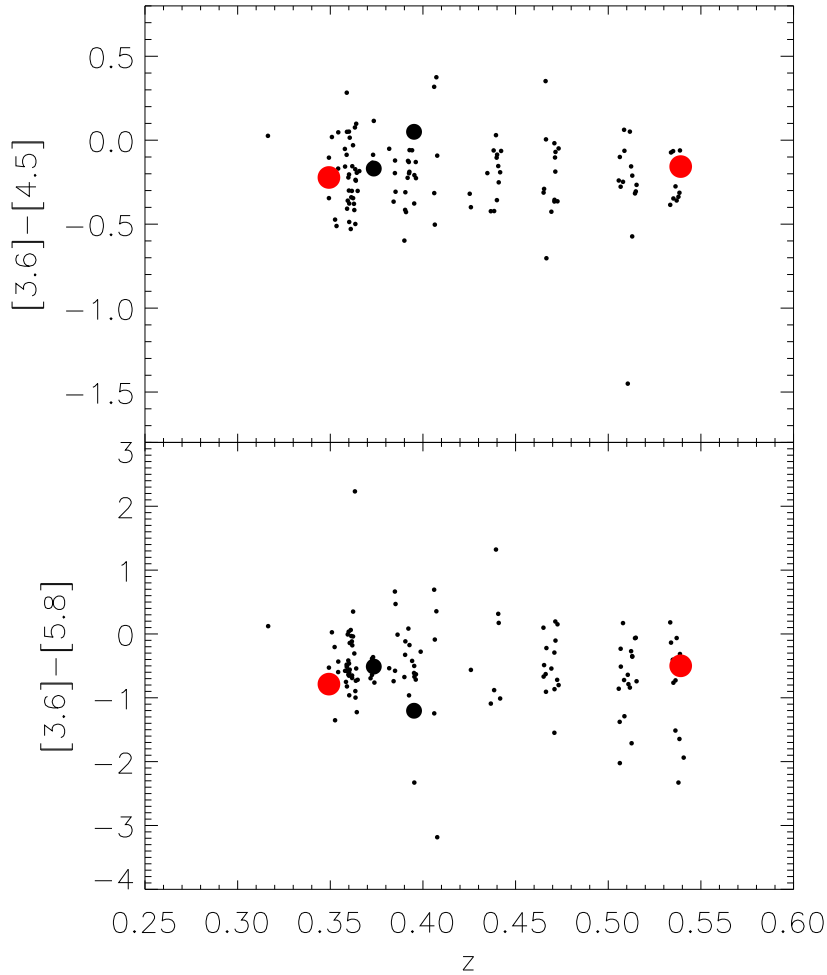

Figure 3.10 IRAC colors [3.6]-[4.5] (top) and [3.6]-[5.8] (bottom) versus z for all galaxies in our sample with IRAC coverage in those bands (small black circles). Also included are four of the six IR-active early-type galaxies that have IRAC coverage. The S0 galaxies are denoted by medium-sized black circles while the ellipticals are denoted by large red circles. Galaxies dominated in these bands by warm dust from an AGN will have highly negative values of [3.6]-[4.5] and [3.6]-[5.8] due to the SED brightening through the IRAC bands. The four E/S0 galaxies with IRAC coverage lie with the rest of the "normal" galaxies, showing that the 24 μm emission from these galaxies is dominated by star formation and not AGN activity.

determined the 99th percentile of 60 μm luminosity for the E–E/S0 and S0–S0/a categories and converted it to L_{TIR} of 2.4 $\times$ 10^9 $L_\odot$ and 2.3 $\times$ 10^{10} $L_\odot$, respectively. The corresponding SFRs are 0.27 and 2.6 $M_\odot$ yr^{-1} (Rieke et al., 2009) and are indicated in Figure 3.11 by dashed and dotted lines, respectively. Figure 3.11 also shows stellar mass versus SFR for all galaxies in our sample detected at 24 μm (small black dots), separated by environment, with visual morphologies indicated by a variety of symbols. The SFRs for the two group S0 galaxies are at or just below the 99th percentile for local S0–S0/a galaxies, while the SFRs of all four E galaxies exceed the 99th percentile for local E–E/S0 galaxies by factors of 3 to 20, an unexpected result given that there are less than 100 early-type group members in our sample.

On a more general note, these measurements imply that not all early-type galaxies are dead at z $\sim$ 0.5; many are still in the process of forming stars, indicating a larger amount of evolution with redshift than previously thought (e.g. Larson 1974; Chiosi & Carraro 2002). While it does appear that there are still some early-type galaxies forming stars in the local universe (Temi et al., 2009), the ubiquity of IR-active early-types in group and field environments remains largely unknown. We do know, however, that star formation in E/S0 galaxies has been decreasing since z $\sim$ 1. Kaviraj et al. (2008) find that star formation in early-type galaxies has decreased by $\sim$50% since z $\sim$ 0.7, and they show that local early-type galaxies, while largely quiescent now, have had spurts of star formation in their recent past. Thus, the enhancement of star-forming activity in early-type galaxies at z $\sim$ 0.5 compared with the present epoch may apply generally for field and group members.

We now discuss the fraction of 24 μm-detected galaxies with respect to the full range of morphologies, separated by groups and field. As just discussed, for

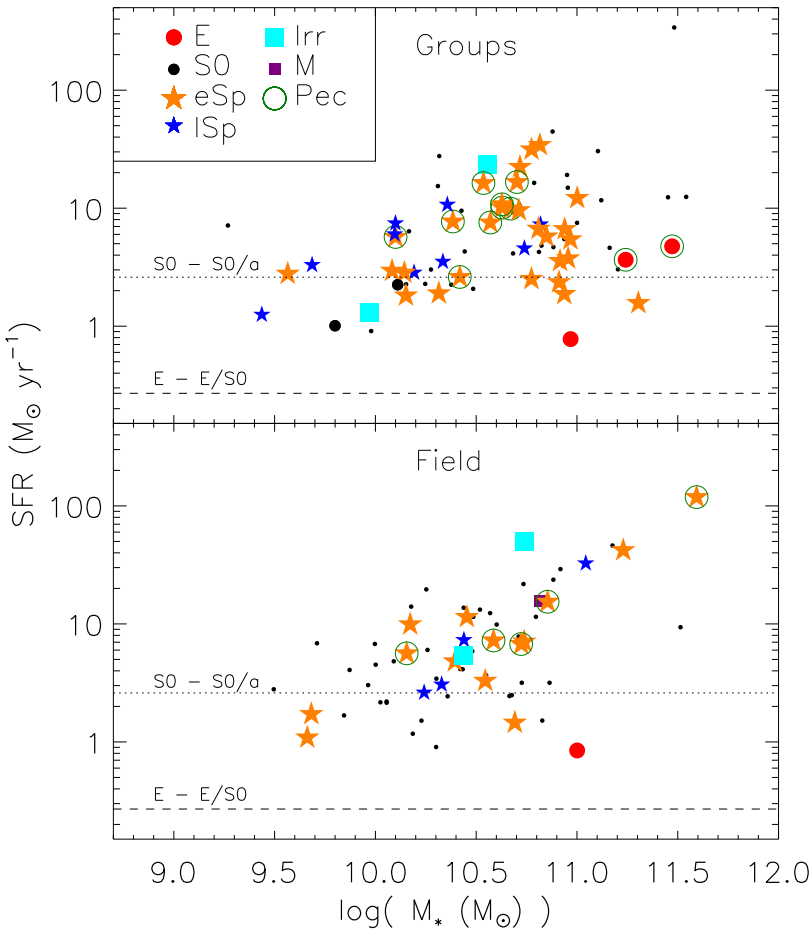

Figure 3.11 SFR versus stellar mass for all galaxies detected at 24 μm (small black dots), separated by environment. Visually-classified morphologies, where available, are identified by different point styles and colors. Ellipticals, S0s, and early-type spirals tend to have higher masses than the other galaxy types, as expected. The 99th percentile of 60 μm luminosity for E–E/S0 and S0–S0/a galaxies in the Nearby Galaxies Catalog (Tully, 1989) correspond to 0.27 $M_\odot$ yr^{-1} (dashed line) and 2.6 $M_\odot$ yr^{-1} (dotted line), respectively. All of the ellipticals detected at 24 μm fall far above the SFR seen in local ellipticals, while the two S0s fall close to the 99th percentile for local S0s.

E/S0 galaxies, 5 out of 75 in groups were detected at 24 μm (7%) and 1 out of 22 in the field (5%). Early-type spirals behave similarly in the two environments: 29 out of 47 group galaxies were detected (62%) compared with 14 out of 23 (61%) in the field. For late-type spirals, 9 out of 19 (47%) are detected in groups and 4 out of 20 (20%) in the field. Although there is a hint of a larger incidence of late-type galaxies with high SFRs detected in our group sample, there are no differences at a significant level.

3.4 Discussion

There is strong agreement that the dense environments in the cores of clusters do have a large effect on their member galaxies in terms of star formation. Marcillac et al. (2007), Patel et al. (2009), and Koyama et al. (2010) show that the densest regions of the clusters RXJ 1716.4+6708 and RXJ 0152.7-1357 strongly suppress star formation. Using the CNOC1 cluster galaxy sample ($0.2 \lesssim z \lesssim 0.55$), Balogh et al. (2000) find that the mean galaxy SFR decreases with decreasing radius from the center of the cluster, and Ellingson et al. (2001) shows a decrease in the fraction of blue and emission-line galaxies and an increase in the fraction of ellipticals as one approaches the cluster core. Similarly, for the more distant cluster MS 1054-03 ($z \sim 0.8$), Bai et al. (2007a) observed that star formation in member galaxies near the core was substantially suppresed; Vulcani et al. (2010) find the same suppression in cluster galaxies from $0.4 \lesssim z \lesssim 0.8$ as compared with the field, though the reduction in SFR was more modest in those clusters. Locally ($z \lesssim 0.3$), we continue to see star-formation quenched or suppressed near cluster cores: Haines et al. (2009) find suppression for star-forming cluster galaxies (defined by $L_{IR} > 10^{10}$ $L_\odot$), as do Bai et al. (2006) and Bai et al. (2009), who report that star-forming galaxies (defined by SFR $\gtrsim 0.2$ $M_\odot$ yr^{-1}) are much less likely to be

found in the cores of local clusters Coma and A3266. Biviano & Katgert (2004) use kinematics of different cluster galaxy morphologies to show that late-type spirals are more likely to be found at higher distances from the core.

Although the SFR suppression in cluster cores is clearly established, work to-date has not reached a firm conclusion about the comparison of group galaxies with those in the field and in clusters with respect to the IR regime. Wilman et al. (2008) find, from 8 μm measurements of a subset of the GEEC sample, that the SFR is significantly suppressed in groups as compared with the field at z $\sim$ 0.4. Bai et al. (2010) use 24 μm observations to show that local groups have somewhat suppressed SFRs compared with the field, and somewhat elevated ones compared with clusters (though they have a lower SFR limit than our study). At higher redshifts, Marcillac et al. (2008) use a large sample of galaxies in the Extended Groth Strip (EGS) to find that LIRGs and ULIRGs measured at 24 μm do not preferentially exist in higher-density environments (including groups) at z $\sim$ 0.9. Tran et al. (2009) use 24 μm data to find a substantially (four times) higher incidence of active star-forming galaxies in groups compared with clusters at z $\sim$ 0.37. They also find that the groups and field are similar in this regard for their luminosity-limited sample. Patel et al. (2009) use 24 μm measurements to find a progressive suppression of the SFR by an order of magnitude from the field to cluster core densities.

Other recent studies in optical bands show suppression of star formation in groups due to different mechanisms. Peng et al. (2010) and Kovač et al. (2010) use SDSS and zCOSMOS galaxies at a variety of redshifts (up to z $\sim$ 1) and environments to show that the effects of environment on individual galaxies are separate from the evolution and quenching with increasing galaxy mass. This "mass quenching" is the dominant effect at high galaxy masses ($M_* \gtrsim 10^{10.2}$ $M_\odot$),

while other effects, like environmental quenching, dominate for low-mass and satellite galaxies ($M_* \lesssim 10^{10}$ $M_\odot$) (Peng et al., 2010). As mentioned previously, Tran et al. (2009) find comparable fractions of star-forming galaxies in their supergroup and the field for a luminosity-limited sample, but their mass-selected sample shows the supergroup has about half the fraction of star-forming galaxies as the field.

In light of the uncertainties in the effects of groups on the SFRs as reflected in the Spitzer 8 and 24 μm data, we have carried out a thorough study of the CNOC2 groups at $0.3 < z < 0.55$, which are exceptionally well-characterized and have substantial amounts of ancillary data. The large sizes of this group sample and of the accompanying field sample also allow reasonably good statistics for our conclusions. We find that the incidence of 24 μm emission is virtually the same in these groups as in the field. This result agrees well with that of Tran et al. (2009) for their luminosity-selected supergroup at z = 0.37 but has higher statistical weight because our field sample is significantly larger. This agreement is interesting because Tran et al. (2009) studied super-groups with large velocity dispersions and significant X-ray luminosities, while our groups generally have lower velocity dispersions and no X-ray emission.

This similarity of IR properties appears to hold in detail, both in the forms of the fractional luminosity functions and as characterized by L^*. The overall fractional luminosity functions for groups and field are consistent with being drawn from the same distribution. Tran et al. (2009) found that L^* for their field sample was $\sim$ 0.4 dex lower than for their groups. To look for this effect, we used our fLF Schechter function fits to determine L^* for our groups. L^* for our field is marginally larger (again $\sim$0.4 dex) than the groups, though given the error bars on the values of L^*, the field and group L^* are comparable. It is possible that

the difference between the two studies arises from the different environments—one large group-like structure for Tran et al. (2009) versus our individual, smaller groups. However, given the statistical significance of the two studies, it is plausible that there is no significant overall difference in L^* between the two environments. This emphasizes the lack of any strong dependence of group member properties on the size or mass of the group (Wilman et al. 2005b; this work).

The IR properties of our group and field galaxies appear to be contrary to the shift in the distribution of galaxy morphologies toward early-types in groups (McGee et al. 2008; Wilman et al. 2009), which we confirm with a form of CA analysis. In part, this apparent contradiction can be explained by the presence of a number of E/S0 galaxies that are detected at 24 μm; this IR activity appears to arise from elevated levels of star formation as compared with local E/S0 galaxies (as also found by Tran et al. (2009)). However, this behavior has also been seen at similar redshifts in field early-type galaxies (e.g., van der Wel et al. 2007; Pérez-González et al. 2008). Along with a higher population of E/S0 galaxies, the groups also have larger overall numbers of massive, early-type spirals. These galaxies contribute significantly to the numbers of IR-detected group members and to the group luminosity function. Tran et al. (2009) find a similar result for their super-group: that an excess population (compared with the field) of spirals fills in the dearth of star formation that would otherwise exist because of the larger proportion of early-type galaxies. A minor difference is that the Tran et al. (2009) group sample is rich in relatively low-mass star-forming spirals compared with those in our groups.

An interesting observation is that there are only two galaxies total in our group and field sample that can be classified as ULIRGs (Ultra-Luminous Infrared Galaxies; $12 \lesssim \log(L_{TIR}/L_{\odot}) \lesssim 13$). Le Floc'h et al. (2005) showed that

ULIRGs make up only ∼10% of the IR population at z ∼ 0.7, which roughly means, at the redshifts we are studying here, we should expect to see 4 to 12 ULIRGs. While the errors on this estimate are almost certainly large enough to encompass our two ULIRGs, it is still odd that our sample lies at the low end of the expected range. If galaxies in groups have higher propensities for mergers or low-velocity encounters, we might expect to see more of these high-L_{TIR} galaxies in the groups, if not overall. Geach et al. (2009) suggest that such encounters could be fueling the growth of galactic bulges, which explains the larger fraction of Sa through E galaxies in the groups. If we do not see massive amounts of star formation in the groups—or, in this case, neither the groups nor the field—then either a process common to both group and field galaxies is responsible for the bulge formation or star formation from mergers and low-velocity encounters is short enough to not show significant IR emission in individual galaxies.

Because mass has been shown to have significant association with suppressing star formation, we also made a quantitative test of the overall similarity of group and field members of similar mass. The ratio of low-activity star forming galaxies (i.e., those with SFR < 2.7 $M_\odot$ yr^{-1}) to the total number of galaxies with $M_* > 10^{10}$ $M_\odot$ is 0.69. We synthesized this result from field galaxies in a Monte Carlo calculation, drawing randomly from a field sample matched in mass. The synthesized distribution is Gaussian and has its maximum probability at a fraction of 0.66, with a range at $\pm 1\sigma$ from 0.62 to 0.70. That is, there is only marginal evidence (1σ) for a change in incidence of high levels of star formation in galaxies of the same mass in groups versus the field, and any such change is limited to be no more than a 10% effect (at 1σ).

All of these results are consistent with the hypothesis that the difference between the group and field populations is confined largely to their differing mass

functions. For a given mass and morphological type, there is no statistically significant suppression or enhancement of star formation in individual group galaxies in the intermediate stellar mass range of 10^{10} to 2×10^{11} $M_\odot$. However, groups have begun to build massive galaxies with lower specific star formation rates as typical for their relatively-early types. The shifts toward lower specific star formation rates and toward higher masses tend to cancel each other, leading to similar infrared fractional luminosity functions.

We must remind ourselves, however, that we are only probing the brightest star-forming galaxies at these redshifts; galaxies with SFRs below our detection limit could be more affected by the group environment, resulting in a lower fraction of star-forming galaxies in the groups (Peng et al., 2010). Locally, the fraction of IR-active galaxies in the two environments differs by $\sim$30% (more star-forming galaxies in the field) for galaxies with SFRs $\gtrsim 0.1$ $M_\odot$ yr^{-1}, a much lower detection limit than our sample (Bai et al., 2010). Other group studies have found environmental dependence of the fractions of star-forming group and field galaxies at fixed luminosity or stellar mass using different indicators (Wilman et al. 2005a, 2008; Balogh et al. 2007, 2009).

These differences suggest that groups are indeed an intermediate stage between the field and clusters. Our groups contain fractions of E and S0 galaxies at levels comparable to clusters (Wilman et al. 2009), and the mass distribution of group galaxies tends to extend higher than that of field galaxies, as confirmed with a more detailed inspection of the group and field galaxy masses. Despite these differences, the overall IR activity in groups seems to indicate a lack of suppression or enhancement of star formation as compared with the field: the fractions of star-forming galaxies (SFR > 2.7 $M_\odot$ yr^{-1}) are comparable in the groups and field, and the fractional luminosity functions are nearly identical. Individ-

ual galaxies of similar mass and morphology appear to have virtually identical infrared properties in the two environments. Thus, the group environment affects the masses and morphologies of galaxies, and their star forming properties change consistent with these effects. However, any additional changes in star forming properties are, at best, subtle, at least for SFR > 2.7 $M_\odot$ yr^{-1}, indicating that the level of star formation is driven primarily by galaxy mass, itself a function of environment. In other words, star-forming activity in individual galaxies is only indirectly related to the group versus field environment but is linked more strongly to the overall change in galaxy masses and morphologies (Peng et al., 2010). The higher L^* for the supergroup of Tran et al. (2009) may indicate an enhancement of star formation that is environmentally-dependent, but they find that mass more strongly affects star formation. Apparently, the assumed increased rate of galaxy-galaxy interactions in groups either does not affect the star formation significantly, or strong interaction-driven star formation occurs in environments other than the groups we studied here.

The outskirts of clusters are a probable alternative location for galaxy processing, as shown by the higher fractions of IR-bright galaxies in group and field galaxies than the outskirts of the Coma and A3266 clusters (Bai et al., 2009). Additional studies of groups and clusters at a variety of redshifts, preferably to lower SFR limits, are needed to further disentangle the effects of these moderately-dense environments on the star formation, mass, and morphology of their member galaxies.

3.5 Conclusions

We have observed 26 galaxy groups and accompanying field galaxies with deep MIPS photometry and used 24 μm flux densities to estimate the total IR lumi-

nosities and SFRs of galaxies in both environments. We find that on an individual basis, group and field galaxies of similar mass and morphology do not differ significantly in terms of their SFRs, and the amount of star formation does not depend on the richness of the groups. However, the groups have systematically lower specific SFRs and a higher incidence of massive early-type galaxies, more reminiscent of clusters than the field. We discovered that some of these E and S0 galaxies, as well as a large contingent of massive early spirals, are still forming stars at significant levels. These galaxies may explain why the fractional luminosity functions of the groups and field are nearly identical despite the overall decrease in star-forming activity in the groups. The group environment affects galaxy SFRs primarily through the shift toward higher masses, with an accompanying trend toward earlier types and reduced specific SFRs. These high-mass, early-type galaxies, along with IR luminosities comparable to the field, put groups in between the field and clusters in terms of overall galaxy properties.

CHAPTER 4

STAR-FORMING GALAXY EVOLUTION IN NEARBY RICH CLUSTERS

(Tyler et al. 2013, in prep)

Dense environments are known to quench star formation in galaxies, but it is still unknown what mechanism(s) are directly responsible. In this paper, we study the star formation of galaxies in Abell 2029 and Coma, combining indicators at 24 μm, Hα, and UV down to rates of 0.03 $M_\odot$ yr^{-1}. We show that A2029's star-forming galaxies follow the same mass–SFR relation as the field. The Coma cluster, on the other hand, has a population of galaxies with SFRs significantly lower than the field mass–SFR relation, indicative of galaxies in the process of being quenched. A significant fraction of these galaxies host AGNs. Ram-pressure stripping and starvation/strangulation are the most likely mechanisms for suppressing the star formation in these galaxies, but we are unable to disentangle which is dominating. The differences we see between the two clusters' populations of star-forming galaxies may be related to their accretion histories, with A2029 having accreted its star-forming galaxies more recently than Coma. Additionally, we discovered a sample of early-type galaxies in A2029 whose 24 μm and/or FUV emission does not appear to come from star formation. Similar galaxies have probably been classified as star-forming in previous studies of dense clusters, possibly obscuring some of the effects of the cluster environment on true star-forming galaxies.

4.1 Introduction

High-density regions have long been known to affect the evolution of galaxies, morphing blue, star-forming disks into red, quiescent early-types. Many possible methods by which dense regions change galaxies have been discussed: ram-pressure stripping, the removal of a galaxy's gas as it plunges through the intra-cluster medium (ICM) (e.g., Gunn & Gott 1972; Kinney et al. 2004; van Gorkom 2004; Sivanandam et al. 2010); starvation/strangulation, the removal of the hot gas halo by the ICM, making it unable to accrete more material (e.g., Larson et al. 1980; Balogh et al. 2000; Kawata & Mulchaey 2008; McCarthy et al. 2008); and galaxy-galaxy interactions, such as harassment and mergers, which readily change the morphologies of galaxies (e.g., Barnes & Hernquist 1996; Mihos 2004; Conselice 2006). See Boselli & Gavazzi (2006) for a more comprehensive review of these environmental processes.

What is not known, however, is which of these effects—if any—play dominant roles in the galaxy evolution seen in different environments. The effects are strongest in dense clusters, which tend to have higher fractions of early-type galaxies and lower fractions of star-forming galaxies than the field (e.g., Dressler 1980; Gómez et al. 2003; van der Wel et al. 2007; Bai et al. 2009; Tempel et al. 2011), suggesting they are instrumental in cutting off a galaxy's ability to form stars. This behavior becomes less prominent with youth: clusters at higher redshifts (up to $z \sim 1$) have both more star-forming galaxies in general and more massive star-forming galaxies than local clusters (Kennicutt 1983; Balogh et al. 1997; Hashimoto et al. 1998; Poggianti et al. 1999). Galaxy morphology and star formation also depend on local density (Dressler 1980; Whitmore et al. 1993; Lewis et al. 2002; Christlein & Zabludoff 2005; Petropoulou et al. 2011). In Coma, for example, the outer regions of the cluster have higher fractions of low-star-

forming galaxies than the dense center (Bai et al. 2009; Edwards & Fadda 2011).

It is also possible that at least some of the evolution we see in cluster galaxies occurs before they reach such high densities, though the evidence is less clear. Galaxy groups are known to have nearly cluster-level fractions of early-type galaxies, specifically S0s (Postman & Geller 1984; Zabludoff et al. 1996; Zabludoff & Mulchaey 1998; Wilman et al. 2009; Just et al. 2010). Also, groups have lower fractions of star-forming galaxies than the field but higher fractions than clusters (Wilman et al. 2005b; Gerke et al. 2007; Wilman et al. 2008; Balogh et al. 2009; Iovino et al. 2010). Both of these results would seem to indicate a sort of "pre-processing" occurring in groups, but because these and other recent studies (Tran et al. 2009; Bai et al. 2010; Tyler et al. 2011) show that groups appear to be intermediate between the field and clusters, additional processing must still occur in clusters.

There are many aspects of both star formation and clusters themselves we need to consider if we wish to understand the dominant mechanism for the quenching of star formation in dense regions. First, we must accurately estimate the star formation rate (SFR). Optical and UV data are frequently used; however, both are subject to uncertain corrections for dust absorption. UV measurements, specifically, can be subject to selection biases that tend to make them echo the overall luminosity function of the cluster (Cortese et al., 2008). The mid-infrared (mid-IR) does not have these problems, and its overall correlation with total IR luminosity (L_{TIR}) makes it a good indicator of the total SFR of most galaxies (Rieke et al., 2009). Still, the mid-IR probes only obscured star formation, which means it can underestimate the SFR in galaxies with low levels of star formation, where there is less dust and less extinction (Kennicutt et al. 2009; Rieke et al. 2009; Calzetti et al. 2010). Using only one type of star-formation indicator, therefore,

only tells us part of the story. To get an unbiased picture, we need to estimate the total amount of star formation in galaxies—obscured and unobscured—and probe down to the very lowest SFRs.

Additionally, we also need to study a cluster that is not in the process of forming or merging with other clusters or groups. Large numbers of infalling galaxies can obscure the overall effect of the dense environment on member galaxies. The higher fraction of star-forming galaxies in the field, as well as triggered star formation from galaxies falling into the cluster potential, can make cluster members appear more like field and/or group galaxies than what perhaps the cluster would be in a few gigayears (e.g., Beijersbergen et al. 2002; Cortese et al. 2008; Mahajan et al. 2010). If we want to focus on what effects dense environments have on galaxies, we need to observe stable, relaxed clusters.

Abell 2029 seems to be one such cluster. It appears relaxed, with a large brightest cluster galaxy (BCG) at the center, a smooth X-ray profile, and a lack of large substructures (Lewis et al. 2003; Vikhlinin et al. 2005; Bourdin & Mazzotta 2008). Deep MIPS 24 μm data are available from the Bai et al. (2007b) study of intracluster dust, probing IR luminosities down to low levels. Homogeneous optical spectra were obtained in this work, and there is a pointed GALEX observation of the cluster as well (Hicks et al. 2010), allowing us to combine Hα, IR, and UV measurements into a more complete picture of obscured and unobscured star formation in the cluster down to low SFRs. To place our work within a broader context, we compare it with similar results for the Coma cluster.

In Section 2, we discuss our observations and sample selection. Section 3 covers the creation and analysis of our SFR functions, Section 4 introduces a population of 24 μm-detected early-type galaxies which do not appear to be forming stars, and Section 5 discusses the analysis of A2029 with these early-type galaxies

removed. Section 6 compares A2029 with studies of the Coma cluster, and we discuss the two clusters in Section 7. Our conclusions are summarized in Section 8. Throughout the paper, we use the following cosmological parameters: $H_0 = 70$ km s^{-1} Mpc^{-1}, $\Omega_M = 0.25$, $\Omega_\Lambda = 0.75$.

4.2 Sample & Data Reduction

4.2.1 Infrared Observations

Cluster A2029 was originally observed with the Multiband Imaging Photometer for *Spitzer* (MIPS; Rieke et al. 2004) in February 2004 with a total integration time of 80 s pixel^{-1}. Additional observations in January 2005 to look for faint intracluster emission extended the exposure time to $\sim$340 s pixel^{-1} for the combined mosaic over a $\sim 45' \times \sim 80'$ area (Bai et al., 2007b). The images were processed using the MIPS Data Analysis Tool (DAT, ver. 2.9; Gordon et al. 2005) as described by Bai et al. (2007b).

Sources were initially selected using the IRAF routine DAOPHOT (Stetson, 1987) and fluxes from PSF fitting. Errors were estimated for each source by averaging the sigma-clipped flux of the nearest 30 randomly-placed apertures. True detections were selected in terms of these errors: sources at 3σ or above were considered real sources, while anything below 3σ significance was rejected. All possible sources were visually inspected so as not to include false detections such as high-signal image artifacts.

The DAOPHOT routine occasionally missed faint sources in the field, so we also used SExtractor to identify and extract IR sources. This routine first subtracts the background and filters with a Gaussian function with a 4″ FWHM. The program also used a deblending routine to separate individual sources and remove any artifacts that may masquerade as sources. We used a 1σ detection thresh-

old to identify and extract all possible sources, though only those above 3σ were retained as true detections. (This is the same method used to remove sources in Bai et al. (2007b); see their paper for additional information on source extraction.) The SExtractor routine was able to identify more low-flux sources than DAOPHOT, though after filtering out AGNs and other sources (discussed later), few new galaxies were added. Given the better accuracy of this method, we use the SExtractor-selected galaxies in the rest of this paper. The differences between these two methods are minor, however, and our overall results are independent of the photometry approach.

As a result, the 3σ detection limit was $\sim$135 μJy, or $L_{24} \sim 2.6 \times 10^{41}$ erg s^{-1} and SFR $\sim$ 0.028 $M_\odot$ yr^{-1} using the method of Calzetti et al. (2010) at the redshift of our cluster (z $\sim$ 0.08).

4.2.1.1 IR Source Matching & Errors

To identify which optical sources had 24 μm emission, we cross-correlated optical and IR catalogues by matching the position of each to within a radius of 3″ (corresponding to $\sim$4.5 kpc). The matching radius needed to be small enough to minimize the number of false matches while simultaneously including galaxies with star formation in their outer regions, since areas of star formation can be clumpy and/or asymmetrical with respect to the overall shape of the galaxy, especially in late-types. Although positions at 24 μm are accurate to $\lesssim$ 1″, the MIPS PSF is large (6″ FWHM). Our field is relatively crowded, and some of our IR sources are extended, leading to our selection of this matching radius.

Incorrectly-matched IR sources will occur, however, so it is important to be aware of the errors of our source-matching criteria. First, we noted four IR sources had been matched to multiple optical galaxies. After viewing optical images of the area, all were easily associated with a specific galaxy and the incorrect opti-

cal matches removed. This gives us a rough estimate of our IR/optical source-matching errors of ∼0.8% incorrectly matched sources.

Given that we can detect sources far beyond our cluster redshift and that we would like to have an upper limit on the possible fraction of incorrect matches, we scattered ∼3,500 fake source coordinates randomly over the 24 μm image. (This is slightly more fake sources than the number of real sources detected in the 24 μm image but still below the confusion limit.) We combined the real 24 μm source list with this fake source list and matched it to our catalog of cluster and field galaxies with known redshifts. The fraction of galaxies matched to a fake source was much less than 1%. We conclude that the total fraction of 24 μm sources matched to an incorrect optical source is no more than ∼1%.

4.2.2 Optical Observations

To confirm cluster members spectroscopically, we targeted 1800 objects in the inner $30' \times 60'$ of the MIPS field with the Hectospec fiber spectrograph on the MMT at Mt. Hopkins (Fabricant et al., 2005). We used the 270 gpm grating, covering a wavelength range of 3650–9200 Å for objects down to r $\sim$ 20, allowing us to observe the Hα emission line in galaxies out to z $\sim$ 0.4, far beyond the cluster redshift. The region was observed using two different configurations with three 10-minute exposures each for the brightest galaxies and five different configurations with three 15-minute exposures each for all other sources. The spectra were reduced using the HSRED[1] IDL routine. We visually confirmed the redshift of each source using best-fitting templates, resulting in confident redshifts for 1352 objects.

Because 24 μm emission from AGNs can masquerade as star formation, we need to identify possible active galaxies from our sample. HSRED and our redshift-

[1]See http://www.astro.princeton.edu/∼rcool/hsred/ or http://code.google.com/p/hsred/.

confirmation widget identify AGNs and QSOs via emission line ratios, allowing us to confirm their active galaxy status by eye and remove them. To be as conservative as possible, we also removed a few additional galaxies that did not have sufficient line ratios but still appeared to have suspiciously AGN-like spectra (e.g., broad hydrogen lines).

4.2.3 UV Observations

We selected far-UV (FUV) sources in the GALEX database[2] from the A2029 pointed observation GI3-103 (PI: Hicks) described in further detail in Hicks et al. (2010). The GALEX 1.2-degree field of view, centered on the BCG, includes our entire Hectospec coverage area so that none of our spectroscopically-confirmed cluster members lie near the edge of the GALEX image. This 1517-second observation is $\sim$85% complete down to $\sim$23.0 mag. Because this completeness limit is for 5σ or brighter sources, our SFR(FUV) detection limit (0.043 $M_\odot$ yr^{-1}) is a conservative estimation[3]. We then matched the UV sources with our optical catalog using a $4''$ radius.

4.2.4 Sample Selection

To differentiate cluster members from the field, we used the method of den Hartog & Katgert (1996), who select members based on each galaxy's relative line-of-sight velocity (V-V0, where V0 is the mean cluster velocity) as compared with its projected distance from the center of the cluster. Den Hartog & Katgert (1996) then use the maximum line-of-sight velocity at a given distance from the cluster center to define which galaxies are cluster members and which are interlopers. Figure 4.1 shows this method for A2029. The maximum line-of-sight velocity is

[2]http://galex.stsci.edu/GR6/.

[3]See the GALEX website and the GALEX exposure time calculator (http://sherpa.caltech.edu/gips/tools/expcalc.html) for additional information.

plotted as a pair of dashed lines. Only galaxies within these lines are considered cluster members. To ensure we were as complete as possible, we retrieved all extended sources near the cluster redshift within our 24 μm field of view from the NASA/IPAC Extragalactic Database[4] (NED) and the Sloan Digital Sky Survey[5] (SDSS). We removed duplicate sources and included the remaining galaxies for identifying cluster members.

After removing all non-cluster galaxies and limiting the field sample to galaxies with $z \leq 0.2$, we have a total of 588 cluster galaxies (445 of which were covered by Hectospec and MIPS) and 65 field galaxies with redshifts. All the cluster members are listed in Table 1. We did not include any of the NED or SDSS sources in our final sample because it is difficult to identify and correct for selection biases of these galaxies.

[4]The NASA/IPAC Extragalactic Database is operated by the Jet Propulsion Laboratory, California Institute of Technology, under contract with the National Aeronautics and Space Administration.

[5]http://www.sdss3.org/

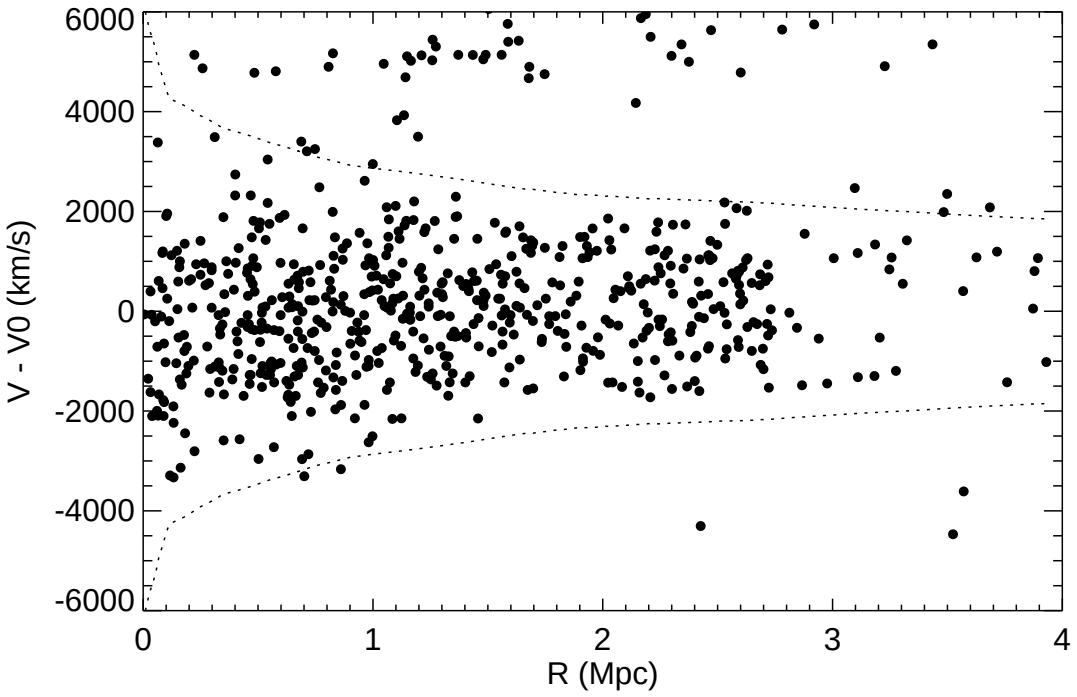

Figure 4.1 Relative velocity (V) of all galaxies with respect to the cluster mean velocity (V0) as a function of projected distance from the cluster center. Cluster members were selected to be galaxies within the maximum line-of-sight velocity (dotted lines) at a given distance, as per den Hartog & Katgert (1996).

Table 4.1. A2029 Member List

RA	Dec	z	$\log(L_{24\mu m})$ ($L_\odot$)	$\log(L_{H\alpha})$ ($L_\odot$)	$\log(L_{FUV})$ ($L_\odot$)	SFR (min)[a] ($M_\odot$ yr^{-1})	SFR (max)[a] ($M_\odot$ yr^{-1})	$\log(M_*)$ ($M_\odot$)	Notes[b]
227.59595	5.6415414	0.0768	-	-	-	-	-	10.34	-
227.46886	5.6797333	0.0808	-	-	-	-	-	10.87	-
227.58581	5.8550225	0.0812	8.44	7.46	8.61	0.711	0.711	10.29	-
227.32547	5.5163308	0.0793	9.38	7.49	8.54	2.185	2.185	10.90	-
227.34391	5.5039944	0.0752	8.47	6.75	-	0.242	0.242	10.22	-
227.38376	5.5582892	0.0731	9.07	7.06	8.16	1.007	1.007	10.18	-
227.35787	5.5324111	0.0739	8.06	6.35	-	0.094	0.094	9.94	-
227.41070	5.6222886	0.0799	-	-	-	-	-	10.34	-
227.54800	5.4776306	0.0786	9.23	-	-	1.109	1.109	10.57	2
227.44500	5.6604972	0.0835	9.20	7.51	8.85	1.713	1.713	10.31	-
227.43088	5.6700219	0.0838	9.44	7.74	9.16	2.928	2.928	10.74	-
227.53186	5.6630389	0.0842	8.75	7.66	9.61	1.176	1.176	9.59	-

4.3 SFR Function

4.3.1 Methodology

For all sources detected at 24 μm, we calculated the 24 μm luminosity (L_{24}) with the general relation between flux and luminosity (νF_ν) using the luminosity distance. Hα luminosities ($L_{H\alpha}$) were calculated using the Hα equivalent width along with the continuum magnitude, which was estimated by linearly interpolating between the SDSS r- and i-band magnitudes to the Hα rest-frame wavelength. The linear behavior of the SEDs of these galaxies at SDSS r, i, and z (and sometimes g) makes linear interpolation appropriate in this case. For the few sources without SDSS observations, we simply use the r-band magnitude, which is not significantly different from the interpolated magnitude for most sources. Additionally, because our field galaxy sample only contains objects out to z $\sim$ 0.2, this method can be used for all field galaxies as well since Hα does not redshift beyond the i-band until z $\sim$ 0.4. The equivalent widths were calculated by linearly fitting the continuum within 200 Å of the emission line and fitting a Gaussian to the Hα line on top of the continuum fit. All fits were visually checked; those where the continuum and/or Hα line were fit poorly by our automated routine were then fit manually (using the same method) so as to make the measurements as accurate as possible. The errors of these manually-fit lines were modified to reflect the higher uncertainty in the fits.

We use the equations of Calzetti et al. (2010) to convert 24 μm and/or Hα luminosities to total SFRs. As required by Calzetti et al. (2010), galaxies with both 24 μm and Hα measurements used unobscured (uncorrected) $L_{H\alpha}$. For sources with only Hα detections and no 24 μm, we had two options: for a lower-limit on the SFR (unobscured), we used the same conversion but without the IR contribution; as an upper limit, we added in our 24 μm detection limit for the IR component.

Table 4.1—Continued

RA	Dec	z	$\log(L_{24\mu m})$ ($L_\odot$)	$\log(L_{H\alpha})$ ($L_\odot$)	$\log(L_{FUV})$ ($L_\odot$)	SFR (min)[a] ($M_\odot$ yr^{-1})	SFR (max)[a] ($M_\odot$ yr^{-1})	$\log(M_*)$ ($M_\odot$)	Notes[b]
227.54318	5.5711417	0.0765	8.23	-	8.47	0.235	0.235	11.31	2
227.49977	5.6787333	0.0732	-	-	-	-	-	10.94	-
227.57229	5.7011861	0.0782	-	-	8.57	0.064	0.138	11.00	2

[a]If a galaxy only has Hα or FUV detections (no 24 μm), then the lower limit (min) on SFR is calculated using these wavelengths without dust corrections. The upper limit (max) is calculated using our 24 μm detection limit with Hα (or FUV if Hα is not available). If the min and max values of SFR are the same, then the SFR was calculated using 24μm and Hα (or FUV if Hα is not available). In these cases, the total SFR includes both obscured and unobscured components from measured quantities.

[b]Notes: (0) indicates galaxies without 24 μm data; (1) indicates galaxies from SDSS or NED that are cluster members but do not have Hectospec coverage; (2) indicates passive (non-star-forming) galaxies (the SFRs listed in the table are from assuming the 24 μm and/or FUV detections were due to star formation); (3) indicates galaxies spectroscopically identified as AGN and not included as star-forming galaxies (as with the passive galaxies, the SFRs listed in the table are calculated as if the 24 μm, Hα, and/or FUV were all from star formation only).

Note. — This is only a small sampling of the full catalog, which is available in electronic format.

We originally assumed that the very low SFRs of the Hα-only detected sources indicated that the obscuration of these systems was insignificant. However, if we include the 24 μm upper limits, only about half of the SFRs of these galaxies remain reasonably unaffected; the other half change more significantly, indicating there could be a significant obscured component for some sources. Despite this, we chose to display the non-corrected Hα SFRs in our figures unless stated otherwise; using the upper limits does not change our conclusions.

It is more difficult to detect weak Hα emission lines in a bright galaxy than a faint one due to the higher continuum level of the bright galaxy. Therefore, we estimated our Hα detection limit using the Hα luminosities of the brightest galaxies in the r-band and converting them to SFRs using the methods already discussed. All but a few of the Hα-detected galaxies are above this limit (0.06 $M_\odot$ yr^{-1}), and 80% of all galaxies in the cluster are fainter in the r-band than the galaxies used to calculate the detection limit, giving us an estimate of the completeness limit of our Hα-detected galaxies as well.

In a similar manner, we calculated UV SFRs by correcting the FUV (1350–1780 Å) luminosity for obscuration effects using the 24 μm luminosity (for sources with both UV and IR detections) from Zhu et al. (2008). Then we used the method of Kennicutt et al. (2009) to convert this FUV luminosity to SFR. We double-checked our conversions by comparing the combined 24 μm/Hα SFR with the 24 μm/FUV SFRs, which agreed very well and with minimal scatter. For galaxies only detected in the FUV (not 24 μm or Hα), as with Hα-only detected objects, we use the same conversion to SFR but without the 24 μm component for a lower limit on the SFR. If we compare our unobscured Hα SFR with the unobscured FUV SFR (for objects with detections in both), the scatter is larger, though the Hα SFRs tend to be higher than the FUV SFRs. As with the Hα measurements, if we

correct the UV-only SFRs with our 24 μm detection limit (resulting in an upper limit on the SFR), our conclusions do not change.

Our SFR functions are corrected for spectroscopic completeness, which was calculated by taking the number of sources with spectroscopic redshifts in a given r-band bin and dividing it by the total number of photometrically-identified extended sources in each bin. The reciprocal of these values is the correction factor. We interpolated between these values given each source's r-band magnitude. The 24 μm detections are already 80% complete at the IR detection limit, and the vast majority of our 24 μm detections are far above this limit, so we do not correct for the incompleteness of IR source detections.

K-corrections and stellar masses were estimated using the KCORRECT (v. 4.2) routine SDSS_KCORRECT, which calculates mass using template and model fits with SDSS photometric data (see Blanton et al. 2007 for details). KCORRECT uses a different IMF and cosmological values than we use, so we corrected the original stellar mass output to the IMF and cosmology adopted in this paper.

4.3.2 Initial Cluster SFR Function

We created an initial SFR function by plotting all cluster galaxies in terms of their detection method (Figure 4.2). (Initially, we focused on 24 μm and Hα only; the UV detections will be discussed in the following section.) Galaxies only detected at 24 μm or Hα are indicated by brown open triangles or blue open stars, respectively, with detection limits shown by the brown dashed line and blue dot-dashed line. The green open circles indicate sources detected at both Hα and 24 μm, while the black filled circles are all sources, regardless of detection method, with Poisson errors. (Lines connecting the data points are used only to help guide the eye.) Two things stand out: the population of 24 μm-emitting galaxies without Hα emission and the apparent turnover at log(SFR) $<$ -0.8. For now, we focus on

the first of these phenomena.

4.4 Passive Early-Type Galaxies

Star-forming galaxies detected in the IR but with no appreciable Hα emission might be expected at higher SFRs: increasing SFRs are associated with increasing amounts of obscuring dust. Indeed, it might seem strange that the galaxies at the highest SFRs have both 24 μm and Hα detections. However, the SFRs of the most active galaxies in this cluster do not reach even $\sim$10 $M_\odot$ yr^{-1}, which apparently is not associated with enough dust to completely obscure the Hα emission. So if our most vigorously star-forming galaxies are detected at both 24 μm and Hα, why do we have a population of low-star-forming galaxies only detected in the IR? Objects forming stars at such rates should have observable Hα emission; there should not be enough dust to completely obscure the Hα line. We now take a closer look at these IR-emitting galaxies.

4.4.1 The Passive UV- and IR-Emitting Galaxy Population

Figure 4.3 shows the typical optical spectra (redshift-corrected) of the 41 24μm-only galaxies, with the Hα wavelength identified by a vertical dashed line. All of the galaxies (even the ones not shown here) appear to be early-types. Other than the sky absorption lines, the only obvious features are the Hβ and Ca H and K absorption lines; a few of the spectra shown have [N II]6583$\AA$ emission lines. They do not look like star-forming galaxies at all.

However, the Hectospec fibers subtend 1.5″ on the sky, which means for the larger galaxies, we may only be probing the central bulges and missing star formation in the outer regions of the galaxies. If we look at optical images of this population from SDSS (both cluster and field galaxies; Figure 4.4), we see that nearly all have early-type morphologies (E/S0). Some could be edge-on spiral

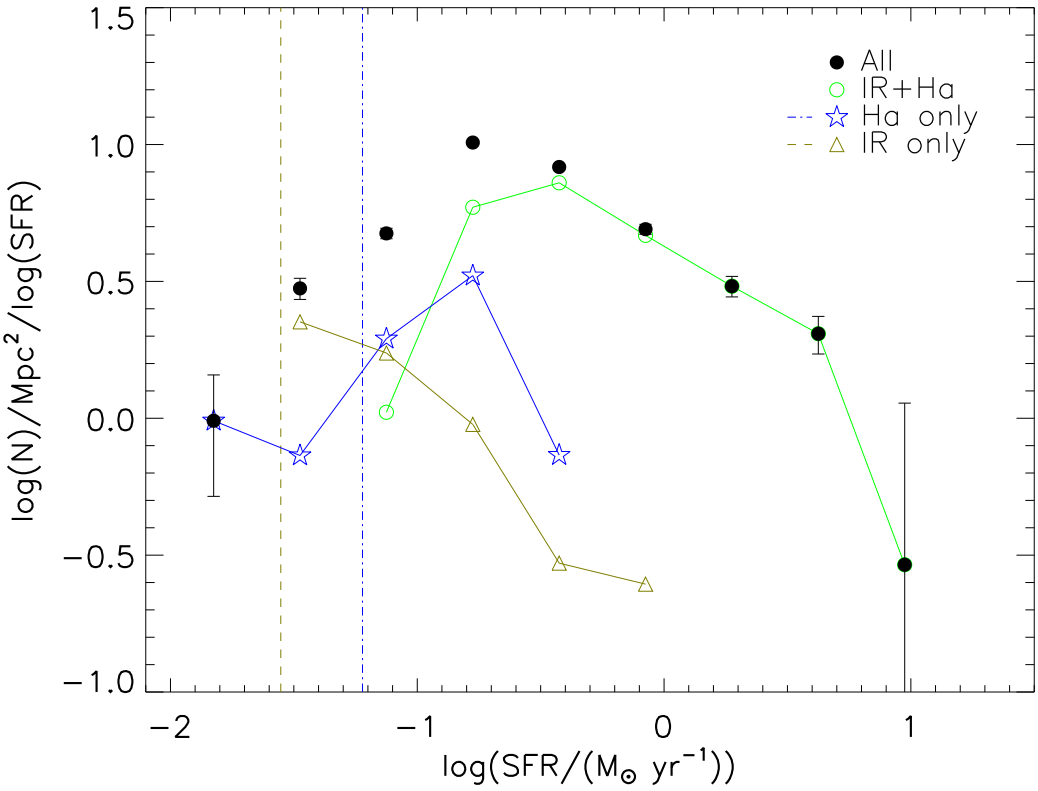

Figure 4.2 SFR function of A2029 broken down into star-formation detection methods: galaxies only detected in Hα (blue open stars), galaxies only detected at 24 μm (brown open triangles), galaxies detected with both IR and Hα (green open circles), and all galaxies combined (black filled circles). (Lines connecting the points are for guiding the eye only.) The brown dashed line and blue dot-dashed blue line indicate our approximate 24 μm and Hα detection limits, respectively.

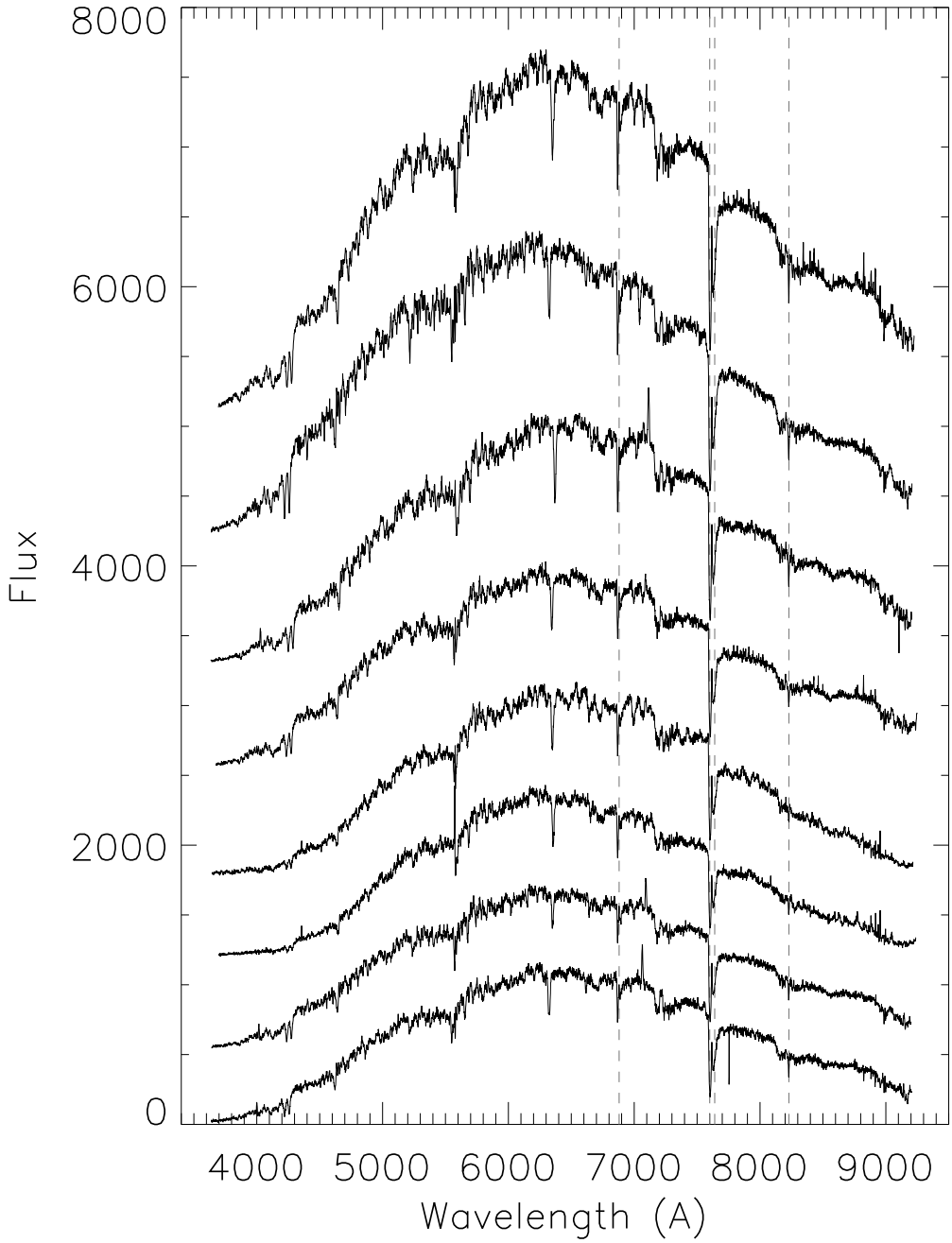

Figure 4.3 MMT Hectospec optical spectra of a portion of the 24 μm- and/or FUV-detected galaxies without Hα emission. Grey dashed lines indicate sky absorption features. None of these sources show any star formation or obvious AGN activity that could account for the 24 μm emission.

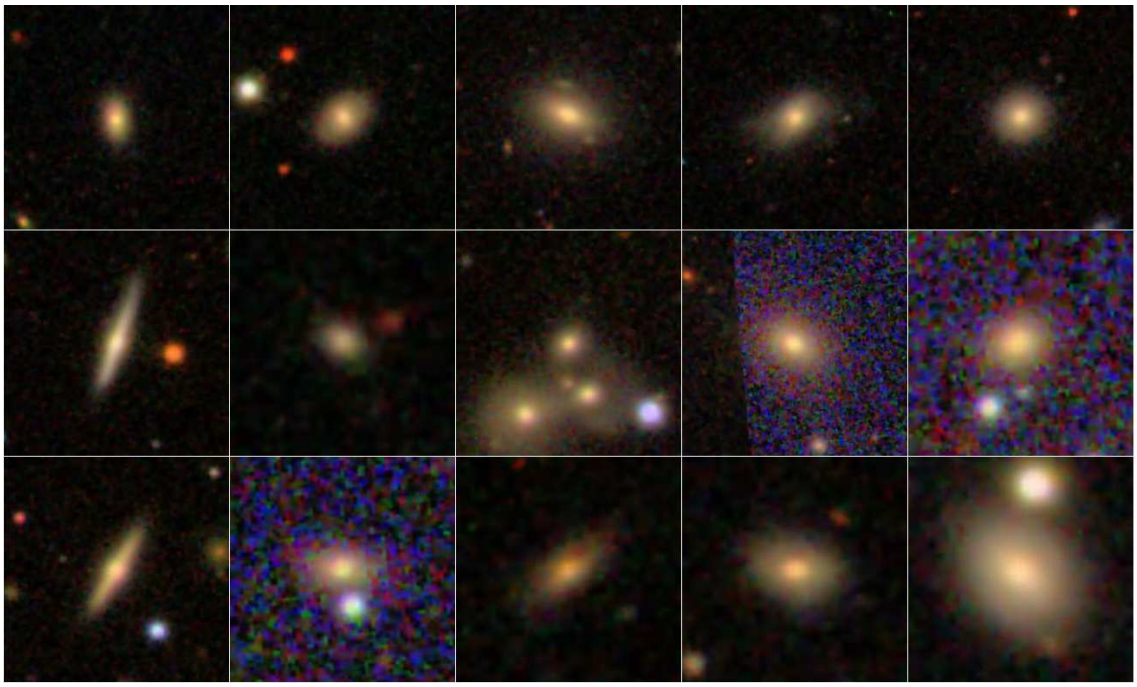

Figure 4.4 SDSS multi-color images of the 24 μm-/FUV-detected-only galaxies whose spectra are shown in the previous figures (not to scale). Most of the sources look like early-type E or S0 galaxies or passive early-type spirals.

galaxies, but given their red colors and the lack of any indications of star formation in their spectra, they seem to be completely passive. Only a handful show blue colors and other morphological features indicative of ongoing star formation. A closer look at the IR images of these galaxies revealed some with 24 μm emission from the outer regions of the galaxies as well as the central bulges. The sizes of the bulges of these galaxies, however, are larger than the Hectospec fiber size, which explains why their spectra look like the rest of the early-type galaxies. These obviously star-forming galaxies were removed from the non-star-forming E/S0 population and retained in the SFR function.

One possibility for this 24 μm emission from early-type galaxies is that the

IR source is offset from the galaxies enough to cast doubt in terms of the 24 μm matching. Perhaps the IR emission is not from these galaxies but from other nearby sources. We investigated this possibility by comparing the location of the 24 μm sources to these early-type galaxies. All agreed in position almost exactly with their optical source. There were no accompanying optical sources for any galaxies that could be alternative identifications for the IR emission instead of the cluster members.

Twenty-four of the 41 24μm-detected early-type cluster galaxies were also detected in the FUV, and an additional 14 galaxies were detected only in the FUV and not in 24μm or Hα. Of all 55 galaxies not detected in Hα (but detected in 24μm or FUV), 38 have colors, morphologies, and spectra reminiscent of early-type, "red and dead" non-star-forming galaxies. Because of these similarities and the lack of any additional indicators of star formation, we treat these 38 as non-star-forming early-type galaxies (referred to as passive galaxies from here on) and identify the other 17 as star-forming. Of the rest, there are a total of 11 galaxies detected only at 24μm, 10 only detected in the FUV, and 17 detected in both that have no evidence of current star formation. This seems to indicate that the IR and/or UV emission is coming from a source other than young stars. Passive galaxies with IR/UV emission and excess have also been found in galaxies of other clusters (Boselli et al. 2005; Bressan et al. 2006; Ko et al. 2009; Shim et al. 2011).

4.4.2 Identifying the E/S0 IR Emission Source

If star formation is not causing the 24 μm or UV emission in these early-type galaxies, what is? One of the possible sources of the IR emission is dust around old stars. During the asymptotic giant branch (AGB) phase of stellar evolution, the stars lose mass via stellar winds, creating a shell of dusty material around

them that absorbs radiation from the star and re-emits it in the IR (Habing 1996; Piovan et al. 2003). In early-type galaxies, this population of stars is significant enough that their emission needs to be taken into account when modeling the SEDs (Bressan et al. 1998; Piovan et al. 2003).

Temi et al. (2009) use K_S-band luminosity compared with IR luminosity to identify both passive and star-forming early-type galaxies in the local universe. Figure 4.5 is our re-creation of the first plot of their Figure 1. We matched our cluster galaxies with those from the 2MASS extended and point source catalogs and plotted them as black squares (passive galaxies) and grey squares (all other cluster members). The dashed line is our 24μm detection limit at the redshift of the cluster. Temi et al. (2009) split their sample into blue (U-V $<$ 1.1; blue circles) and red (U-V $>$ 1.1; red circles) early-types. Green circles indicate galaxies without available U and/or V colors, and green triangles indicate 24μm upper limits. Temi et al. (2009) found a strong relation between L_{K_S} and L_{24} for red early-type galaxies with no apparent star formation (i.e., 24μm emission is from old stars and not star formation or AGNs; black line). Our own passive early-types mostly fall on or very close to the relation, indicating the IR emission in these galaxies is dominated by the old stellar population rather than AGNs or ongoing star formation. If we convert our SDSS data to UBVRI colors (using KCORRECT; Blanton & Roweis 2007), our galaxies would easily fall in the Temi "red" galaxy sample; indeed, most are much higher than the Temi et al. (2009) U-V limit. A few of our "passive" galaxies lie significantly above the truly passive relation, but like the rest of our passive sample, they appear to be normal early-type galaxies with no emission lines (though, a couple have weak [N II]6583$\AA$). The two early-type galaxies with the highest offset from the passive relation (also the least massive) do have blue colors (U-V ¡ 1.1), but this could be due to AGN. Since the nature of

the 24 μm emission in these galaxies remains unknown, they remain in the "passive early-type" list. Even if they were truly star-forming galaxies, however, they would not affect our results.

Though the IR emission from the passive A2029 galaxies seems to be from dust around old stars, weak AGNs could also be contributing. We removed the obvious AGNs from our sample already, but we could have missed low-luminosity AGNs. Inspection of our optical spectra reveals what could be faint [OIII]5007 Å emission lines in some of our IR early-types, but this is hardly conclusive. Most of these galaxies are also detected in the FUV, which could be coming from AGNs (e.g., Agüeros et al. 2005), though it could also be coming from recently-quenched star formation (e.g., Greggio & Renzini 1990; Yi et al. 2005; Donas et al. 2007; Atlee et al. 2009; Choi et al. 2009).

Instead, we can turn to X-ray observations of the cluster. Deep *Chandra* and *XMM-Newton* images from the central region of the cluster cover 28 of the 38 24 μm/FUV early-type galaxies we previously identified as not forming stars. Five are clearly detected in X-rays, implying that AGNs are likely responsible for the 24 μm/FUV emission in at least some cases. It is also possible that some have low-luminosity AGN that are too faint in X-rays to be detected in these observations, especially those from *XMM*, which is not as sensitive as *Chandra*. Additionally, the galaxies closest to the cluster center may not be detected due to their proximity to the bright X-ray gas of the cluster itself.

In conclusion, there are a variety of non-star-forming mechanisms that can produce low levels of IR and/or FUV emission in early-type galaxies. Generically, it appears that extremely low or nonexistent levels of star formation allow other IR and FUV sources that are usually hidden to dominate. No matter what the actual mechanism for the 24 μm and UV emission in these passive early-type

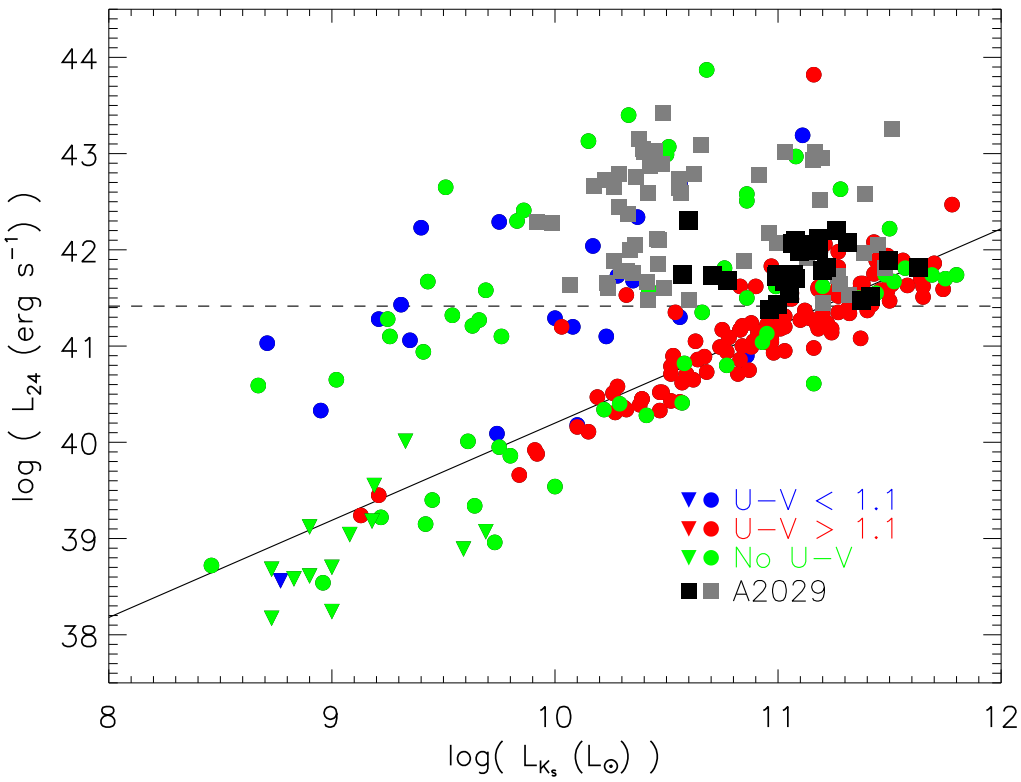

Figure 4.5 24 μm luminosity vs. K_S luminosity for the IR-detected, passive early-types in A2029 (black squares) and other cluster galaxies (grey squares). Our 24 μm detection limit is shown by the dashed line. All other points are from the Temi et al. (2009) sample of nearby early-type galaxies, including those with the following optical colors: U-V $>$ 1.1 (blue circles), U-V $<$ 1.1 (red circles), no U-V color data (green points), and 24 μm upper limits (triangles). Temi et al. (2009) found a strong trend (solid black line) with red early-type galaxies whose IR emission is dominated by the old stellar population as opposed to an AGN or any other source of 24 μm emission. Most of our passive cluster galaxies fall on or near this trend; similarly, their optical U-V colors are all well above the 1.1 limit. This suggests that the IR emission from the passive early-type galaxies is likely to be dominated by dust around old stars.

galaxies, it is highly unlikely to be from ongoing star formation. Thirty-eight of the 158 galaxies detected using at least one of the three star-formation indicators do not appear to be actively forming stars. This is 24% of the detected galaxies—not an insignificant fraction! This means that for SFRs $\lesssim 1$ $M_\odot$ yr^{-1}, one must be careful when using only a single indicator (UV or IR) for identifying star-forming galaxies.

4.5 Star-Forming A2029 Galaxies

4.5.1 Revised SFR Function

Figure 4.6 shows the "cleaned" SFR function with the non-star-forming early-type galaxies removed, using the same symbols as in Figure 4.2 but with FUV-detected star-forming galaxies included as purple open squares (FUV-only) and red down-pointing triangles (FUV- and 24 μm-detected). (The dotted purple line is the approximate FUV detection limit.) Removing most of the sources only detected at 24 μm or UV emphasizes the turnover at log(SFR) $\lesssim$ -0.8. Initially, we suspected we were simply missing Hα-emitting galaxies, but the FUV suggests the bin at log(SFR) $\sim$ -0.8 is complete.

We have found that the turnover is due to a selection effect. For our spectroscopy, we only targeted galaxies with r $\leq$ 20 mag, which will automatically filter out low-mass galaxies. This effect can be seen in Figure 4.7, where we compare the stellar masses of the galaxies with their total SFRs (IR, Hα, and/or FUV). A2029 galaxies are shown as red circles and field galaxies are shown as blue stars. (The non-star-forming early-type galaxies are shown as filled points; their SFRs are plotted as if the 24 μm and/or FUV emission was due entirely to star formation.) Galaxies with no detected star-formation indicator are plotted as downward arrows, indicating these points are upper limits (based on our 24

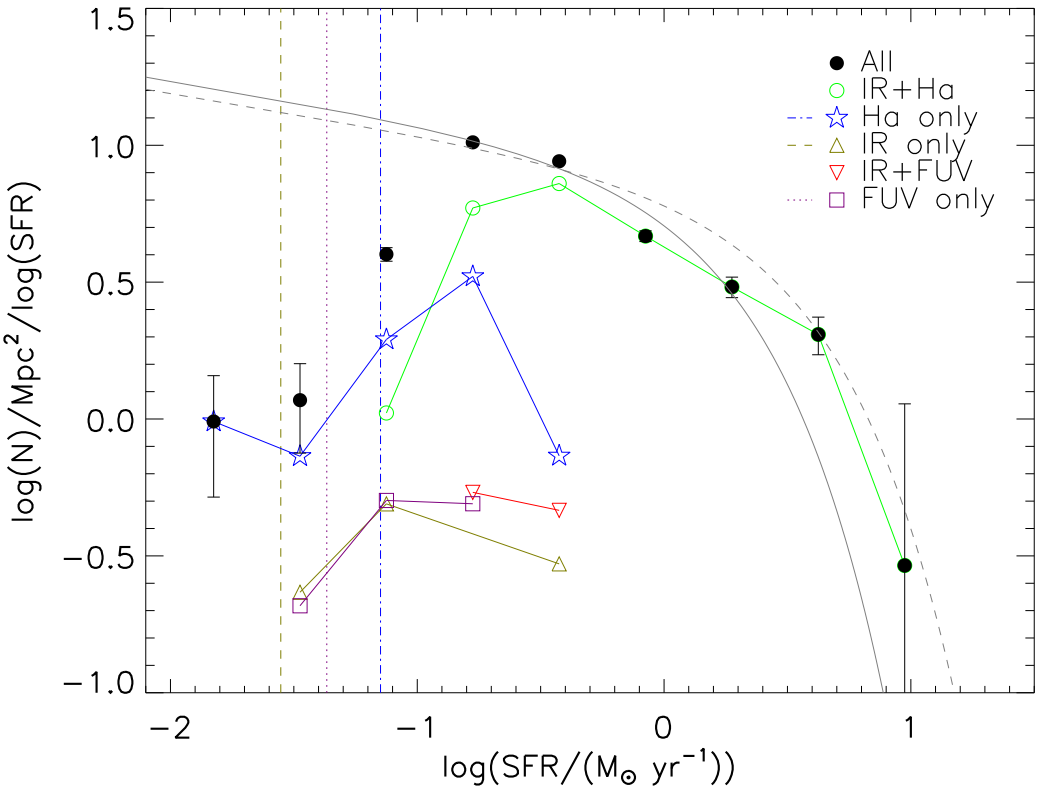

Figure 4.6 Revised SFR function with the non-star-forming early-type galaxies removed. We believe the sharp dropoff of galaxies at low SFRs to be the result of a selection bias. The same symbols are used here as in Figure 4.2 with additional FUV-only galaxies shown as purple open squares and FUV/24 μm galaxies as down-pointing red triangles. The approximate FUV detection limit plotted is as a vertical purple dotted line. The grey dashed line is the multi-cluster composite Schechter function from Bai et al. (2009) normalized to A2029 using χ^2 minimization. The solid grey line is the best-fit Schechter function using the same multi-cluster faint-end slope and allowing SFR* to vary. Both fits are comparable given the error bars and both fit A2029 reasonably well.

μm detection limit). If we look at all of the quiescent galaxies, we seem to be complete only down to log(M_*) $\sim$ 9.7. Some of the galaxies are lost due to the r-band magnitude limit, but many could be due to an inability to identify redshifts. It is difficult to determine the redshifts of quiescent galaxies because of their lack of emission lines; this is even harder for faint galaxies. Star-forming galaxies, on the other hand, have bright emission lines, making it much easier to measure their redshifts (as can be seen in the figure). We estimate for r $\sim$ 19.5 mag star-forming galaxies, we are complete in mass down to at least log(M_*) $\sim$ 9.0, if not lower. However, the greater difficulty in measuring redshifts accounts for the higher mass completeness limit for quiescent galaxies. Given what we know of our completeness in the star formation indicators, we estimate that our SFR function is complete down to log(SFR) $\sim$ -1.0 (Figure 4.6).

4.5.2 Comparison with Stellar Mass

Let us look more closely at Figure 4.7. Recall that red circles are galaxies in the cluster and blue stars are field galaxies (note that our field sample is incomplete). Open symbols connected by lines indicate galaxies with FUV or Hα detections but no 24 μm detections. The lower and upper limits in SFR for these sources are indicated by the unobscured SFR (FUV or Hα only) and maximum SFR (FUV or Hα corrected with the 24 μm detection limit), respectively. Overall, the star-forming galaxies in the cluster and field are comparable except for the highest masses. The quenching process is primarily responsible for a larger proportion of quiescent galaxies in the cluster, not a change in the mass–SFR relation for the active galaxies. We discuss this behavior quantitatively in Section 6.2.

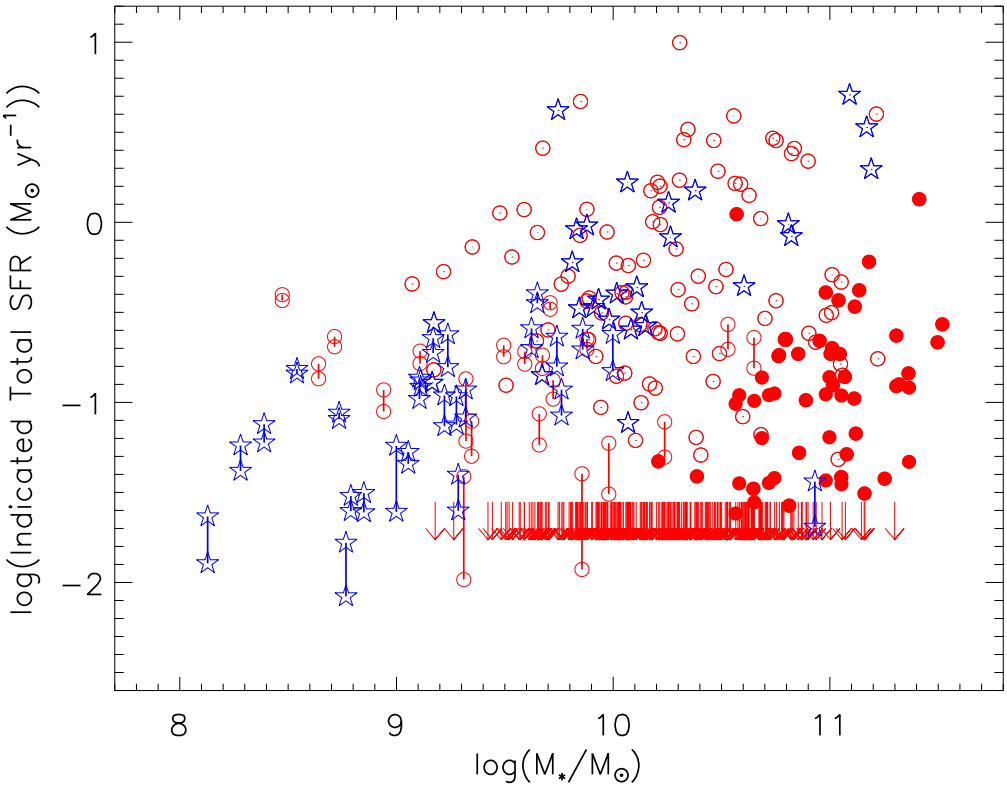

Figure 4.7 SFR vs. stellar mass (M_*) for A2029 (red circles) and the field (blue stars). Connected points indicate galaxies with SFRs calculated from uncorrected Hα/FUV only (lower limits) and uncorrected Hα/FUV combined with our 24 μm detection limit (upper limits). Red arrows indicate the upper limit of star formation for quiescent galaxies (i.e., the 3σ IR detection limit). Our population of IR-detected early-type galaxies is shown as solid points, with SFRs calculated as if the 24 μm emission was entirely from star formation. Without these massive non-star forming galaxies, the cluster is highly reminiscent of the field and most star-forming galaxies have SFRs high above the upper limit for quiescent galaxies, suggesting a rapid quenching mechanism is responsible for suppressing star formation in the cluster. Our mass limit for star-forming galaxies is estimated to be $\log(M_*/M_\odot) \sim 9$, while the limit for non-star-forming galaxies is closer to 9.7.

4.5.3 Galaxy Distribution

The location of star-forming galaxies in the cluster itself is an additional indicator of the suppression of star formation. Figure 4.8 is a histogram of the projected radius (in Mpc) of all galaxies in A2029 (black open bins), all star-forming galaxies regardless of detection method (blue hashed bins), and the non-star-forming IR/FUV early-type galaxies (red hashed bins). The star-forming galaxies appear to be somewhat evenly distributed, though a slight increase with increasing distance is evident. There is a faint opposite trend with the early-type galaxies. These trends could be biased by projection effects, however. To test this, we fit the overall galaxy distribution with a Navarro, Frenk, and White profile (NFW; Navarro et al. 1996) and created fake clusters with $\sim$500 galaxies randomly arranged in three-dimensional space according to the distribution. We then took the same fraction of star-forming galaxies as in A2029, placed them throughout the cluster, and created histograms of their projected radius. We ran this simple simulation hundreds of times and averaged the results. First, we distributed star-forming galaxy population uniformly throughout the cluster, resulting in these galaxies having a similar (NFW) profile to the overall cluster population. Then, we distributed the same population uniformly beyond 1 Mpc from the center. This resulted in a relatively constant projected radial distribution, indicating the central region of the cluster is mostly devoid of star-forming galaxies. The lack of star-forming galaxies in the dense core of the cluster, as well as the increasing fraction of star-forming galaxies with projected radius, suggests the suppression mechanism becomes more efficient as the local density increases. Others have found similar results (e.g., Bai et al. 2009; Mahajan et al. 2010). The slight increase in the IR/FUV early-type galaxies toward the center of the cluster is likely due to the morphology-density relation (and, similarly, the mass-density relation).

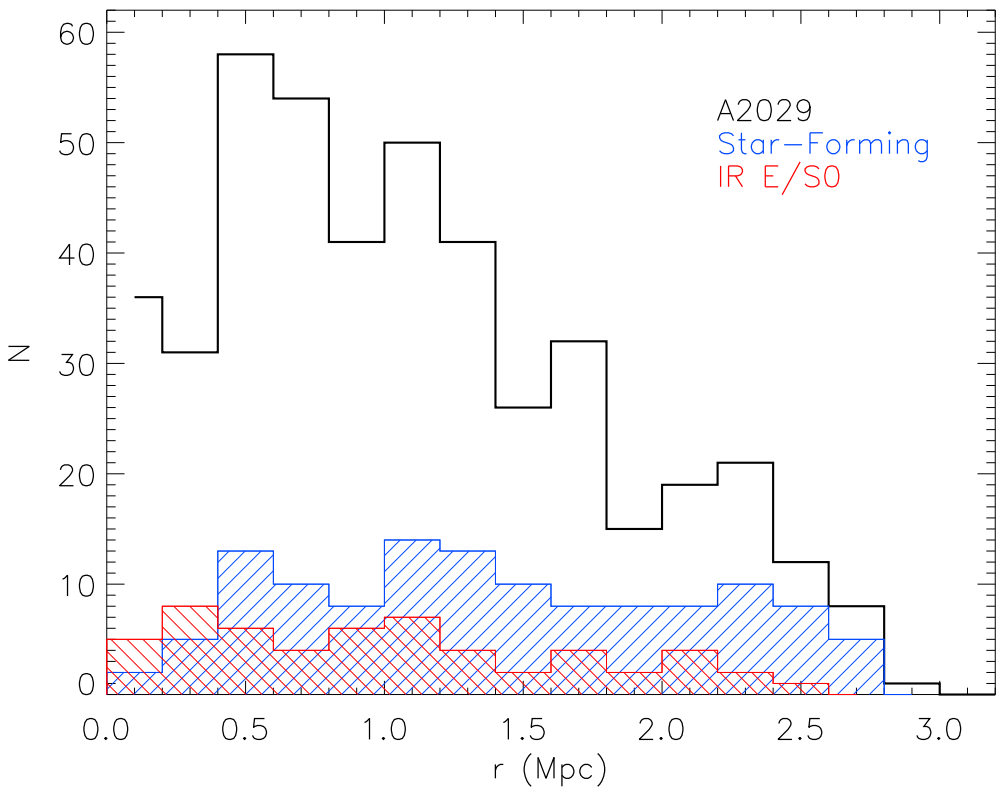

Figure 4.8 Histogram of all cluster galaxies (black bins), all star-forming galaxies regardless of detection method (blue hashed bins), and the 24 μm- and FUV- detected non-star-forming early-type galaxies (red filled bins). The distribution of star-forming galaxies is independent of radius while the non-star-forming early-types tend to favor small radii. If we model the star-forming galaxies as being uniformly distributed outside of the core (>1 Mpc), we get a more constant overall distribution, similar to what is shown here. This indicates that the star-forming population lies outside the cluster core; this highest-density region of the cluster should quench star formation more strongly than the outskirts regardless of the suppression mechanism. Non-star-forming early-type galaxies are slightly more concentrated toward the center of the cluster due to the mass–morphology relation.

4.6 Comparison with Other Clusters & the Field

Expanding on the results for A2029 requires comparing them with other nearby, dense clusters. Coma is excellent for this purpose because it has good 24 μm coverage that goes deeper in luminosity than that for A2029 due to the proximity of the cluster. These data have been studied by Bai et al. (2006) and Edwards & Fadda (2011). Bai et al. (2009) have also presented a 24 μm study of A3266 and compared it with Coma, effectively including some aspects of A3266 in our analysis.

4.6.1 SFR Function

Because we do not have sufficient data at the faint end to constrain the shape of our SFR function, we use the faint-end slope of previous studies to compare with A2029. The dashed grey line in Figure 4.6 is the multi-cluster composite Schechter function from Bai et al. (2009), normalized to A2029 using a χ^2 minimization routine. We then fit a Schechter function to our cluster using the same faint-end slope but allowing SFR* to vary (solid grey line). This results in log(SFR*/(M$_\odot$ yr^{-1})) $\sim 0.27 \pm 0.04$, a lower value than the composite, which is $\sim 0.45^{+0.13}_{-0.12}$ when redshifted to our cluster using Le Floc'h et al. (2005). However, given the error bars and the overall fits to the data, both Schechter functions are comparable and reasonably good representations of A2029.

The Bai et al. (2006, 2009) studies only use 24 μm detections for their luminosity functions. In Figure 4.9, we use 24 μm only to estimate SFRs using Rieke et al. (2009), which was shown in Bai et al. (2009) to be comparable to their own template-fitting method for estimating SFRs. The vertical dashed black line indicates the 24 μm detection limit using this IR-to-SFR conversion; we do not use the data point below this limit in any fits. The dashed red line shows the best-fit

Schechter function from the Bai et al. (2009) composite cluster luminosity function normalized to A2029 (black filled circles). If we remove the 24 μm-detected galaxies that we previously identified as not forming stars (blue triangles) and refit the composite Schechter function (solid red line), we find the composite to be a much better representation of our cluster than when we included the non-star-forming early-types. Even if Coma and A3266 also have a population of non-star-forming 24 μm galaxies that were included in their luminosity functions, their IR SFRs are low enough that they would be below our completeness limit for A2029. In other words, accidentally including non-star-forming 24 μm galaxies in Coma and A3266 does not change the similarities between their SFR function and that of A2029. All three clusters can be fitted by the same luminosity function, found by Bai et al. (2009) to also be very similar to the field luminosity function.

4.6.2 Mass–SFR Relation

Edwards & Fadda (2011) included multiple wavelength data in their study of Coma, including emission line measurements. Figure 4.10 shows the same total SFR vs. stellar mass as Figure 4.7, including A2029 (red filled circles) and Coma (blue filled triangles). The Coma galaxies are adapted from Edwards & Fadda (2011); we only included galaxies with both 24 μm and Hα detections. (Only a few Coma galaxies with spectra are not detected at Hα, and the authors do not distinguish these galaxies from the ones that do not have spectra.) The total SFRs for Coma were calculated in the same way as for our cluster. A subset of the Coma galaxies was listed in SDSS, allowing us to compare our method for estimating stellar masses with theirs. Because the two techniques resulted in masses within a factor of two for most of the galaxies, we use the masses listed in Edwards & Fadda (2011) for all Coma galaxies. The horizontal dotted line is our 24 μm detection limit; the detection limit for Coma appears to be at a similar

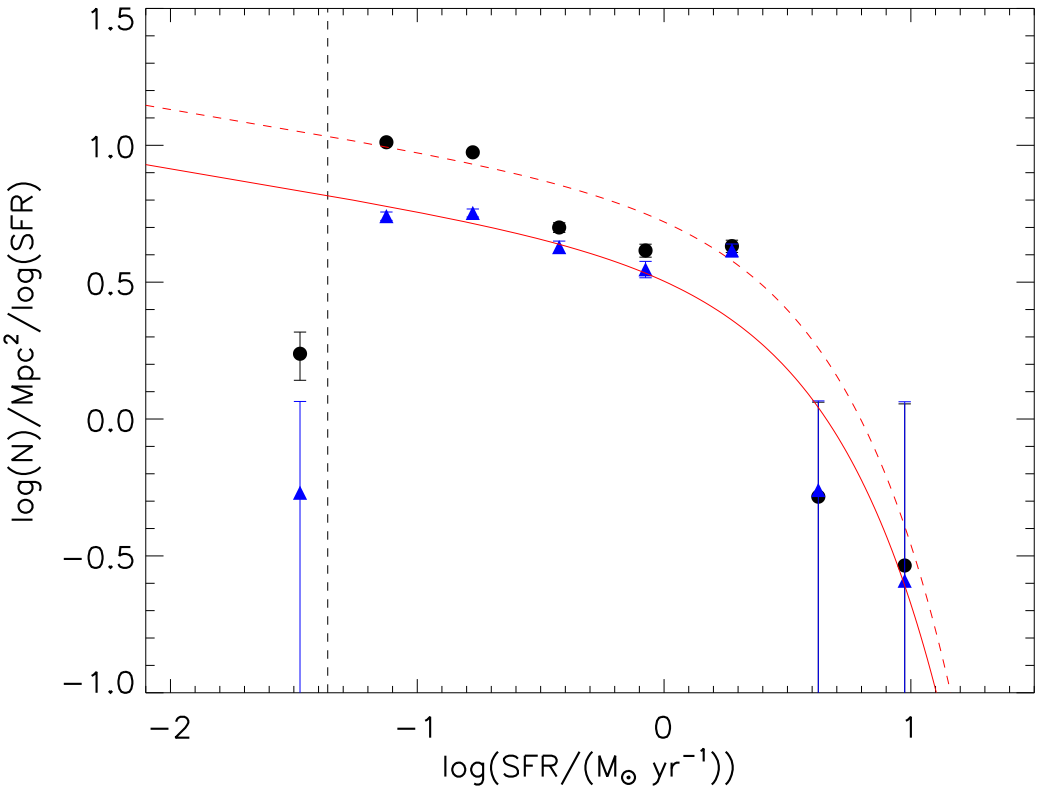

Figure 4.9 SFR function for all 24 μm-detected galaxies in A2029 (black circles) and for all 24 μm-detected galaxies not including those identified as non-star-forming early-types (blue triangles). The best-fit Schechter function for the Bai et al. (2009) composite cluster normalized to A2029 using χ^2 minimization for all 24 μm sources is shown by the red dashed line, while the same fit normalized to the star-forming galaxies only is shown by a solid red line. The composite Schechter function fits the A2029 data well when the non-star-forming galaxies are removed. The vertical black dashed line indicates the 24 μm detection limit.

level (in terms of Hα detections).

The black dashed line is adapted and modified from Brinchmann et al. (2004), who found a strong relation between stellar mass and SFR for field galaxies. Up to $\log(M_*/M_\odot) \sim 10.5$, this relation is linear; the SFRs of higher-mass galaxies drop off and become more uncertain due to lower numbers of these galaxies and the larger proportion of early-types at high mass. We extrapolate the linear relation in this region to represent only the late-type population (as is also done by Elbaz et al. 2007). To avoid this region, and because of our completeness limit, we only compare galaxies in the mass range $9.0 \lesssim \log(M_*/M_\odot) \lesssim 10.5$. The mode of the Brinchmann et al. (2004) relation follows the distribution of star-forming galaxies, so we use the mode as the basis of our field comparison[6].

To accurately compare the Brinchmann et al. (2004) relation to our clusters, we need to minimize any systematic differences between the two studies. We calculated the SFR and stellar mass in the same manner as A2029 for a complete sample of galaxies from the Boötes field (Rujopakarn et al. 2010; not including AGN) and combined it with our own field galaxies. We then fit a line to the mode of the Brinchmann et al. (2004) relation and normalized it to our combined field sample. This normalized relation falls on the black dashed line shown in Figure 4.10; we will refer to it as the overall "field relation" from now on.

A2029 and Coma seem to mostly follow the field relation, though Coma appears to have a larger number of high-mass, low-star-forming galaxies. This is easier to see in Figure 4.11, where we show the SFR offset between the cluster galaxies and the field for $9.5 \lesssim \log(M_*/M_\odot) \lesssim 10.5$. The solid black line is the average distribution of field galaxies at these masses (Brinchmann et al., 2004), while the red dashed line and blue dotted line are the distributions of A2029 and

[6]The mean is influenced by the more quiescent galaxies and so is not a good representation of the overall trend.

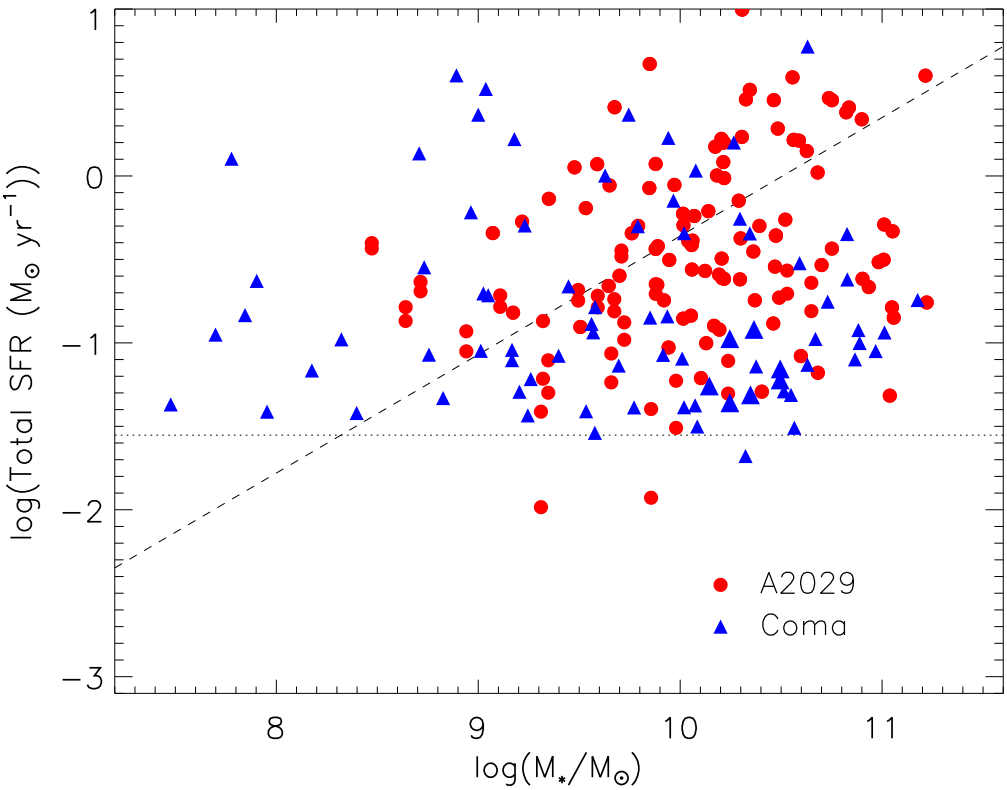

Figure 4.10 SFR vs. stellar mass for A2029 (red circles) and Coma (blue filled triangles; Edwards & Fadda 2011). Larger blue-filled triangles are AGN (see text). The IR detection limit for A2029 is shown as a horizontal dotted line; the Hα detection limit for both clusters should be comparable and near the IR limit. The mode of the overall field relation for SFR and stellar mass (normalized to a sample of local field galaxies) is shown as a dashed line (Brinchmann et al., 2004). Coma seems to have more massive, low-star-forming galaxies than A2029, which follows the field relation fairly well.

Coma galaxies, respectively. A2029 follows the field very closely, while Coma has more low-SFR galaxies than either the field or A2029, as we noted earlier. In addition, due to the targeting of IR-bright galaxies for spectroscopy (Edwards & Fadda, 2011), massive quiescent galaxies are missing from the Coma sample. The detection limit for both clusters (vertical dashed line) is for $\log(M_*/M_\odot) = 9.5$. The incompleteness slowly increases for masses increasingly below this limit. A completeness-corrected version of the figure is discussed in the following section.

One issue with the Coma SFRs is the Hα aperture corrections (Edwards & Fadda, 2011). The size of the spectral fibers used for Coma tends to be smaller than the galaxies themselves, indicating that some Hα luminosity is lost. Edwards & Fadda (2011) estimate corrections for this lost light based on the galaxy continuum photometry and state that the median aperture correction is $\sim$2, though some can be as high as 10. Because the star-forming regions are likely to be distributed differently from the optical continuua, we test the effects of different aperture corrections. Figure 4.12 shows the field (black solid line) and Coma (blue solid line) distributions with aperture correction factors of zero (no correction), two, four, and eight. These plots show that only the most extreme corrections (all galaxies corrected by a factor of eight, which is a huge overestimation since Edwards & Fadda (2011) find that few galaxies need such a high correction) begin to remove the population of low-SF galaxies in Coma. We conclude that this small population of star-forming galaxies is real and not a selection effect. We use the median correction of two below.

To demonstrate that the correction should be no larger than a factor of two, we carried out another test. The 24 μm fluxes represent the total star formation over the full galaxy (beam of 6″, extended emission captured to first order through SExtractor), and we can compare them with the Hα measurements to see if there

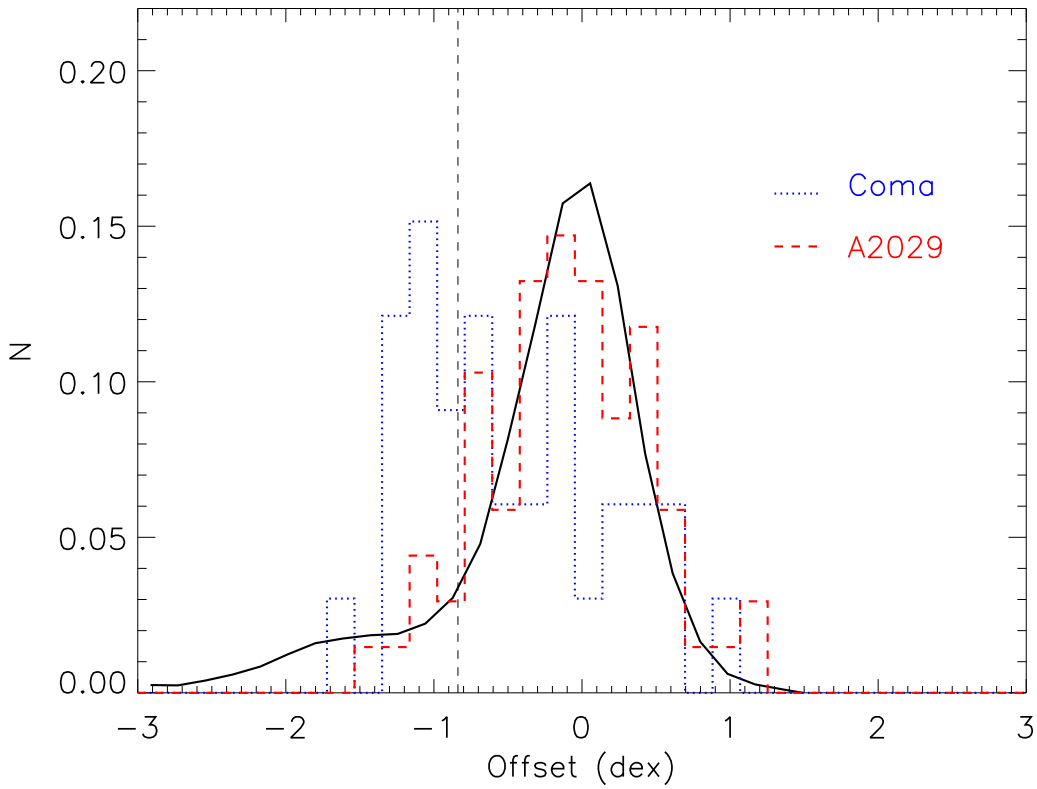

Figure 4.11 Offset from the Brinchmann et al. (2004) field relation (black line) for A2029 (red) and Coma (blue) for all star-forming galaxies at $9.5 \lesssim \log(M_*/M_\odot) \lesssim 10.5$. The vertical dashed line is our completeness limit given the detection limit at $\log(M_*) = 9.5$. A2029 closely follows the field, while Coma has a population of galaxies that fall below the field relation.

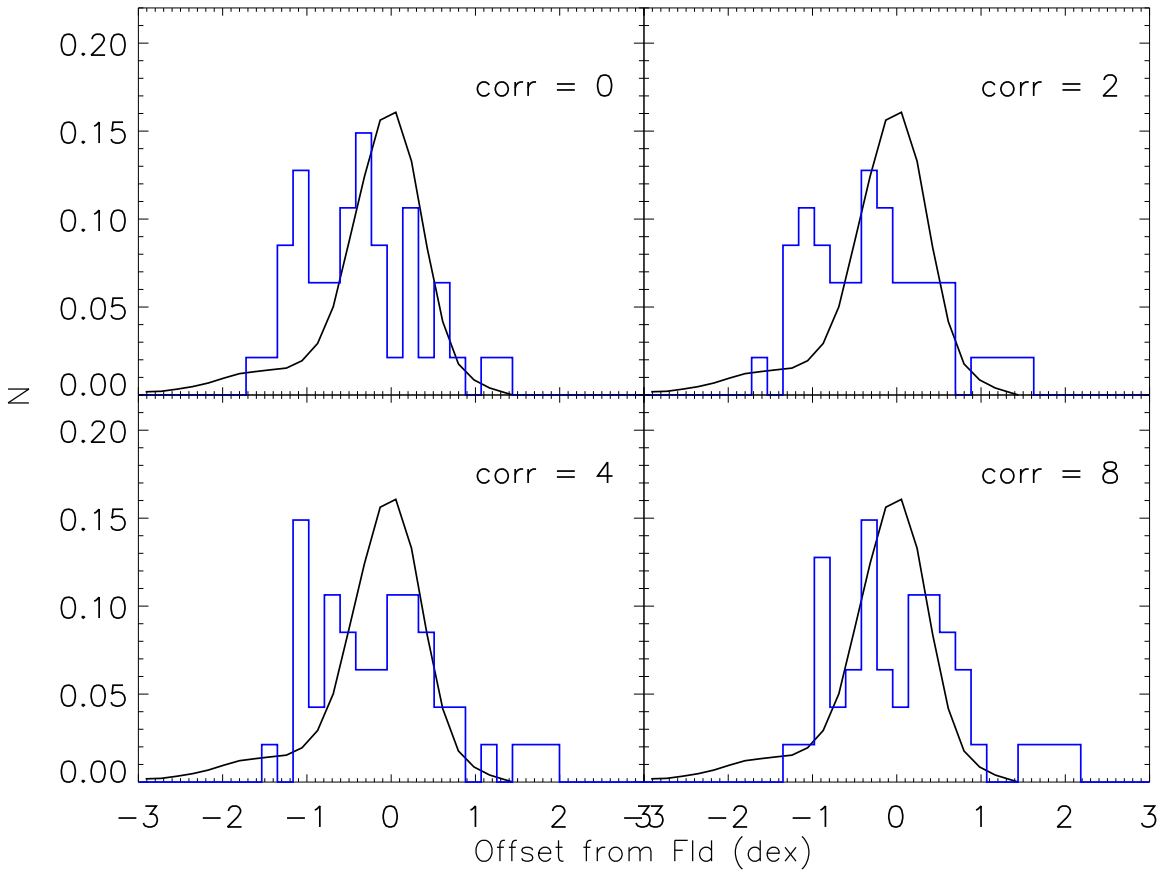

Figure 4.12 Testing different Hα aperture corrections for Coma star-forming galaxies by imposing correction factors of 0, 2, 4, and 8. The black line represents the distribution of SFRs of field galaxies compared with the median (zero offset), while the blue line is the distribution of star-forming galaxies in Coma. Except for the highest correction factor (which would only be needed for a handful of galaxies), there still exists the population of galaxies with SFRs significantly below the field average.

is a tendency for the latter to be systematically too small. For this test, we used the SINGS sample, for which integrated 24 μm and Hα fluxes are available (Kennicutt et al., 2003). We restricted the test to galaxies with SFRs between 0.1 and 1 $M_\odot$/yr to have good statistics and comparable SFRs in the samples. We found that there was no significant difference between the $SFR_{24}/SFR_{H\alpha}$ for the Coma galaxies (mean 10, median 4) and the SINGS galaxies (mean 8.6, median 6.8), suggesting that virtually no aperture correction may be needed for most of the Coma Hα measurements.

In the case of A2029, the projected fiber diameters are already about twice those for Coma, and our use of continuum photometry to convert equivalent widths to line fluxes implicitly makes a first-order aperture correction. We therefore make no additional adjustments for the size of the spectroscopic aperture.

4.6.3 Anemic Coma Galaxies

The analysis in the preceding section has identified a significant population of star-forming galaxies in Coma that fall significantly below the field mass–SFR relation. Figure 4.13 shows the offset of all star-forming Coma galaxies (blue solid line) from our normalized field relation and the distribution of star-forming field galaxies around the Brinchmann et al. (2004) relation (black dashed line) for three mass bins. As the masses of Coma galaxies increase, the characteristic SFR decreases with respect to the field. How are these galaxies different from the other star-forming galaxies?

We extracted the subset of 13 massive ($10 \lesssim \log(M_*/M_\odot) \lesssim 10.5$) galaxies that lie significantly below the field relation (offset $\lesssim$ -0.7) for closer study. These galaxies are listed in Table 2. First of all, these galaxies are fairly evenly distributed in terms of projected area in the cluster, which, as we showed earlier with A2029, means most if not all of the galaxies are in the outskirts. Secondly,

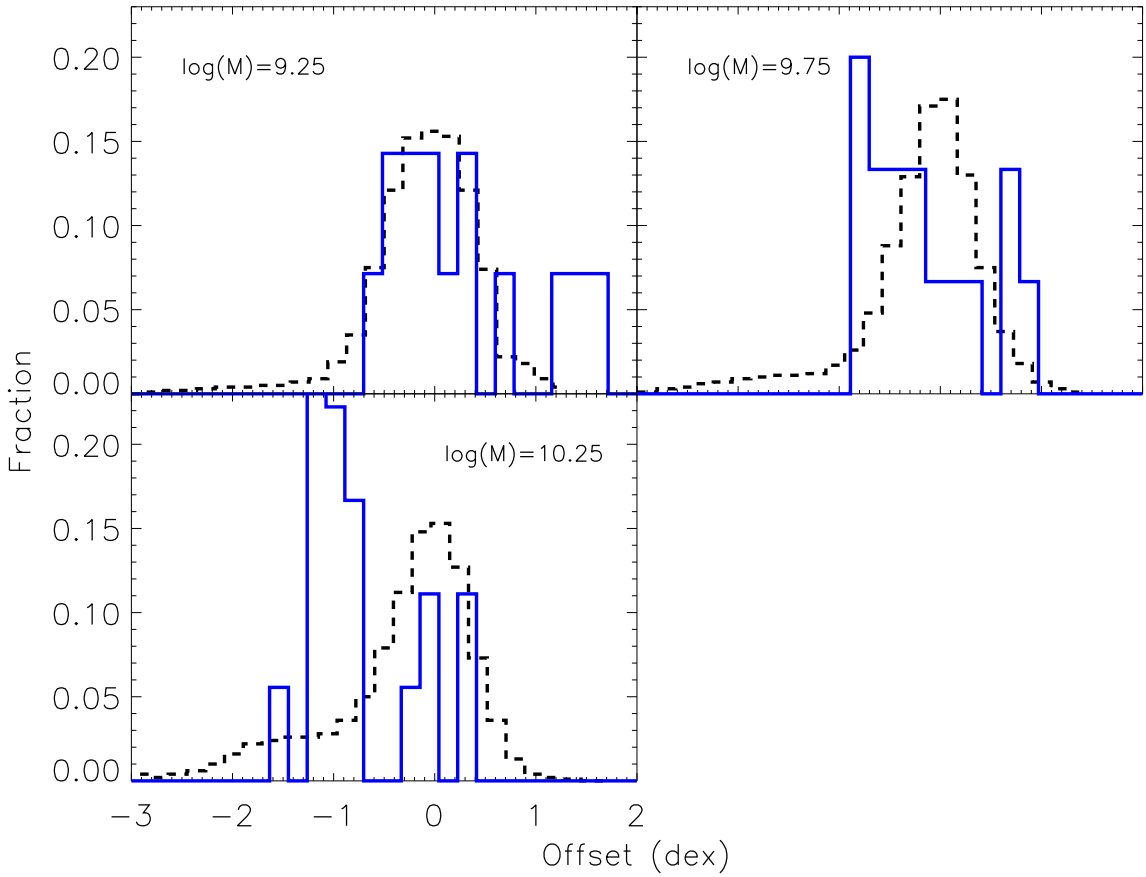

Figure 4.13 Same as Figure 4.11 for Coma but separated into different mass bins. The black dashed line is the offset for the Brinchmann et al. (2004) field galaxies as compared with the mode of the field relation and the blue line is the same but for Coma's star-forming galaxies. Coma's population of low-star-forming galaxies (as compared with the field) is most prominent at higher masses; in the lowest mass bin, Coma's star-forming galaxies are comparable with the field.

almost all are early-type galaxies, with over half being S0s, specifically. None show obvious signs of ongoing merger activity, though some have indications of previous interactions (e.g., rings). We classify this small population of high-mass, low-star-forming Coma galaxies as "anemic," a term defined by van den Bergh (1976) to identify spiral galaxies with abnormally low amounts of gas and star formation as compared with "normal" spirals. He also identified the brightest cluster spiral, NGC 4921, as anemic as well, and we include it in our table of anemic Coma galaxies.

Another interesting aspect of these galaxies is that over half were previously identified as hosting an AGN (shown in Figure 4.10 as larger blue triangles), along with NGC 4921. Indeed, it could be that their outputs are dominated by the AGN and that our conclusion that they are anemic is not entirely correct. This possibility could be tested using the diagnostic diagrams proposed by Lacy et al. (2004) or Stern et al. (2005) since both approaches identify AGN that dominate the mid-IR output of a galaxy by the filling in of the spectral dip near 5μm by warm dust heated by the AGN. However, IRAC measurements are available for only two of the anemic galaxies.

Donley et al. (2012) show that the color selection methods are basically equivalent to selecting objects with power-law mid-IR spectra, so we will use an analog of the Lacy/Stern plots using WISE photometry instead. The resulting diagnostic diagram is shown in Figure 4.14. The dark green line shows the power-law locus, running from indices of -0.25 to -2.25. The green triangles are Seyfert galaxies, divided roughly equally between Type 1 and Type 2 (NGC 1275, 3227, 3516, 3783, 4051, and 4151; Mrk 1, 6, 9, 78, 79, 176, 198, 273, and 348). The red stars are a selection of low-luminosity ($8 < \log(L_{TIR}) < 10$; Sanders et al. 2003) star-forming galaxies, and the black square is the color of a template of a low-luminosity star-

Table 4.2. Anemic Coma Cluster Galaxies

Catalog ID	RA	Dec	Morphology	log(M_*) ($M_\odot$)	Total SFR ($M_\odot$ yr^{-1})	AGN?
-	194.48608	27.037508	-	10.25	0.106	Y
-	194.14433	27.22756	S0	10.37	0.120	Y[a]
-	194.29483	27.404902	Sa	10.14	0.055	Y
-	194.65758	27.464002	S0	10.35	0.049	Y[a]
MCG+05-31-036	194.47652	27.490639	SBb	10.25	0.044	Y
-	194.17664	27.548255	S0	10.32	0.021	N
-	194.26768	27.730046	S0	10.02	0.041	N
MCG+05-31-007	193.85438	27.798033	Sp	10.38	0.072	N
IC 4042	195.17815	27.971266	SB0	10.50	0.070	Y
NGC 4907	195.20335	28.158341	SBb	10.49	0.060	Y
-	196.04228	28.247957	S0	10.08	0.032	N
MCG+05-31-110	195.67002	28.371308	S0/Sp	10.07	0.042	N

[a]We retrieved 20 cm data from Miller et al. (2009) and found the IR-radio q parameter (q = $\log(F_{24}/F_{20cm})$) to be indicative of an AGN.

[b]Classic anemic galaxy in Coma, not identified as anemic in our sample due to its high mass. Morphology from de Vaucouleurs et al. (1991).

Note. — Description of columns: (1) Catalog ID of the galaxy (if available); (2),(3) SDSS coordinates; (4) Galaxy morphological type as listed by the SIMBAD database; (5) Stellar mass, in solar units, adapted from Edwards & Fadda (2011); (6) Total SFR using 24 μm and Hα from Edwards & Fadda (2011), calculated using the same method as A2029 (assuming all 24 μm emission is from star formation); (7) Flag for whether the galaxy is known to have an AGN or not (most identified via SIMBAD). The complete table is available in electronic format.

forming galaxy based on the templates of Rieke et al. (2009). The Coma anemic galaxies are the blue circles. They fall exactly in the locus of the other star-forming galaxies, demonstrating that their mid-IR outputs are dominated by stellar power and that their SFRs are correctly deduced from IR luminosities. We also show the colors of a number of massive early-type galaixes in Coma, selected not to show indications of star formation in optical spectra (i.e., no Hα emission) (e.g., Moss & Whittle 2005; Miller et al. 2009). Two of these galaxies fall in the star-forming zone, indicating that low levels of star formation may have been overlooked in the optical spectroscopy; the remaining 11 galaxies define a distinct locus that shows the behavior of the IR excesses in quiescent early-type galaxies. Thus, the properties of the anemic galaxies in the mid-IR are inconsistent with those of AGN-dominated galaxies or quiescent ones, but they do indicate significant levels of star formation.

It is difficult to determine the prevalence of these high-mass, low-star-forming galaxies in Coma, both because of the AGN contamination and because of the detection limit at $\log(M_*/M_\odot) \sim 9$ and corresponding field offsets $\lesssim$ -0.7 dex. We need to correct for any galaxies we may be missing below our detection limit. We do not have enough data to correct for the incompleteness for galaxies below $\log(M_*/M_\odot) \sim 9.5$, so we focus on galaxies from $9.5 \lesssim \log(M_*/M_\odot) \lesssim 10.5$. The results are shown in Figure 4.15. For each of the first three bins below offset $\sim$ -0.7, we calculate a completeness correction using the ratio of areas and number of sources above and below the detection limit in each bin. The solid black, dashed red, and dotted blue lines (the field average, A2029, and Coma, respectively) are the same as in Figure 4.11 except for the completeness corrections. Our new completeness limit, with the corrections, is shown as a vertical black dashed line. Even with completeness corrections, A2029 does not have the low-star-forming

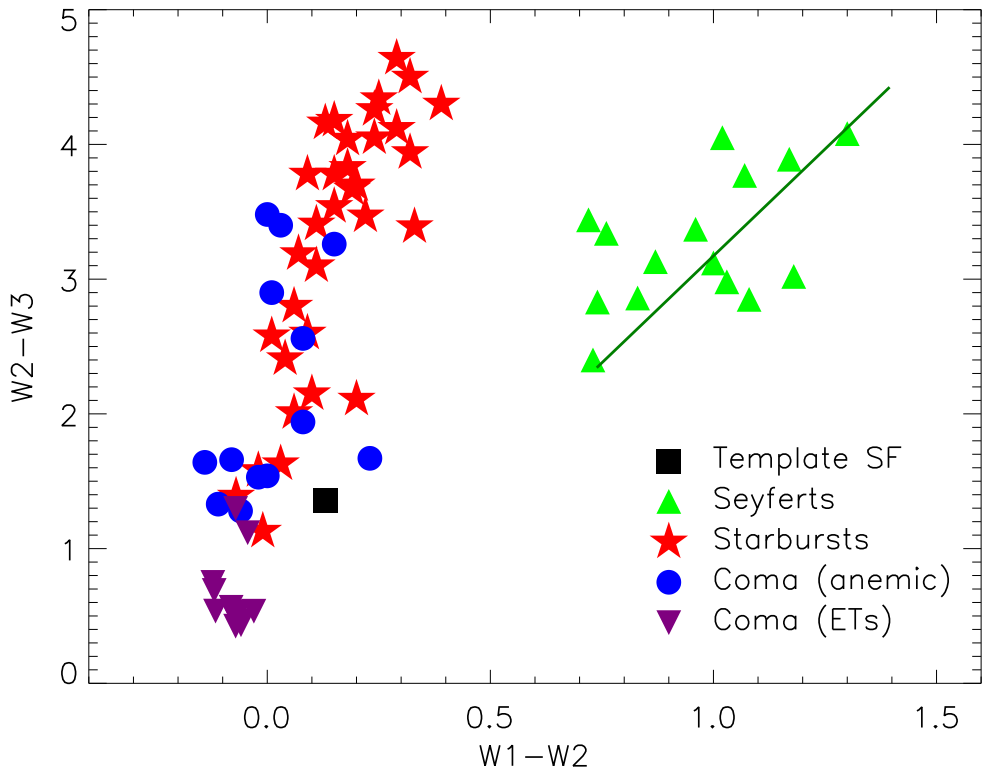

Figure 4.14 AGN diagnostic for WISE sources: local Seyferts (green triangles), local starbursts (red stars), star-forming galaxy template from Rieke et al. (2009; black square), and anemic Coma galaxies (blue circles). The dark green line shows the power-law locus, running from indices of -0.25 to -2.25. While over half of the anemic Coma galaxies are known to harbor AGN, they fall within the star-forming galaxy region using this mid-IR diagnostic, indicating that star formation dominates the IR output of the anemic galaxies.

galaxies that Coma has—its star-forming galaxies are still comparable to the field star-forming population.

4.6.4 24μm-Emitting Early-Type Galaxies

We also discovered that Coma, too, has non-star-forming early-type galaxies with 24μm emission, like A2029. These galaxies are shown in Figures 4.14 and 4.16. We collected a sample of 13 normal early-type galaxies in Coma, all of which have WISE and 24μm coverage but do not have Hα emission. In Figure 4.14, the WISE colors of these galaxies (purple down triangles) indicate that most are indeed passive; only a couple have possible residual star formation.

All but two of these Coma galaxies have 24μm emission as well, so we added them to the Temi et al. (2009) plot used earlier to show that the IR emission from passive, early-type A2029 galaxies is mostly from the old stellar population (Figure 4.16). All points are the same as in the previous plot (Figure 4.5) except that the only A2029 galaxies we include are the early-type galaxies not detected in Hα. The Coma galaxies, shown as yellow stars, occupy the same region of the plot as the passive A2029 galaxies, indicating that the IR emission from all of these galaxies is from the same source—old stars—rather than star formation.

4.7 Discussion

A surprising result from previous studies of rich galaxy clusters is that their IR luminosity functions appear to be very similar to that of field galaxies at the same redshift (Bai et al. 2009), although the fraction of galaxies emitting at a detectable level in the IR is much smaller than in the field. Only by carefully combining measurements of a number of clusters were Atlee & Martini (2012) able to find evidence for a subtle difference between the field and average cluster IR luminosity functions.

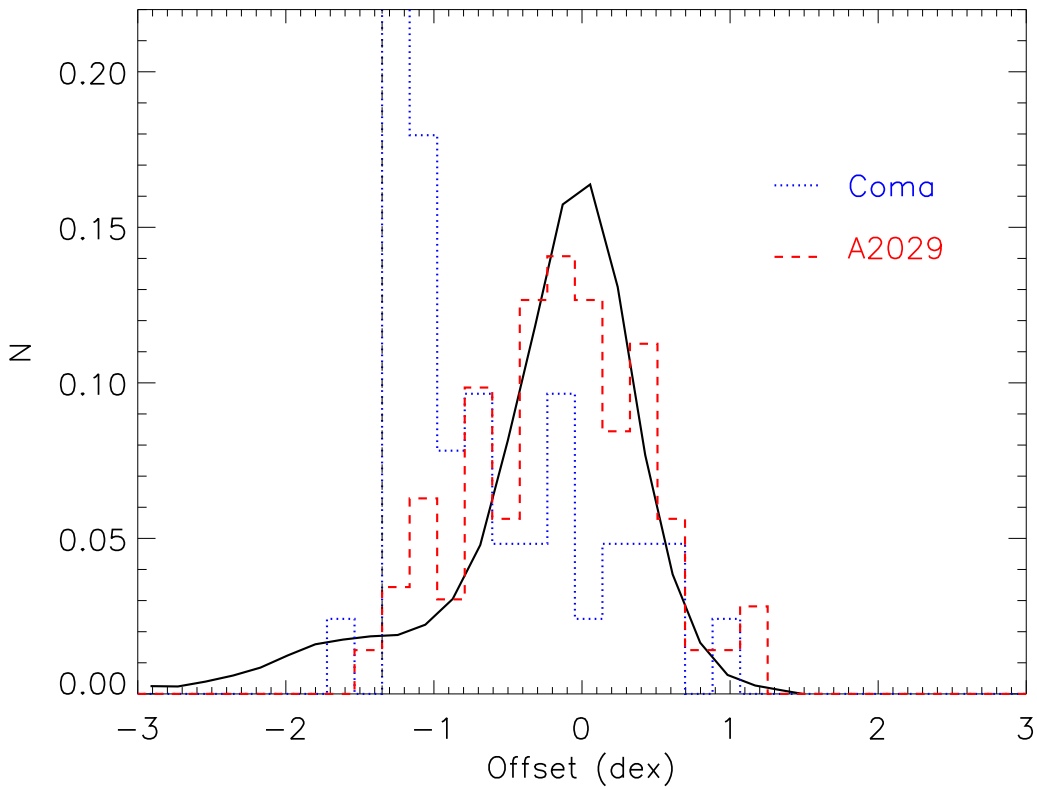

Figure 4.15 Same as Figure 4.11 but including completeness corrections for both clusters. The vertical dashed line is the completeness limit for the corrected distributions. Even corrected for missing galaxies, A2029 looks like the field, while Coma retains its population of star-forming galaxies that lie far below the field relation (black line).

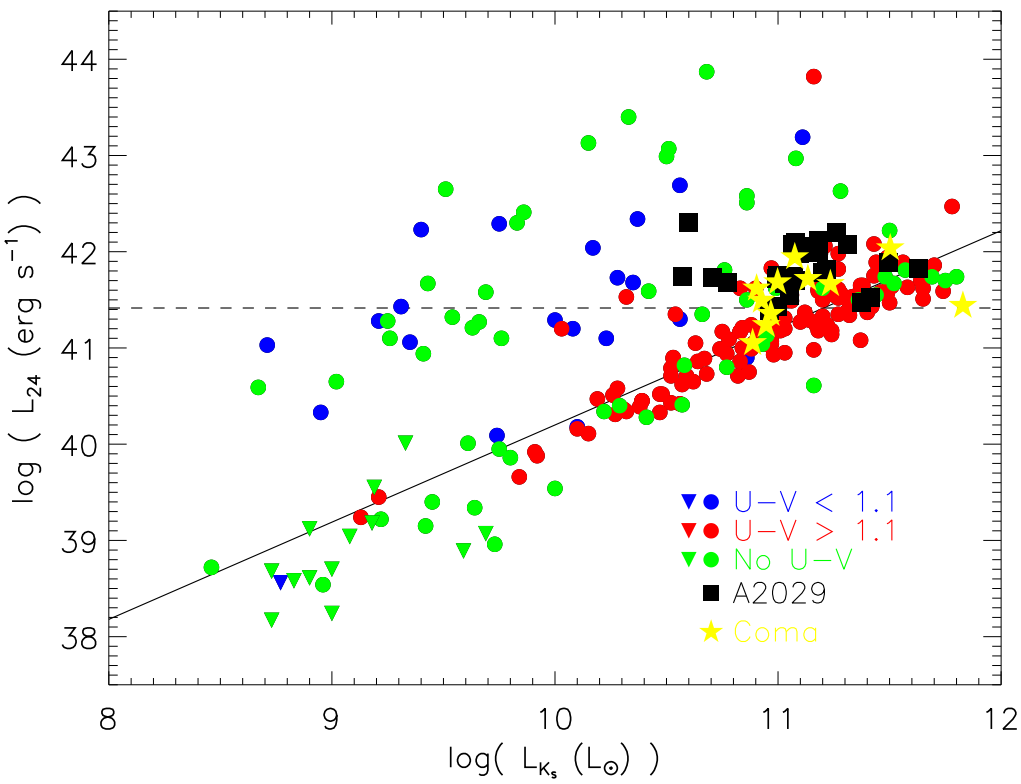

Figure 4.16 Same as Figure 4.5 but with a sample of non-star-forming Coma early-type galaxies with 24μm emission. These galaxies fall in the same passive region of the plot as our A2029 non-star-forming early-type galaxies, indicating a similar population of galaxies exists in Coma as well.

However, our more detailed examination of the components of the IR-luminous cluster population shows some interesting features that can be missed in the luminosity function alone. We find that the large proportion of early-type galaxies in dense clusters yields a significant number of such objects that are detected in deep IR surveys but that are not forming stars at the indicated level; their IR outputs are probably related to AGN and mass loss from old stars. These objects must be removed from the luminosity function if it is to be compared correctly with the field.

After removing these objects and correcting for incompleteness, we have shown that the distribution of SFRs in A2029 is nearly identical to that of the field. Since the bulk of this cluster is relaxed and evolved, it appears that its star-forming population has been acquired relatively recently and that there has not been sufficient time to quench the star-forming activity. It is noteworthy that these galaxies are not more active than field galaxies either, since some hypotheses would suggest an increase in activity upon the initial encounter with a dense cluster. Even if the outermost gas is removed from a galaxy, it is thought that the dense molecular clouds could remain (Boselli & Gavazzi, 2006) and that they might sustain star formation for about 2 Gyr (Bigiel et al., 2011), putting a rough limit on the time since the A2029 galaxies might have been accreted. In comparison, in the Coma cluster there is a population of early-type galaxies (including early spirals) that falls below the field mass–SFR relation, indicating that we are seeing them in the process of being quenched. These galaxies lie in the outer zones of the cluster rather than in the center, requiring either that the quenching mechanism be active there or that they were quenched on plunging orbits that have returned them to the outskirts of the cluster. The differences between the star-forming populations is most easily explained as differences in the history of accretion of field galaxies

in the two clusters, so long as the quenching process is delayed by a sufficient interval to account for the absence of quenched galaxies in A2029 but is not so slow that it cannot account for the anemic galaxies in Coma.

Boselli & Gavazzi (2006), and references therein, review in detail the multitude of processes that could be responsible for the quenching of star formation in groups and clusters and the types of environments in which each could dominate or be most efficient. The lower-density group environment is a prime location for harassment and tidal forces between galaxies themselves due to the higher incidence of interactions and slower velocities needed to strip significant amounts of gas from the galaxies (e.g., Merritt 1984; Byrd & Valtonen 1990; Boselli & Gavazzi 2006). The dominant mechanisms in clusters, however, are more likely to be starvation/strangulation, ram-pressure stripping, and thermal evaporation (the ISM of the galaxy is heated by the ICM enough that the galaxy's graviational potential is unable to retain the gas; e.g., Cowie & Songaila 1977). We can rule out thermal evaporation considering that this mechanism is most effective at low masses, and our anemic Coma galaxies are of much higher mass (Boselli & Gavazzi, 2006). Ram-pressure stripping can occur throughout most of the cluster, though it is most efficient in the densest regions; starvation/strangulation is more likely to occur in the outskirts of clusters, explaining why even star-forming galaxies in the outermost regions of clusters can have suppressed star formation as compared with the field (Boselli & Gavazzi 2006). The location of Coma's star formation suppressed galaxies in the outskirts suggests starvation/strangulation is dominating, but as we mentioned previously, it is possible that the galaxies have already made one pass through the cluster, opening the possibility for ram-pressure stripping as an important quenching mechanism.

Interestingly, Boselli & Gavazzi (2006) also mention that tidal interactions (say,

between galaxies and the cluster potential), though not a dominant mechanism for quenching galaxy-wide star formation, can funnel material to the nuclei of galaxies, possibly triggering a short burst of star formation at the galaxies' centers. This material and/or the sudden increase in star formation would help feed a low-luminosity AGN, which could at least partially explain the high incidence of AGN in the anemic Coma galaxies (Lake et al., 1998).

It should be noted, though, that we are focusing on the star-forming galaxies with $9.0 \lesssim \log(M_*/M_\odot) \lesssim 10.5$. As mentioned previously, low-mass galaxies can be more easily affected by a dense environment than higher-mass galaxies (Boselli & Gavazzi 2006 and references therein). Depending on the field mass–SFR relation at $\log(M_*/M_\odot) > 10.5$, both A2029 and Coma could have significant numbers of galaxies forming stars at rates lower than expected for the field relation, indicating ongoing quenching in the most massive galaxies as well. Perhaps studying the lowest- and highest-mass galaxies would help pinpoint the dominant mechanism(s) responsible for quenching star formation in the most dense regions of the universe.

4.8 Conclusions

We studied the 24 μm, Hα, and UV star formation indicators for galaxies in clusters Abell 2029 and Coma. A2029 is relaxed, with no obvious substructures, making it a good target for observing how dense environments affect star-forming galaxies over time. Coma is a good comparison cluster due to its proximity and abundance of multiwavelength observations.

The star-forming galaxies in A2029 follow the field mass–SFR relation. Coma, while having a population of star-forming galaxies that echoes the field, has an additional population that lies far below the field relation, indicating these galax-

ies are in the process of being quenched. A large fraction of these galaxies also host AGN. We are unable to identify the dominant mechanism responsible for suppressing star formation, though we suspect ram-pressure stripping and starvation/strangulation are the most likely. Given the field-like population of star-forming galaxies in A2029, it appears that these galaxies have been accreted very recently (within 2 Gyr) and have not yet had time to be quenched. The incidence of suppressed star formation in Coma indicates that it accreted a significant number of galaxies longer ago.

Additionally, we discovered a population of 24 μm- and/or FUV-emitting early-type galaxies in A2029 with no evidence of star formation, whose IR emission may arise from AGNs or old stellar populations.

Chapter 5

Star Formation in X-Ray Underluminous Clusters

It has long been known that dense environments, like clusters, greatly affect the properties of galaxies: color, morphology, mass, star formation. What remains unknown, however, is what mechanism is most responsible for these changes. The two most widely favored cluster mechanisms for quenching star formation, ram-pressure stripping and starvation/strangulation, rely on hot X-ray gas (the intracluster medium, or ICM) to strip material from infalling galaxies, but recent studies have shown a population of clusters with significantly less core X-ray emission than expected given their mass. However, recent work has shown that clusters once identified as being X-ray underluminous may, in fact, simply be normal clusters with different X-ray temperatures and/or orientations. There are indications that the total mass in intergalactic gas in these clusters is similar to that in others, but since the configuration of this gas is different, these clusters might have a different population of star-forming galaxies than normal X-ray bright clusters. In this paper, we study four X-ray underluminous clusters (XUCs) to probe the effectiveness of the ICM at quenching star formation. Using Hα emission and 24 μm photometry to estimate total star formation rates, we find that the fraction of star-forming galaxies for these clusters is between normal X-ray clusters and the field. Also, the mass–SFR distribution varies depending on the cluster: one has star-forming galaxies reminiscent of the field and another has a large population of anemic galaxies. This indicates that some preprocessing occurs before galaxies enter the cluster environment, but the cluster (and, therefore, the hot ICM) is still responsible for some quenching of star formation.

5.1 Introduction

Galaxy properties are highly dependent on both the point in time when they are observed and their local environment, for as yet unknown reasons. In focusing on the latter effect, however, we have confirmed that high density regions are populated more by red, early-type galaxies with little or no star formation compared with the field, which is dominated by blue spiral galaxies readily forming stars (Dressler 1980; Balogh et al. 1997; Poggianti et al. 1999; Lewis et al. 2002; Gómez et al. 2003; van der Wel et al. 2007; Bai et al. 2009; Tempel et al. 2011). A variety of effects have been described to try to explain the changes we see in galaxies in different environments. In low- to mid-density regions, galaxy-galaxy interactions (harassment and mergers) are favorable and can affect galaxy morphology and, to a lesser extent, SFR (e.g., Barnes & Hernquist 1996; Mihos 2004; Conselice 2006). Other effects become dominant in dense clusters, typically involving interactions between the intra-cluster medium (ICM) and individual galaxies. The ICM can strip the gas from galaxies, resulting either in the removal of the hot halo around the galaxy (starvation/strangulation; e.g., Larson et al. 1980; Balogh, Navarro & Morris 2000; Kawata & Mulchaey 2008; McCarthy et al. 2008) or a complete removal of the gas (ram-pressure stripping; e.g., Gunn & Gott 1972; Kinney et al. 2004; van Gorkom 2004; Sivanandam et al. 2010). Starvation/strangulation causes star formation to slowly taper off as the galaxy uses up its gas reservoir in the disk and is unable to accrete more. Star formation in a ram-pressure stripped galaxy quickly subsides due to nearly all the gas—even in the disk—having been removed.

Given that the ICM has been deemed the most likely instigator in the depletion of star formation in the most dense regions, it makes sense to probe clusters that vary in terms of their hot X-ray gas. Recent work has discovered a popula-

tion of clusters with X-ray luminosities (L_X) well below the mass-L_X relation for normal, bright X-ray clusters (e.g., Balogh et al. 2002; Basilakos et al. 2004; Lubin et al. 2004; Popesso et al. 2007; Dietrich et al. 2009; Castellano et al. 2007). Some suspect that the low L_X of these clusters (referred to as X-ray underluminous clusters, XUCs, from now on) is due to the clusters still being in the process of forming, and the X-ray gas has not had time to collapse and heat to the expected temperature (Balogh et al. 1997; Popesso et al. 2007). Similarly, the clusters could be experiencing a merger event with another cluster, a rich group, or a series of groups, affecting the distribution of the X-ray gas so as to lower its overall density and, therefore, its luminosity (Barrena et al. 2002; Clowe et al. 2004; Popesso et al. 2007). However, there is evidence that these clusters are not actually underluminous in X-rays and, instead, have different X-ray temperatures and/or configurations.

No matter the reasons for some clusters having low L_X (or the appearance of low L_X), a less dense ICM or one with different properties could have a different impact on member galaxies if ram-pressure stripping or starvation/strangulation is responsible for quenching star formation. To test this hypothesis, we have selected four clusters previously identified as being X-ray underluminous (Balogh et al. 2002; Popesso et al. 2007)—Abell 117 ($z \sim 0.055$), Abell 2255 ($z \sim 0.080$), Abell 2026 ($z \sim 0.091$), and CL1633 ($z \sim 0.24$)—to target with MIPS 24 μm and optical spectroscopy. These four clusters are shown in Figure 5.1, along with the Popesso et al. (2007) Abell cluster galaxies (black filled circles), as compared with the typical L_X–M_{200} relation from their X-ray selected sample (solid line, with the 2σ scatter as dashed lines). Open colored symbols show our four XUCs with masses from Popesso et al. (2007); filled colored symbols show the same XUCs but with masses calculated from our new membership lists. Our IR and optical

data for these clusters, along with archival SDSS photometry, allow us to accurately identify cluster members and individual star-forming galaxies. The multi-wavelength observations are especially important for estimating SFRs due to the possible contamination of non-star-forming sources that occurs when focusing on only one star-formation indicator.

In Section 2, we discuss the photometric and spectroscopic observations, including cluster membership selection criteria. Section 3 includes our analysis and the results thereof, which we then discuss in Section 4 and conclude in Section 5.

Throughout the paper, we use the following cosmological parameters: $H_0 = 70$ km s^{-1} Mpc^{-1}, $\Omega_M = 0.3$, $\Omega_\Lambda = 0.7$.

5.2 Observations & Sample Selection

5.2.1 Observations

5.2.1.1 Optical Photometric Data

The clusters in our sample are chosen to be covered by both the imaging and spectroscopic surveys of the Sloan Digital Sky Survey (SDSS). (Cluster CL1633 is the only one without complete SDSS coverage.) The SDSS photometric survey provides a uniform data set to study the galaxy properties in these clusters, as well as identifying candidates for further spectroscopic observations. The SDSS model magnitudes are the linear combinations of best-fit exponential and de Vaucouleurs profiles and are recommended as the best estimates of magnitude by SDSS. As such, we use the model magnitudes retrieved from SDSS and correct them for Galactic extinction (O'Donnell, 1994).

We used these SDSS photometric data to estimate galactic stellar masses with the SDSS_KCORRECT routine within KCORRECT (v. 4.2; see Blanton et al. 2007 for details). KCORRECT uses different cosmological values and initial mass func-

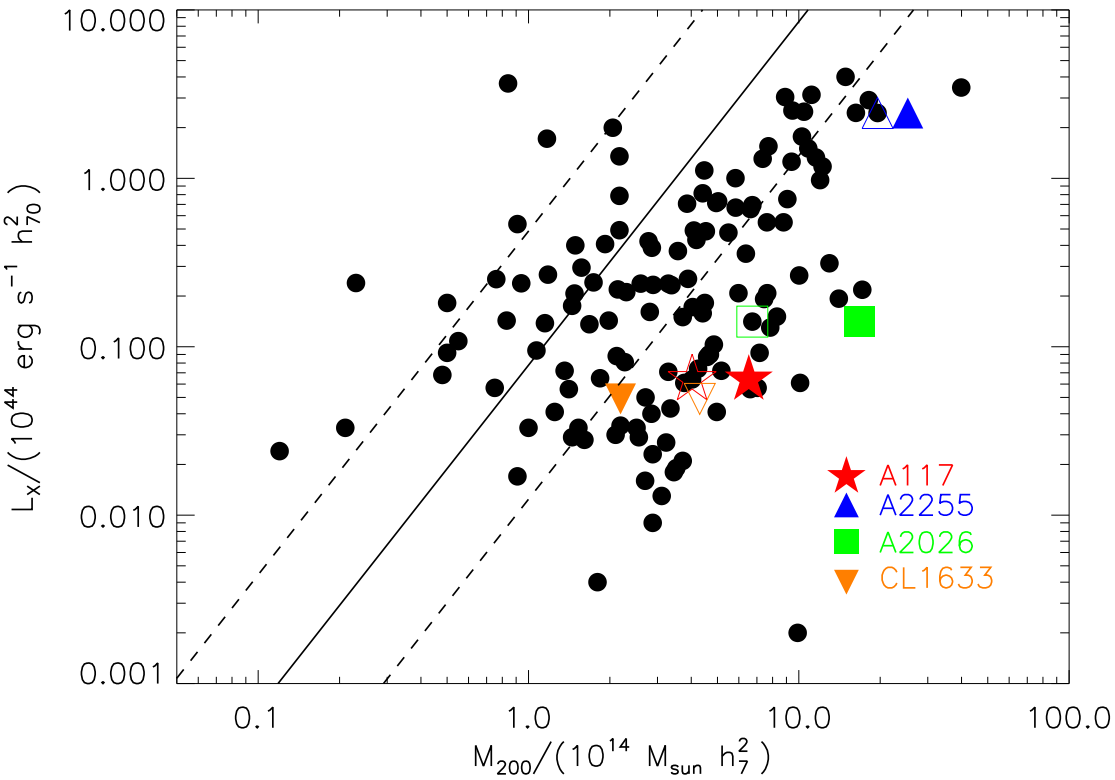

Figure 5.1 X-ray luminosity (L_X) vs. mass (M_{200}) for the Abell clusters in Popesso et al. (2007) (black filled circles; includes normal X-ray-emitting and X-ray underluminous clusters). The four X-ray underluminous clusters in our study are highlighted by different points. The open symbols are for values of M_{200} from Popesso et al. (2007); the filled symbols show the same four XUCs but with M_{200} calculated using our membership list. The solid black line is the relation for the Popesso et al. (2007) X-ray selected sample of normal X-ray-emitting clusters with 2σ offsets (dashed lines).

tion, so we corrected the original stellar mass output to the cosmology and IMF (Kroupa 2001) adopted in this paper.

5.2.1.2 Spectroscopic Data

We obtained optical spectra of cluster galaxies with Hectospec on the MMT, which is a multiobject spectrograph with 300 optical fibers (subtending 1.5" each) and a 1-degree field of view. We use the 270 line mm^{-1} grating, covering the wavelength range 3650-9200 $\AA$ with a spectral resolution of $\sim$5 $\AA$.

Spectroscopic targets were selected from the photometric SDSS catalog. For A117 and A2255, we selected all extended sources within the 1-degree field down to 4 magnitudes fainter than the BCGs. We excluded all optical source candidates with known redshifts from SDSS or the NASA Extragalactic Database (NED) with the exception of about 20 galaxies that we used for cross-calibration. A2255 was observed with MIPS before Hectospec, so we were able to assign a higher priority to objects with 24μm detections. We used two fiber configurations for A117 and one for A2255 with three 10-minute exposures for each configuration. For A2026 and CL1633, we selected sources from SDSS in a similar manner as the previous two clusters. One fiber configuration was used for A2026, while two were used for CL1633. We selected extended sources down to r = 20 mag for A117, r = 19.5 for A2255 and A2026, and r = 21 mag for CL1633.

We reduced the Hectospec data using HSRED, an IDL package developed by Richard Cool[1]. The redshifts of the spectra are measured using an automated cross-correlation routine in HSRED converted from the SDSS pipeline. For all observations, we visually inspect each spectrum to check the results and found that the automatic routine works very well for galaxies in the redshift range of interest.

[1]See http://www.astro.princeton.edu/$\sim$rcool/hsred/ or http://code.google.com/p/hsred/.

After combining the new spectroscopic data with the ones from SDSS and other literature, we assessed the completeness of the spectroscopic data. We calculate the completeness as the fraction of extended sources in SDSS photometric catalog with spectroscopy. In both A117 and A2255, the completeness is the same across the whole 1° field of view. In A117, the completeness is purely r magnitude limited and the measurements are about 80% complete down to r = 19.5. In A2255, we give the sources with 24 μm detection higher priority to the ones without. As a result, although the overall completeness drops to below 80% at r $>$ 18, the completeness for 24 μm souces is $\geq$ 80% down to r = 20. A2026 is nearly complete down to r = 19.5 mag. Given the limited SDSS coverage of CL1633, it is less than 50% complete down to r = 19 mag.

5.2.1.3 IR Observations

We observed the central r $<$ 0.5R_{200} region of our clusters with the Multiband Imaging Photometer for *Spitzer* (MIPS; Rieke et al. (2004)). For A2255, A117, and A2026, we use medium scan mode to map out the central 30′ $\times$ 30′ region with an integration time of $\sim$80 s pixel^{-1}. For CL1633, we used the photometry mode, focused on the central 5′ $\times$ 5′, reaching an integration time of $\sim$570 s pixel^{-1}.

Estimated by the SENS-PET tool on the Spitzer website, these observations achieved a 3σ sensitivity of 0.24 mJy at 24 μm for A2255 with a low level of background and 0.42 mJy for A117 with a medium to high background. The estimated 3σ sensitivities of A2026 and CL1633 are 0.45 and 0.54 mJy, respectively.

5.2.2 Sample Selection

5.2.2.1 Cluster Membership

With nearly complete spectroscopic data in the cluster fields, we can select cluster members by their redshifts. However, even with redshift selection, we still

cannot eliminate interloper galaxies whose redshifts happen to fall within the cluster redshift range but are foreground/background sources not bound to the cluster. To minimize the contamination from interpolers, we follow the strategy proposed by den Hartog & Katgert (1996), combining the redshift and spatial information of the galaxies together to identify cluster members. We include additional spectroscopically-identified galaxies from SDSS and NED to have as complete a membership list as possible.

First, we estimate the bi-weighted mean and dispersion of the cluster peak in the redshift histogram. We only include the galaxies with velocities falling within the $\pm 3\sigma$ range of the cluster mean. Using these galaxies, we calculate the cluster mass profile and the maximum allowed line-of-sight velocity as a function of the projected distance from the cluster center, with assumed dynamic properties of cluster galaxies. We then exclude the galaxies with line-of-sight velocity larger than the maximum projected value. We repeat these two processes until the results converge and the number of cluster members remains constant. We use the most stringent maximum velocity criterion given by den Hartog & Katgert (1996), which assumes that all the cluster galaxies are either in circular or radial orbits.

The results of these member-selecting criteria are shown in Fig. 5.2. This plot shows the individual galaxy velocities (V) relative to the cluster mean (V_0) at each galaxy's projected radius. The maximum line-of-sight velocities at these radii are shown as dashed lines. A117, A2255, and A2026 have clear loci of cluster galaxies well enclosed by this maximum line-of-sight velocity profile. CL1633 is less clear in terms of its members. While we are hesitant to officially label this a definite cluster, we will include it in our analysis anyway, understanding that its identity as a cluster is questionable.

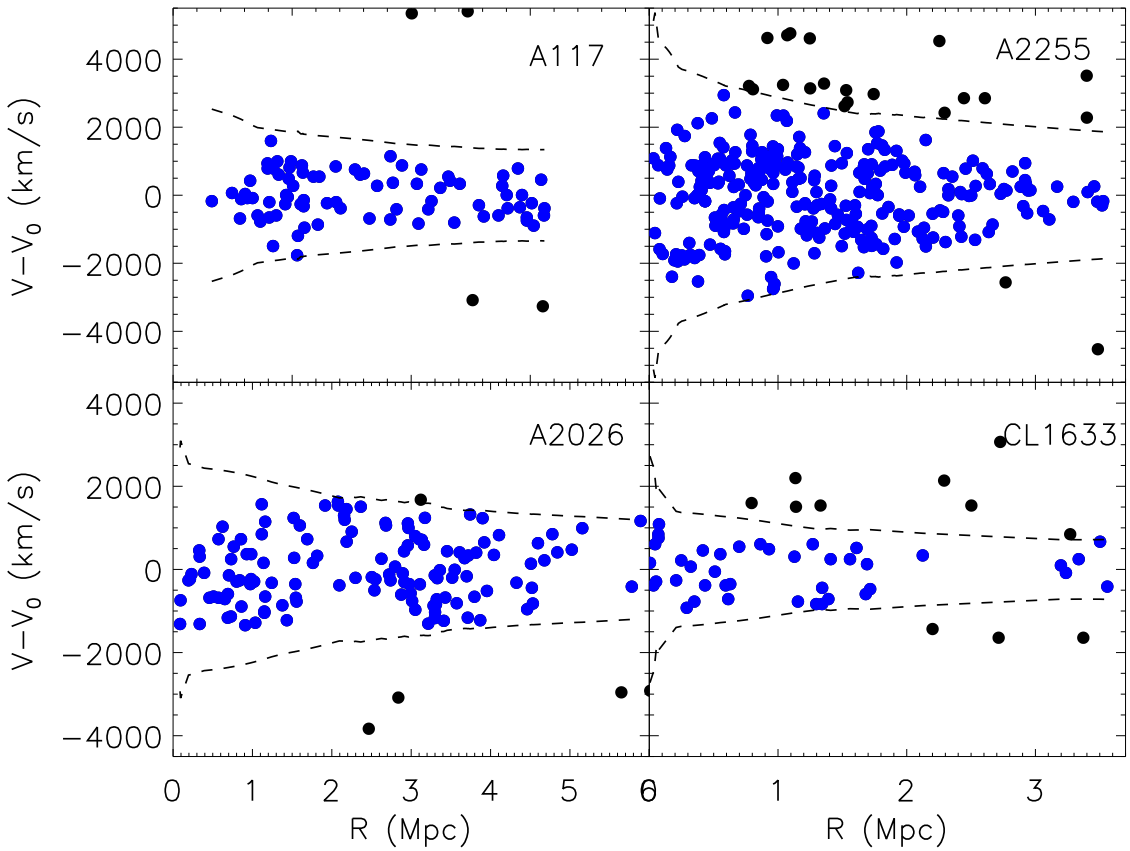

Figure 5.2 Galaxy velocity (V) relative to the cluster mean (V_0) with respect to projected radius. We used the method of den Hartog & Katgert (1996) to identify cluster members. They estimate the maximum velocity a galaxy can have at a given projected distance from the center of the cluster and still be bound to the cluster (dashed lines). If a galaxy's maximum infall and circular velocities fall within these lines, it is considered a cluster member (blue filled circles).

5.2.2.2 AGN

Since we are trying to study star forming galaxies in these clusters, we need to identify and remove galaxies with AGNs dominating the optical and/or IR output. For this purpose, we use our high-resolution spectra to construct BPT diagrams (Baldwin et al., 1981), which identify AGN by comparing the emission line ratios [O III]5007$\AA$/Hβ to [N II]6583$\AA$/Hα (Figure 5.3). We compare our galaxies to the star formation/AGN limits found by Kewley et al. (2001; dotted curve) and Kauffmann et al. (2003; dashed curve; red filled circles), though the latter is typically considered more robust. (Dotted lines separate the typical AGN types into Seyferts and LINERs according to Kauffmann et al. (2003).) Few galaxies in each cluster have detections for all four emission lines, and of those that do, only one (in A2255) is sufficiently far from the Kauffmann et al. (2003) line to be identified as an AGN (and subsequently removed from our star-forming galaxy sample). There are others in the AGN-defined region, but these are so close to the star-formation region that we suspect they are likely to be dominated by star formation even though there appears to be an AGN present.

5.2.2.3 Coverage

For the rest of our analysis, we only include galaxies with both 24 μm coverage and our own spectroscopy. While the additional SDSS and NED sources were useful for identifying cluster members, we do not know the selection criteria for these sources. As such, it is not beneficial to use them further in our analysis.

We discovered previously (Tyler et al., 2013) that galaxies only detected at 24 μm tend to be passive. Whether the IR emission is from an old stellar population, low-luminosity AGNs, or recently-quenched star formation, the majority of 24 μm-only emitters are not currently forming stars. Only galaxies detected in Hα alone or Hα and 24 μm are considered star-forming for all of our clusters except

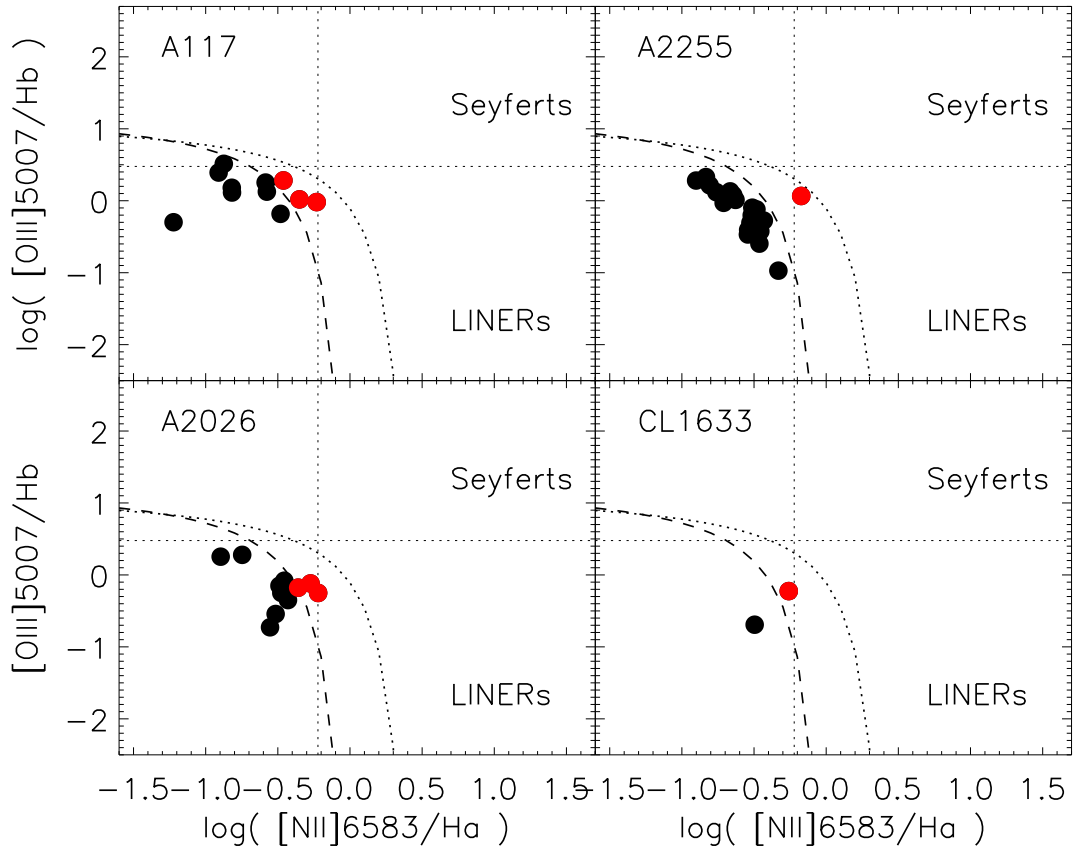

Figure 5.3 Baldwin et al. (1981) (BPT) diagram for galaxies that have detections for all four emission lines. The dotted and dashed curves delineate AGN and star-forming galaxies as per Kewley et al. (2001) and Kauffmann et al. (2003), respectively. We use the more robust latter definition, though only one galaxy (in A2255) is sufficiently far from the boundary that it can be assumed to be dominated by an AGN and was removed from the star-forming population. The other galaxies beyond the Kauffmann star formation/AGN line (red filled circles) are close enough that they likely still have a significant star-forming component.

for CL1633. The 24 μm detection limit for this cluster is high enough (due to its distance) that the IR emission for any detected galaxy could not be entirely from old stars but is likely to be powered by star formation.

With the given criteria above, the total number of galaxies belonging to each cluster are as follows: 79 members for A117, 284 for A2255, 130 for A2026, and 41 for CL1633. The number of galaxies with both 24 μm and Hectospec/IMACS coverage is 74, 87, 59, and 13, respectively, while of those, the number currently forming stars is 34, 31, 28, and 4, respectively.

5.3 Results

We calculated SFRs using the conversions described in Calzetti et al. (2010). For galaxies without 24 μm detections but with Hα emission, we use the same conversions but simply excluded the IR contribution. Because we are not correcting for absorption, the SFRs for these Hα-only galaxies is only a lower limit. All SFRs have been evolved to the present day as per Le Floc'h et al. (2005).

First, we looked at the overall distribution of the star-forming galaxies in terms of projected radius from the center of the clusters. This is shown in Figure 5.4. All galaxies with spectroscopic and IR coverage are shown in black bins while the star-forming galaxies are shown in blue hashed bins. All clusters show a reasonably constant number of star-forming galaxies from the core to the outskirts (though little can be said of CL1633, as it has few galaxy members). Since we are looking at projected radii, this means that most of the star-forming galaxies preferentially exist outside the dense cores of the clusters (Tyler et al., 2013). Additionally, the decreasing number of galaxies overall toward the outer regions of the clusters indicates a sharp increase in the fraction of star-forming galaxies with increasing radius. This increase, as well as the absence of large numbers

of star-forming galaxies in the core, has been found in many previous studies of dense clusters (e.g., Bai et al. 2009; Edwards & Fadda 2011) and is indicative of the quenching mechanism(s) that dominate in these regions.

Luminosity functions (or, in this case, SFR functions) are important for probing the distribution of star-forming galaxies in terms of their activity. Figure 5.5 shows the SFR functions for each of our XUCs. Blue open stars indicate galaxies detected in Hα but not at 24 μm, green circles are galaxies detected with both, and black filled circles indicate all star-forming galaxies. (The red triangle in CL1633 is one galaxy with 24μm emission but no Hα. As mentioned earlier, this cluster is distant enough that the 24 μm emission is too high to only be from an old stellar populations.) The brown dashed line is the 24 μm detection limit, which should be higher than the Hα detection limit in all clusters (except perhaps CL1633). The grey curve is the composite cluster Schechter function fit for Coma and A3266 from Bai et al. (2009), normalized to each cluster using χ^2 minimization for bins completely above the detection limit. A2255 and A2026 are fit reasonably well with the composite function, while A117 is much steeper. It also does not have any galaxies forming stars above $\sim$1 $M_\odot$ yr^{-1}. This could be indicative of quenching of massive star-forming galaxies, though if this is the case, it is strange that the faint end is so much steeper than that for massive clusters.

To observe how the cluster environment itself affects star-forming galaxies, we need to compare them with similar galaxies in the field. In Figure 5.6, we plot the total SFR against the stellar mass for galaxies in each cluster. Star formation detected by Hα only is shown as blue stars, while galaxies with both 24 μm and Hα emission are black filled circles. The vertical dotted lines are our stellar mass limits, estimated using the r-mag limit and mass functions. The dashed line is the mass–SFR relation for field galaxies from Brinchmann et al. (2004), linearized

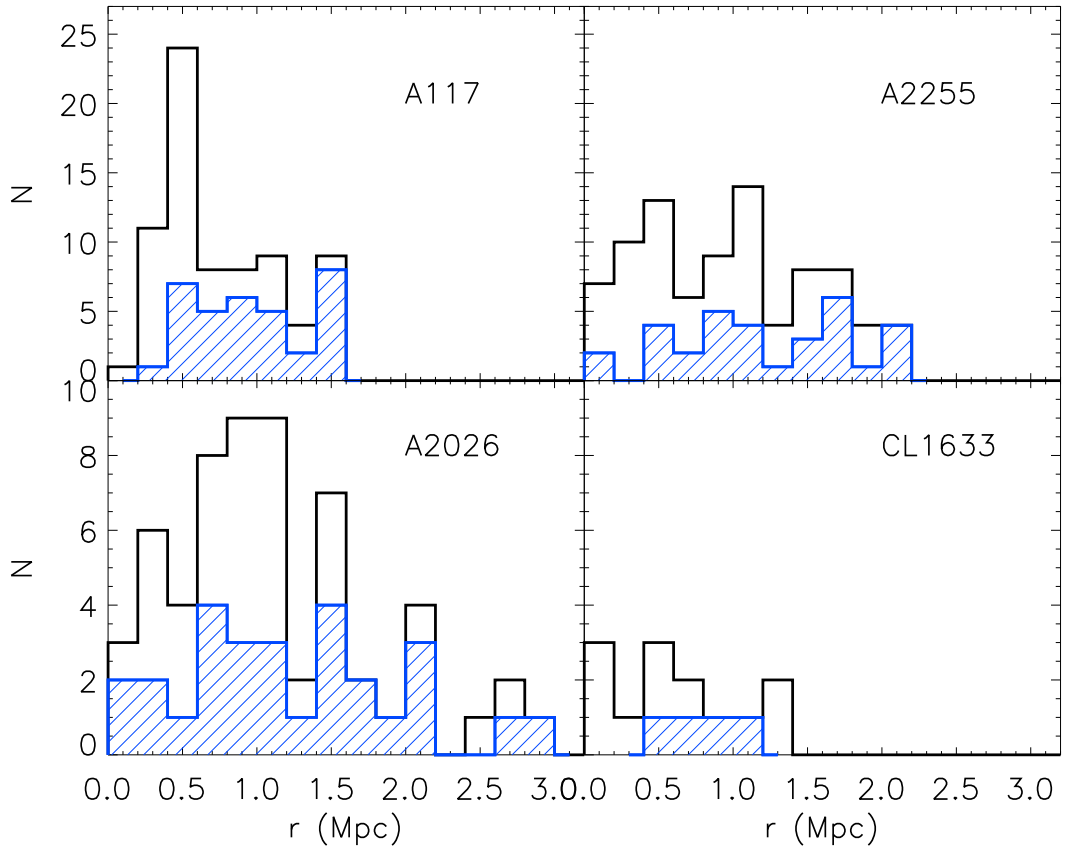

Figure 5.4 Histograms for all cluster members (black solid lines) and star-forming cluster members (blue hashed bins) with respect to projected radius. As has been found in other clusters, the fraction of star-forming galaxies tends to increase with increasing projected radius. Also, the number of star-forming galaxies remains fairly constant from the central to outer regions. Tyler et al. (2013) showed that such a distribution means the star-forming galaxies preferentially exist outside of the core of the cluster (r $\lesssim$ 1 Mpc), providing further evidence of the densest regions' ability to efficiently quench star formation.

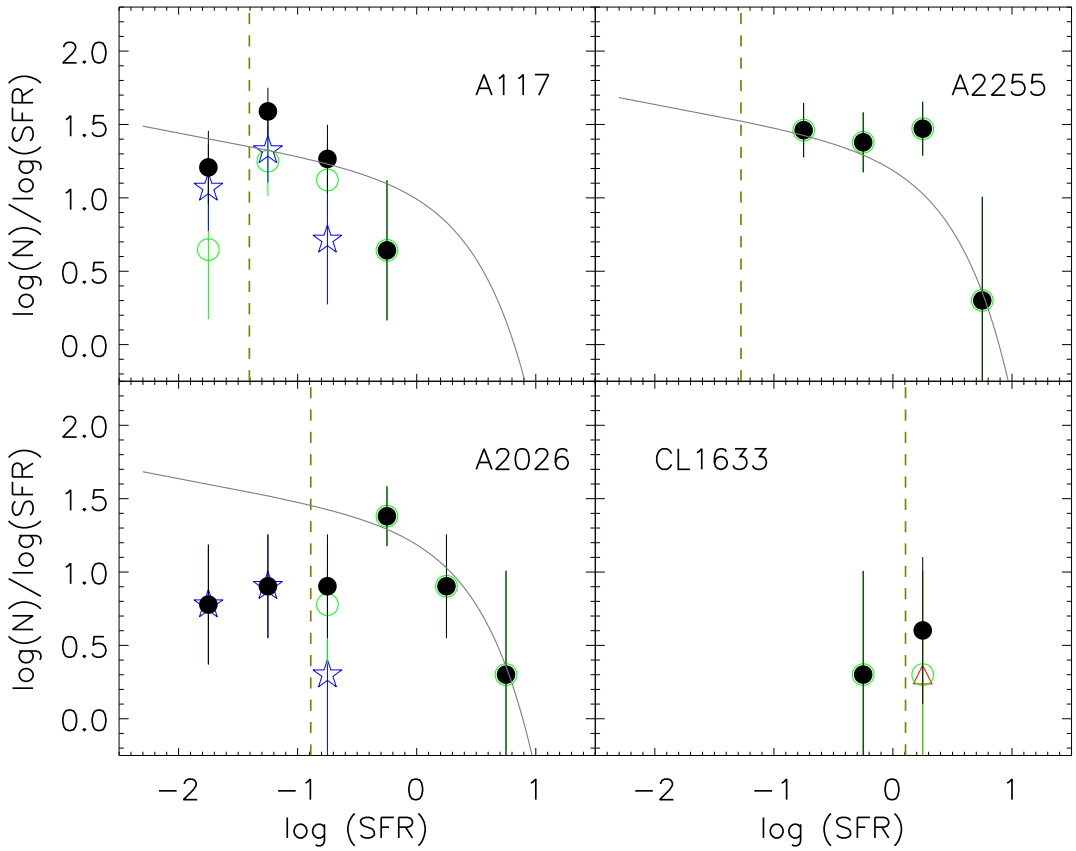

Figure 5.5 SFR functions for galaxies of all four clusters. Blue open stars indicate galaxies detected at Hα but not 24 μm, green open circles are galaxies detected at both Hα and 24μm, and black filled circles indicate the total SFR. The one red triangle point is for 24 μm-only galaxies that are likely forming stars. The brown dashed line shows the 24 μm detection limit for each cluster. All SFRs have been evolved to the present day as per Le Floc'h et al. (2005).

and normalized as by Tyler et al. (2013; see Chapter 4). A2255 and A2026 have a significant fraction of star-forming galaxies reminiscent of the field, while A117's star-forming galaxies have lower SFRs than what would be expected from the field. This could explain why the SFR function of A117 is lacking in high-star-forming galaxies and does not have the same shape as other clusters: the star formation in A117 galaxies has already been significantly suppressed.

A better visualization of this is shown in Figure 5.7. The solid black curve is a histogram of the field distribution for galaxies with $9.0 \lesssim \log(M_*/M_\odot) \lesssim 10.5$. (Above this limit, the field mass-SFR relation deviates drastically from the linear relation, making a comparison with the field at high masses difficult.) The blue histograms show the distribution of cluster star-forming galaxies around the field relation shown in the previous figure but only for galaxies above each cluster's specific mass limit and normalized to the number of galaxies included in the histogram. A2026 most resembles the field distribution except for the Hα-only galaxies, which have not been corrected for dust extinction and so could fall closer to the field relation than what is shown. A2255 is similar to the field, though it has a population of galaxies with SFRs higher than expected. A117, however, consists of star-forming galaxies far below the field; in fact, it is quite reminiscent of Coma's population of anemic galaxies (Tyler et al., 2013).

Given the low numbers of star-forming galaxies in these clusters, combining them would give us a clearer picture of star-forming galaxies in XUCs. Figure 5.8 shows the same plots as the last two except it includes all star-forming galaxies in all four clusters (again, only galaxies above each cluster's mass limit). The top two plots include the uncorrected Hα-only SFR that we have been using up until this point. The bottom two plots are the same except the SFRs for the Hα-only galaxies are calculated using the 24 μm detection limit for each cluster, which

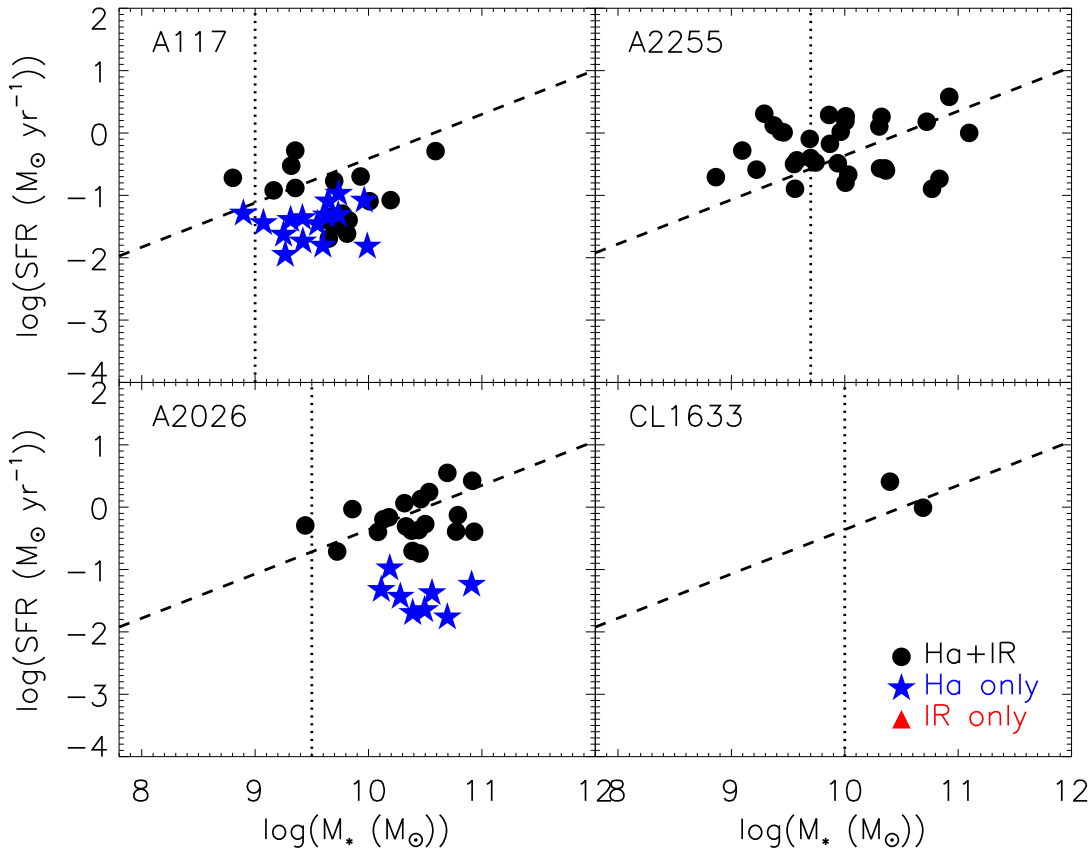

Figure 5.6 Total SFR vs. stellar mass for galaxies in all four clusters. Blue filled stars indicate galaxies detected at Hα but not 24μm and black filled circles signify galaxies detected at both Hα and 24μm. The vertical dotted line is the estimated stellar mass limit given the r-band magnitude limit; the dashed line represents the field M_*–SFR relation as per Tyler et al. (2013) and Brinchmann et al. (2004). Most of the star-forming galaxies in A2255 and A2026 echo the field relation, but A117's galaxies lie mostly below what is expected for the field.

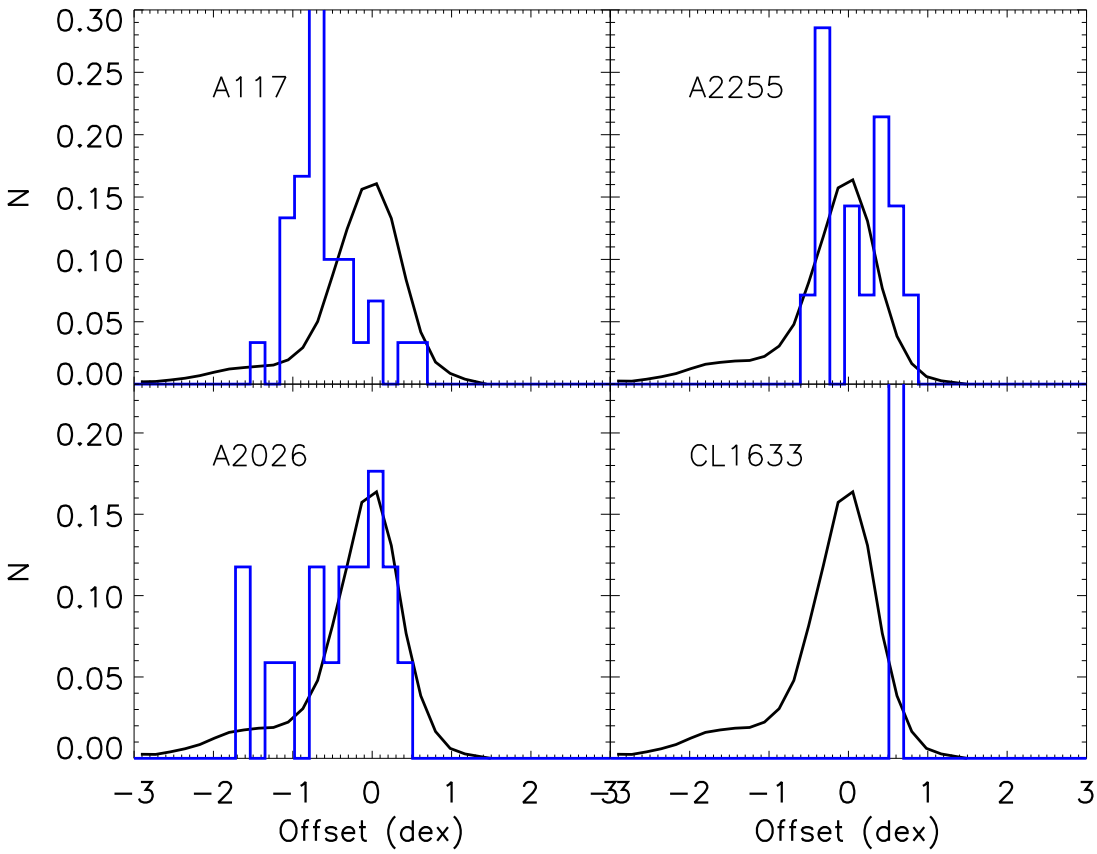

Figure 5.7 Offsets between all cluster star-forming galaxies and the field relation shown in the previous figure. The black solid line is the field distribution (Brinchmann et al., 2004), while the blue solid lines are histograms of the offsets for each cluster.

gives us upper limits on the SFRs. In both plots, there is a significant population of galaxies forming stars at levels lower than expected for the field (so-called "anemic" galaxies).

5.4 Discussion

In our previous paper (Tyler et al. 2013; Chapter 4), we concluded that the mass-SFR distributions for A2029 and Coma were indicative of the clusters' merger history. Because the star-forming galaxy population in A2029 has a similar mass–SFR relation to the field, its star-forming galaxies were most likely accreted recently and the dense cluster environment had not yet begun to quench their star formation significantly. The field-like distribution of star-forming galaxies in A2029 is not indicative of a lack of quenching activity over the life of the cluster, though: the fraction of star-forming galaxies is 27±3%—close to the upper limit for clusters (30%) but lower than field values, which are typically $> 50\%$ (e.g., Balogh et al. 1999; Rasmussen et al. 2012). On the other hand, Coma had a large number of galaxies with SFRs below what was expected for field galaxies of similar mass, indicating that some of the star-forming galaxies had joined the cluster more than a couple Gyr ago (and had time for their star formation to be suppressed by the cluster environment) and/or the galaxies had been "pre-processed" to some extent in groups before entering the cluster.

The main motivation for our study of XUCs, however, was to see if their differently-configured ICMs resulted in a difference in the properties of their star-forming members. They may indeed differ from classical X-ray luminous clusters, with fractions of star-forming galaxies close to that in the field: 46±10% (A117), 36±7% (A2255), 47±11% (A2026), 31±18% (CL1633). However, our other results point more toward these "XUCs" as being like normal clusters. The ra-

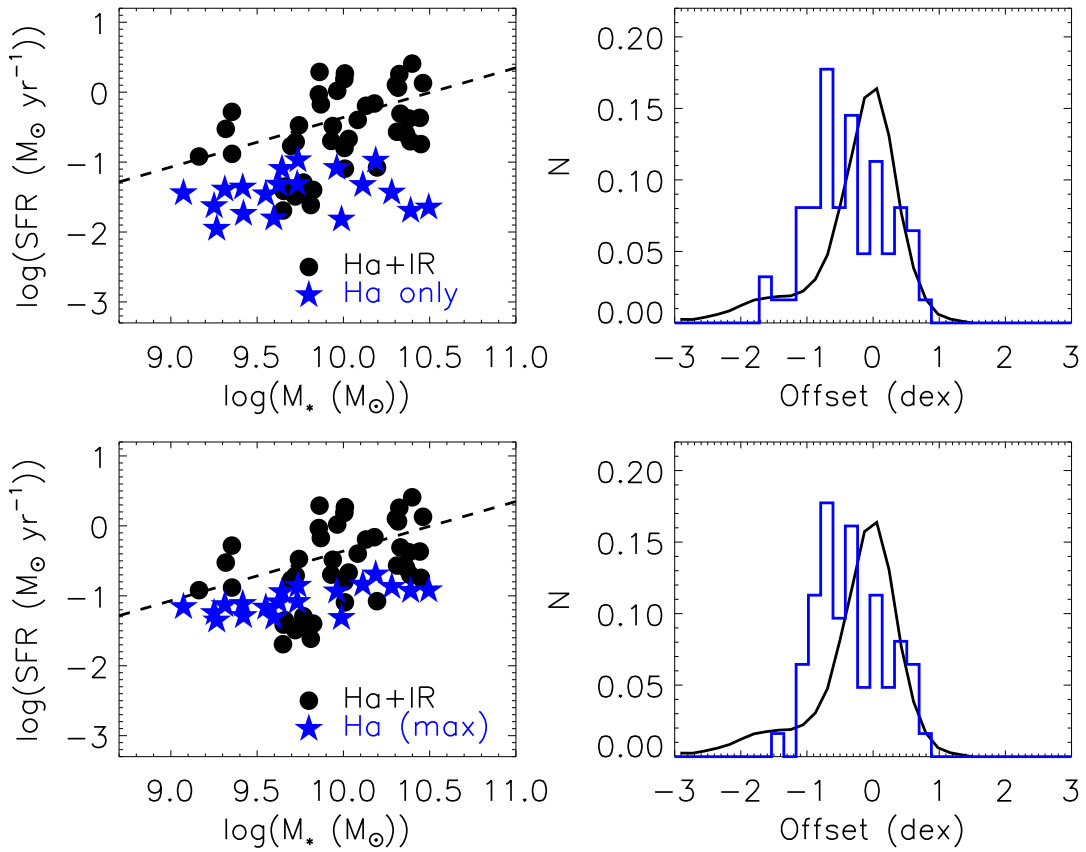

Figure 5.8 Same as the previous two plots but for all star-forming galaxies for all four XUCs (but only including galaxies above the mass limit for each cluster). The top two plots show the uncorrected Hα emission (for galaxies not detected at 24 μm). The bottom two plots are the same except that the Hα-only galaxy SFRs are calculated using the 24 μm detection limit, which gives us an upper limit. In both sets of plots, there is a population of low-star-forming galaxies, similar to what has been found in other clusters like Coma (Tyler et al., 2013).

dial distribution of star-forming galaxies and SFR functions are comparable to what has been found for X-ray luminous clusters like Coma and A2029 (Tyler et al., 2013). Similarly, the distribution of star-forming cluster galaxies around the mass–SFR relation is reminiscent of these two massive clusters. A117 has a significant population of anemic galaxies with a distribution similar to that of Coma, while A2026, on the other hand, is almost identical to the field and A2029 (Tyler et al., 2013). Only A2255 shows a vastly different mass–SFR distribution as compared to the field and all the other clusters we have studied.

From the comparison of the XUCs with the normal ones, it is possible that the X-ray plasma does affect star-forming galaxies in normal clusters (as shown by the lack of suppressed galaxies in XUC A2026), but this correlation may be undermined by the absence of anemic galaxies in the X-ray luminous cluster A2029. It also appears that XUCs like A117 have had their star formation suppressed prior to entering the cluster environment. A117 is evidence for the group environment having a significant effect on star-forming galaxies, also known as preprocessing (e.g., Zabludoff & Mulchaey 1998; Wilman et al. 2009; Just et al. 2010). It is interesting to note that A117 has one of the highest fractions of star-forming galaxies of all the XUCs, indicating that the star-forming galaxies are still in the process of being quenched (i.e., few galaxies have completely ceased forming stars). The XUC results indicate that while some preprocessing does occur in groups, clusters (and the ICM) are still responsible for quenching star formation in at least some cases. A2029 and A2026 are good examples of clusters whose current star-forming galaxies have not been significantly preprocessed by groups. As a result, it is apparent that both group and cluster environments are directly involved in suppressing star formation.

This remains true even if these clusters are not actually X-ray underluminous.

A triaxial cluster with the longest axis oriented along the line of sight would result in an overestimation of the velocity dispersion and, therefore, an overestimate of the cluster mass, making the cluster seem more X-ray underluminous than it really is. Additionally, A2255 has ICM masses and temperatures comparable to A2029, which is a normal X-ray emitting cluster (Molendi & De Grandi 1999; Lewis et al. 2002; Miyoshi et al. 2005; Sakelliou & Ponman 2006). If the low X-ray luminosity is not indicative of of a less-dense or a lower-temperature ICM, then these clusters may not truly be X-ray underluminous. Indeed, some of our results seem to indicate this is the case. Still, the clusters studied in this paper show signs of quenching both from the group and cluster environments, and they have varying fractions of star-forming galaxies, from normal cluster levels to the field. What is needed, at this point, is to look at these "underluminous" clusters in more detail to understand the nature of their X-ray emission and, therefore, their effects on infalling star-forming galaxies.

5.5 Conclusions

We observed four X-ray underluminous clusters with optical spectroscopy and 24 μm photometry to study how clusters with little or no apparent X-ray luminous gas affect the star formation in member galaxies. We calculated SFRs using both Hα and 24 μm and found that the fraction of star-forming galaxies in these clusters is higher than what would be expected from equally-massive, X-ray-bright clusters but on the low end of the expected range for the field. We also found that the mass–SFR distribution of these galaxies varies depending on the cluster, from a field-like distribution to a Coma-like population of anemic galaxies. This indicates that some galaxies have been "preprocessed" in groups prior to entering the cluster environment, while others clearly have not. Therefore, suppression of star

formation occurs in both groups and in clusters—one is not necessarily dominant over the other. These results hold even if, as suggested by recent studies, these clusters are not truly X-ray underluminous.

CHAPTER 6

CONCLUSIONS AND FUTURE DIRECTIONS

In this final section, we summarize our results on IR-emitting galaxies in a variety of environments and look toward further studies of these galaxies with both current and future facilities and instruments.

6.1 High-Redshift ULIRGs and HyLIRGs

Chapter 2 presented new 70 and 160μm measurements of a group of extremely luminous IR galaxies: ULIRGs and HyLIRGs at 1.5 $\lesssim$ z $\lesssim$ 3. These galaxies are very red (R-[24] $\gtrsim$ 15 mag) and bright at 24μm. Until recently, it was unknown what powers these sources, whether it be star formation, AGNs, or both, though at the time, studies suggested that AGNs began to dominate the IR output at the highest luminosities (e.g., Lutz et al. 1998; Tran et al. 2001; Veilleux et al. 2002; Pearson 2005; Gruppioni et al. 2005; Brand et al. 2006; Donley et al. 2010). Our measurements helped constrain L_{IR} for this class of object for the first time, showing they are indeed U/HyLIRGs.

Additionally, we fit templates of canonical starbursts and AGNs to our SEDs, which consisted of all three MIPS bands and IRS spectra. While the MIPS bands probed the blue side of the IR peak, the redshifts of the sources allowed the spectra to cover the silicate absorption feature at 9.7μm and the surrounding polycyclic aromatic hydrocarbon (PAH) emission lines, indicative of strong star formation. Our data was sufficient to deduce the dominant mechanism for the IR output of these galaxies: AGN. Only three of our 11 sources were matched to galaxy templates with significant amounts of star formation, confirming previous findings (Houck et al. 2005; Yan et al.2005; Brand et al. 2007; Melbourne et al.

2012).

The role of U/HyLIRGs in galaxy evolution remains a mystery, however. Both observations and theoretical models of IR-luminous galaxies suggest they are the result of major mergers, which would explain the high levels of star formation and obscuring dust (e.g., Mihos & Hernquist 1996; Narayanan et al. 2010; Donley et al. 2010; Kartaltepe et al. 2010; Nardini et al. 2010). This activity could funnel material to the nuclei of the galaxies, in effect "turning on" the AGNs and subsequently quenching the ongoing star formation (e.g., Sanders et al. 1988; Hopkins et al. 2006). But observations of high-redshift ULIRGs does not always support this view (Sturm et al. 2010; Draper et al. 2012; Melbourne et al. 2012). Evidence is emerging that, at redshifts of $\sim$1 or higher, the dominant form of luminous infrared galaxy is extended, with vigorous star formation over a region comparable with local galaxy disks (Rujopakarn et al., 2011).

6.2 Star-Forming Galaxies in Groups

We then moved on to the more large-scale environments of groups in Chapter 3. It has been known for a long time that clusters affect the properties of their member galaxies, but only a small fraction of galaxies reside in clusters. The largest fraction of galaxies live in groups, which are regions of intermediate density. We set about trying to answer the question of whether galactic star formation is mostly quenched in the group environment or if clusters are most responsible for the "red and dead" galaxy members. We used deep 24μm observations to identify star-forming galaxies since the SFRs probed at these redshifts in the MIR (SFR $\gtrsim$ 2.7 $M_\odot$ yr^{-1} at $0.3 \lesssim z \lesssim 0.55$) are high enough that any unobscured star formation should be negligible.

Previous studies of the same groups had shown that they have higher frac-

tions of early-type galaxies than the field, as expected (Wilman et al., 2009). Despite this, the overall star-formation properties of the group galaxies seemed to echo that of the field. For a galaxy of a given mass and morphology, the group and field galaxies were comparable in terms of their SFR. What makes the groups different, then, is their much higher fraction of early-type galaxies, not necessarily the amount of star formation ocurring in the individual galaxies of a given mass and morphology. Indeed, we even found evidence of star formation in both S0 and elliptical group galaxies, something not often seen in the field because these early-types are not as common.

Our findings show that groups are indeed intermediate between the field and clusters, just not perhaps in the expected manner. It appears that some "pre-processing" does occur the groups—spirals changing to S0s while the galaxies grow in mass—but the overall star formation of individual galaxies is not as readily affected by the group environment as are mass and morphology.

6.3 Star-Forming Galaxies in Clusters

If star formation is not greatly affected in groups—at least, at the SFRs probed in the previous chapter—then the cluster environment must be the main instigator of star-formation quenching. We focus our attention on clusters for Chapters 4 and 5.

First, we focused on the massive clusters A2029 and Coma, using a variety of star-formation indicators (MIR, Hα, FUV) to probe both obscured and unobscured star formation down to very low levels (SFR $\sim$ 0.03 $M_\odot$ yr^{-1}). We found that the SFR function of A2029 is comparable to the composite massive cluster luminosity function of Bai et al. (2009), which includes Coma. However, when we compared the star-forming galaxies to the mass–SFR relation of the field,

we discovered that while Coma has a significant population of low-star-forming galaxies given their mass (as expected for an environment that quenches star formation), A2029 looked almost identical to the field. This does not necessarily mean that A2029 is not suppressing star formation. A2029 may have accreted field and/or group galaxies fairly recently since galaxies that previously entered the cluster have been there long enough to have their star formation quenched but the newest members have not (and are still behaving like normal field galaxies). Coma, on the other hand, accreted a significant fraction of galaxies previously (and those are in the process of having their star formation suppressed), the galaxies underwent significant quenching in the group environment prior to being accreted into the cluster, or a combination of the two effects.

It should be noted that we focused on galaxies with $9 \lesssim \log(M_*/M_\odot) \lesssim 10.5$. Given our optical photometry limit, we were unable to study galaxies below this limit, where quenching mechanisms such as ram-pressure stripping and starvation/strangulation are more efficient (Boselli & Gavazzi 2006 and references therein). The cluster environment could be having a much stronger effect on these low-mass galaxies than the ones we studied.

We also noted, interestingly, that a subset of the galaxies detected at 24μm and/or FUV (not Hα) have colors, morphologies, and spectra like passive early-types. Via the method of Temi et al. (2009), we found that the IR emission from most of these galaxies is likely to be from dust around old stars rather than star formation. A handful were detected in X-rays, which may explain some of the IR or FUV emission through the contributions of AGN, but most seem to be completely passive. This may seem contradictory to our group result, where we found some early-type galaxies with IR emission most likely from star formation. However, the SFRs probed in the group observations are about an order of magnitude

higher than those in A2029. The IR emission from the group early-types is too high to be only from old stars.

The dominant mechanisms for quenching star formation in groups and clusters are different. Group galaxies are more affected by mergers and galaxy-galaxy interactions than ram-pressure stripping or starvation/strangulation. Cluster galaxies are moving too quickly for mergers to occur on a frequent basis, and while groups can have enough intra-group medium to strip gas from disk galaxies, it is much less efficient. Our study of A2029 and Coma was unable to identify the dominant mechanism for suppressing star formation in these clusters.

This brings us to Chapter 5, where we observe four clusters previously identified as being X-ray underluminous in a similar manner as A2029 and Coma to see how much of an effect the ICM has on star-forming galaxies. Ram-pressure stripping, in particular, needs dense, hot gas to strip material from galaxies; the same goes for starvation/strangulation, though it does not require as high a density as ram-pressure stripping (Boselli & Gavazzi 2006). The fraction of star-forming galaxies in the XUCs is between that for massive, X-ray-bright clusters and the field, and the mass–SFR distributions vary from cluster to cluster. This indicates that groups preprocess some galaxies before they enter the cluster environment, though the clusters clearly suppress star formation as well. Neither environment seems to dominate in terms of quenching star formation—both are required to turn blue, disky field galaxies into the red, S0-type galaxies so prominent in groups and clusters. It is possible, though, that these clusters have properties that make them appear underluminous in X-rays when, in reality, are not. More study is required to understand what makes these clusters appear different from normal X-ray emitting clusters and, therefore, how they can affect star-forming member galaxies.

In summary, it is clear that dense environments affect many properties of galaxies: color, morphology, mass, SFR. Groups clearly change the morphologies of their member galaxies, as found by both our study and others', but we found the fraction and types of star-forming galaxies to be intermediate between the field and cluster environments. A2029, Coma, and the XUCs all indicate that groups can preprocess galaxies in some cases, but in others, the cluster environment is most responsible for quenching star formation.

6.4 Future Directions

Some future work has already been accomplished since the research in Chapter 2. Our study of U/HyLIRGs was limited to the Wien side of the FIR peak, resulting in our inability to completely constrain L_{IR}. The Spectral and Photometric Imaging Receiver (SPIRE) on the *Herschel Space Telescope* covers three wavelength bands from 250μm to 500μm—perfectly situated beyond the IR peak for luminous IR galaxies at $2 \lesssim z \lesssim 3$. Melbourne et al. (2012) took advantage of SPIRE observations of the Boötes field to constrain the FIR peak for their sample of optically faint ULIRGs. They observed some of the U/HyLIRGs we did and found that our L_{IR} estimations were within 20% of theirs, and they also found a combination of AGNs and star-forming sources.

Beyond *Herschel*, several new observatories will aid in further understanding both these hugely energetic sources and more normal star-forming galaxies in groups and clusters. The *James Webb Space Telescope* (JWST) will provide imaging and spectroscopic coverage in nearly the same wavelength regime as *Spitzer* (5–28μm), and the Atacama Large Millimeter/Sub-mm Array will soon cover 3 mm to 300μm. For U/HyLIRGs, these telescopes will cover both the Wien side of the IR bump and the Rayleigh-Jeans tail, allowing us to identify and study more

U/HyLIRGs in even more detail. Additionally, the Giant Magellan Telescope (GMT) could provide clearer images of U/HyLIRG morphologies to help us understand how these objects relate to normal galaxy formation and evolution.

These up-and-coming attractions also have a profound impact on group and cluster studies. A multi-object spectrograph on the GMT would provide more complete cluster membership lists, down to even lower masses, as well as higher signal-to-noise spectra for identifying emission lines. The Large Synoptic Survey Telescope (LSST), with its deep optical photometry ($>$ 24 mag in SDSS filters for single images and 27 mag for stacked) will also help reveal the lower-mass group and cluster members. ALMA, at longer wavelengths, could be used to confirm the IR-/FUV-detected early-type galaxies in clusters are truly passive. And JWST will continue the IR legacy left by *Spitzer* and *Herschel*—leading the way toward new discoveries and a more complete understanding of how the galaxies of the past created the galaxies of today.

Appendix A

Early-Type Galaxies with 24μm Emission in Groups

Our initial coordinate matching of MIPS 24μm sources to their optical counterparts resulted in 11 early-type (E or S0) galaxies with possible IR emission: seven group and four field galaxies (Table 1). Given the density of galaxies in our fields—and how surprising it was to find E/S0 galaxies with possible star formation—we checked each match individually to confirm whether or not the 24μm emission was coming from the early-type galaxy or if there were a possibility that a close companion was the actual source of the emission. Here, we provide a short description of both the optical and 24μm sources, as well as HST ACS postage stamps of each galaxy (Figure A.1) with error circles matched to the 24μm emission at 3 arcsec (matching radius) and 6 arcsec (radius of MIPS PSF FWHM).

PATCH 1447 ID 40969 (Figure A.1a): While classified as an "E pec" galaxy (elliptical with a possible interaction from a companion), there are no sources within the 3 arcsec matching radius, and the 24μm emission is clearly right on top of the elliptical (the emission peaks less than 1 arcsec from the center of the elliptical). The 24μm emission is definitely coming from the early-type galaxy with no other obvious source.

PATCH 1447 ID 020364 (Figure A.1b): This elliptical galaxy has three small neighbors, though only two are within the 3 arcsec matching radius (the others are slightly farther out). The 24μm source is closer to the nearest neighbor and close to the edge of the 3 arcsec radius. It is possible that the IR emission is coming from the companion galaxy and not the early-type, and so it is not included in our list of IR-active E/S0 galaxies.

Table A.1. Early-Type Group Galaxies Matched with IR Sources

Patch[a]	ID	RA	Dec	z	L_{TIR} (10^{10} $L_\odot$)	SFR ($M_\odot$ yr^{-1})	Group[b]	Galaxy Type	X-ray Coverage?
1447	040969	222.377813	9.511117	0.35	3.8	3.7	23	E pec	N
1447	020364	222.431575	9.232753	0.36	11	12	25	E	N
1447	041307	222.427158	9.536456	0.54	4.9	4.8	39	E pec	N
1447	111706	222.483754	8.940261	0.39	0.89	0.78	32	E	Y
1447	122388	222.355163	9.074511	0.41	0.96	0.85	0	E/S0	Y
1447	150408	222.184342	8.842967	0.32	1.7	1.5	0	E	N
1447	111547	222.470204	8.926272	0.30	1.0	0.91	0	E	Y
1447	120982	222.349458	8.990908	0.37	3.0	2.8	0	S0 pec	Y
1447	091003	222.578538	9.010039	0.40	1.1	1.0	32	S0/a	N
1447	091304	222.578025	9.030156	0.37	2.4	2.2	28	S0	N
2148	141211	327.600550	-5.681283	0.44	4.5	4.3	138	S0/E	Y

[a]Original CNOC2 patch number (Yee et al., 2000).

[b]Galaxy group to which the object belongs; a 0 value indicates a field galaxy.

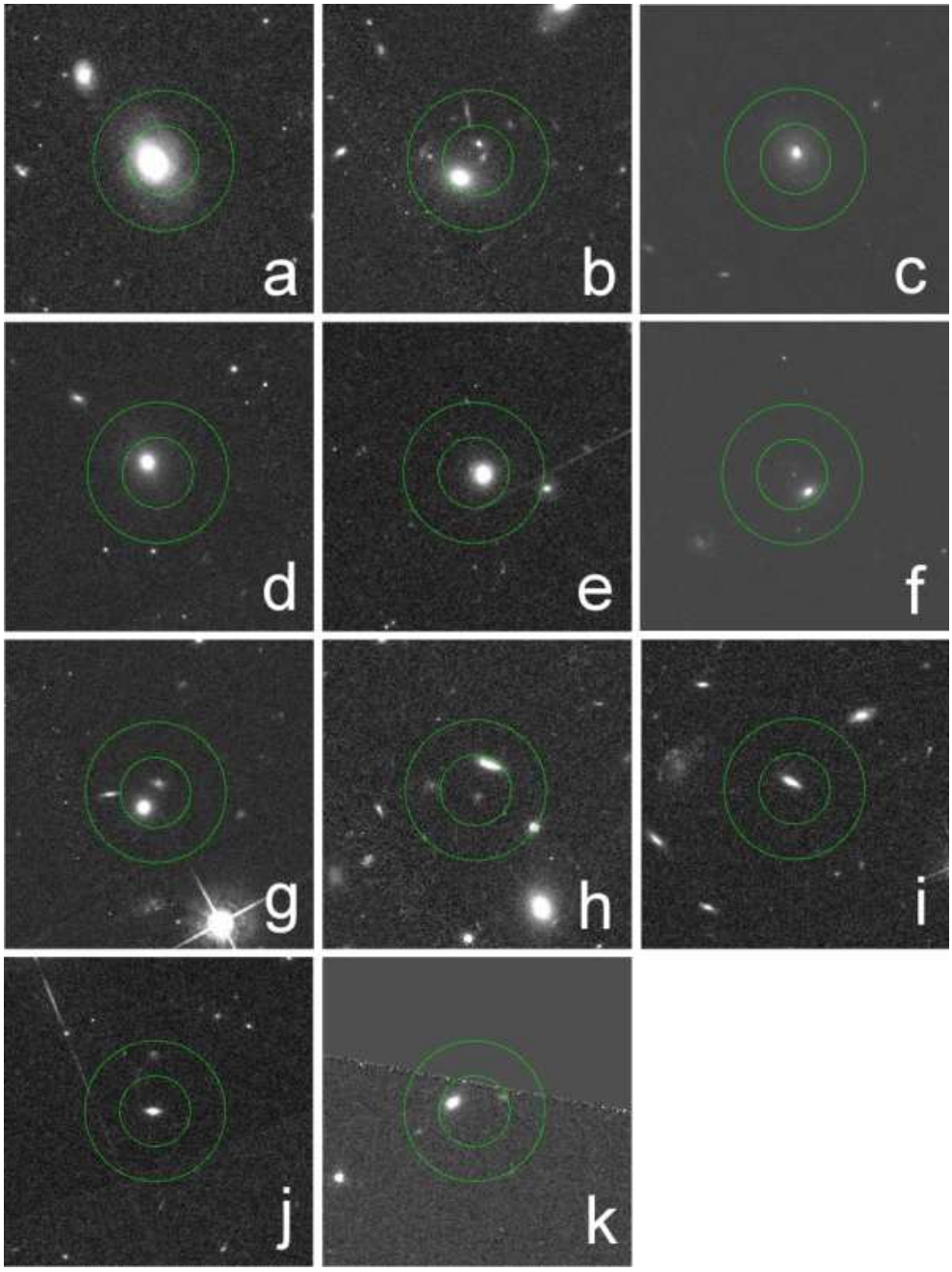

Figure A.1 HST ACS images of the 11 E/S0 galaxies matched with 24μm sources. The inner annulus has a radius of 3 arcsec, which is the length we used for matching the optical coordinates with 24μm sources. The outer annulus shows the FWHM of the MIPS PSF. The ID and patch number of the matched galaxies are as follows: (a) 1447 040969, (b) 1447 020364, (c) 1447 041307, (d) 1447 111706, (e) 1447 122388, (f) 1447 150408, (g) 1447 111547, (h) 1447 120982, (i) 1447 091003, (j) 1447 091304, (k) 2148 141211.

PATCH 1447 ID 041307 (Figure A.1c): This galaxy is another peculiar elliptical but with no galaxies within 3 arcsec. The 24μm source, while faint, is almost directly on top of the elliptical ($\sim$1 arcsec away). It is highly unlikely the IR emission is coming from another source, so we classify this galaxy as an IR-active early-type.

PATCH 1447 ID 111706 (Figure A.1d): Classified as a normal elliptical galaxy, this source has faint 24μm emission that lies almost on top of the galaxy ($\sim$1 arcsec) with no other obvious galaxies within the match radius. This object has deep X-ray coverage as well, with no detected X-ray source to account for the IR emission. We include this elliptical in our list of star-forming early-type galaxies.

PATCH 1447 ID 122388 (Figure A.1e): Other than being classified as an "E/S0," (somewhere between an elliptical and an S0 galaxy, but more closely resembling an elliptical) this galaxy's situation is almost identical to the previous one.

PATCH 1447 ID 150408 (Figure A.1f): Here is another regular elliptical galaxy with only one point-source-like neighbor within 3 arcsec. The 24μm source is well within the match radius, but it is between the nearby object and the elliptical ($\sim$2 arcsec from the elliptical). It is uncertain as to which source the 24μm emission is coming from, so we removed this galaxy from being a star-forming early-type.

PATCH 1447 ID 111547 (Figure A.1g): This is a normal elliptical galaxy with two close companions, one of which appears to be a faint irregular fully within the matching radius. The MIPS source appears extended and spans the distance between this closer neighbor and the elliptical. As with the previous galaxy, the uncertainty in the source of the 24μm emission forced us to not include this galaxy as an IR-active source.

PATCH 1447 ID 120982 (Figure A.1h): A very faint irregular galaxy barely lies within 3 arcsec of the early-type galaxy, listed as a peculiar S0. The IR source

is again between the two galaxies, and though it is slightly closer to the faint companion, the 24μm emission is well within the match radius boundary ($\sim$2 arcsec from the S0). We conservatively do not include this early-type as IR-active.

PATCH 1447 ID 091003 (Figure A.1i): This galaxy is an S0/a, meaning it closely resembles an S0 galaxy but with some Sa qualities. There are no other galaxies within 3 arcsec, and the IR source peaks $\sim$1 arcsec from the S0/a. We include this object as a star-forming early-type galaxy.

PATCH 1447 ID 091304 (Figure A.1j): This normal S0 is almost identical to the previous galaxy.

PATCH 1447 ID 141211 (Figure A.1k): As with the previous two galaxies, this S0/E (S0 galaxy somewhat similar to an elliptical) has no other companions within 3 arcsec (though there are two faint galaxies between 3.5 and 5 arcsec away). The 24μm emission is slightly offset from the galaxy ($\sim$1 arcsec) but within the match radius. A very faint galaxy lies $\sim$1.5 arcsec from the 24μm position. While it seems likely that the IR emission is coming from the S0 galaxy, we took a conservative stance and do not classify this galaxy as IR-active.

In Figure A.2, we plot rest-frame optical and IR SEDS for the six E/S0 galaxies that have confirmed IR emission. The stellar outputs of these galaxies may be dominated by a relatively old population. Therefore, we fit Rieke et al. (2009) average star-forming galaxy templates to the SEDs in two distinct segments. First, we found the average template with the closest L_{TIR} to each galaxy and fit the 24μm data point to the template (red spectrum). For the normal stellar emission, we used optical and near-IR photometry to find the best-fit (χ^2) average star-forming template (orange spectrum). Except for the first two galaxies, we see a clear stellar bump from normal stars and then increasing luminosity of the mid-IR dust emission beyond 7μm, indicative of a normal star-forming galaxy

and not an AGN. In all cases, the SED is consistent with the expectation for star formation. There are two cases where 1) there is IRAC data; and 2) a detection of the aromatic emission at 8μm is predicted from the combination of IRAC bands 1–3 and the MIPS 24μm flux density. The expected 8μm excess is seen for both galaxies.

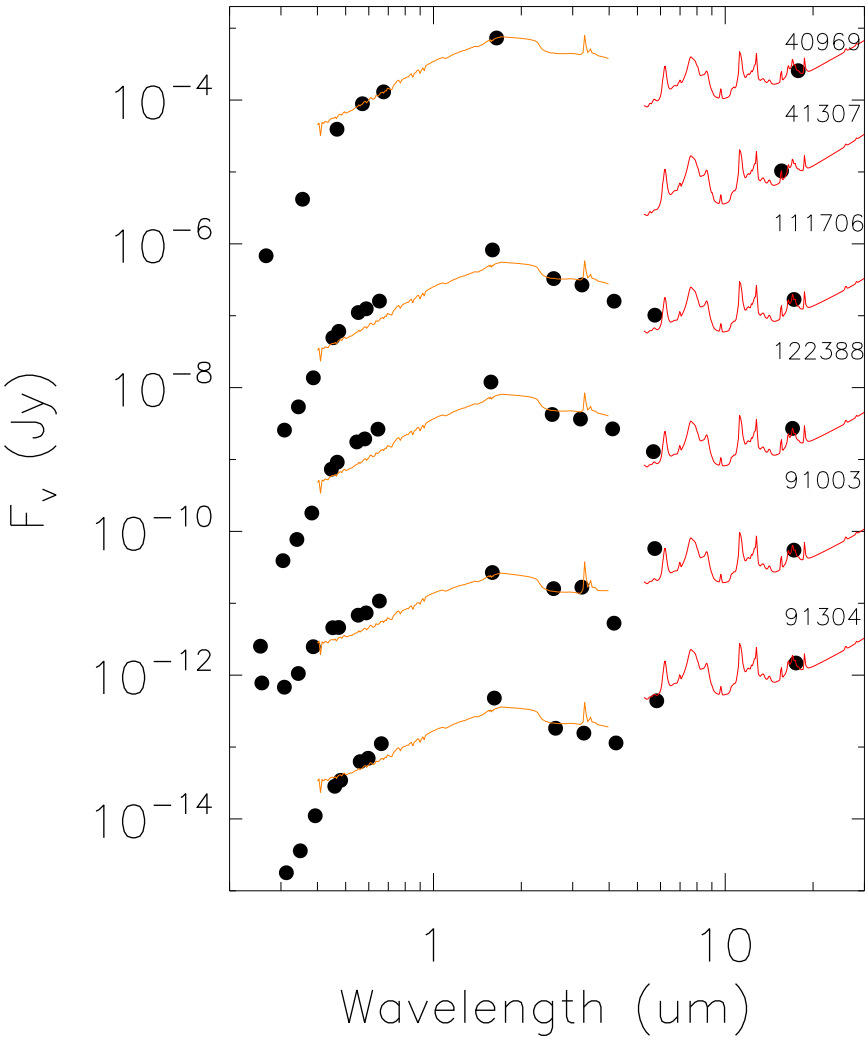

Figure A.2 Optical and IR SEDs (rest-frame) for all six star-forming E/S0 galaxies, identified by their GEEC ID and fit by different segments of the Rieke et al. (2009) average star-forming galaxy templates. Each galaxy was matched to the average template with the closest L_{TIR} and fit to the 24μm data point (red spectra). The orange spectra are best-fit (χ^2) average star-forming templates for the optical/near-IR photometry; while these fits are not very accurate, they are sufficient for our purposes. Except for 40969 and 41307, all galaxies have enough photometric points to indicate the presence of a stellar bump and mid-IR dust emission similar to normal star-forming galaxies.

References

Abell, G. O. 1958, ApJS, 3, 211

Abell, G. O. 1974, in *Stars and Stellar Systems*, vol. 9, ed. A. and M. Sandage and J. Kristian (Chicago: University of Chicago Press)

Abraham, R. G., Valdes, F., Yee, H. K. C., & van den Bergh, S. 1994, ApJ, 432, 75

Abraham, R. G., van den Bergh, S., Glazebrook, K., Ellis, R. S., Santiago, B. X., Surma, P., & Griffiths, R. E. 1996, ApJS, 107, 1

Agüerri, J. A., Méndez-Abreu, J., & Corsini, E. M. 2009, A&A, 495, 491

Andreon, S., Willis, J., Quintana, H., Valtchanov, I., Pierre, M., & Pacaud, F. 2004, MNRAS, 353, 353

Armus, L., Heckman, T. M, & Miley, G. K. 1989, ApJ, 347, 727

Armus, L., et al. 2006, ApJ, 640, 204

Armus, L., et al. 2007, ApJ, 656, 148

Atlee, D. W., & Martini, P. 2012, arXiv:1201.2957v1

Atlee, D. W., Assef, R. J, & Kochanek, C. S. 2009, ApJ, 694, 1539

Bahcall, N. A. 1996, in Astrophysical Quantities, ed. A. Cox (New York: AIP)

Bai, L., Rieke, G. H., Rieke, M. J., Hinz, J. L., Kelly, D. M., & Blaylock, M. 2006, ApJ, 639, 827

Bai, L. et al. 2007, ApJ, 664, 181

Bai, L., Rieke, G. H., & Rieke, M. J. 2007, ApJL, 668, 5

Bai, L., Rieke, G. H., Rieke, M. J., Christlein, D., & Zabludoff, A. I. 2009, ApJ, 693, 1840

Bai, L., Rasmussen, J., Mulchaey, J. S., Dariush, A., Raychaudhury, S., & Ponman, T. J. 2010, ApJ, 713, 637

Baldwin, J. A., Phillips, M. M., & Terlevich, R. 1981, PASP, 93, 5

Balogh, M. L., Morris, S. L., Yee, H. K. C., Carlberg, R. G., & Ellingson, E. 1997, ApJ, 488, 75

Balogh, M. L., Morris, S. L., Yee, H. K. C., Carlberg, R. G., & Ellingson, E. 1999, ApJ, 527, 54

Balogh, M. L., Navarro, J. F., & Morris, S. L. 2000, ApJ, 540, 113

Balogh, M. L., Navarro, J. F., & Morris, S. L. 2000, ApJ, 540, 113

Balogh, M. L., Couch, W. J., Smail, I., Bower, R. G., & Glazebrook, K. 2002, MNRAS, 335, 10

Balogh, M. L., Bower, R. G., Smail, I., Ziegler, B. L., Davies, R. L., Gaztelu, A., & Fritz, A. 2002, MNRAS, 337, 256

Balogh, M. L. et al. 2004, MNRAS, 348, 1355

Balogh, M. L. et al. 2007, MNRAS, 374, 1169

Balogh, M. L. et al. 2009, MNRAS, 398, 754

Balogh, M. L. & McGee, S. L. 2010, MNRAS, 402, 59

Bell, E. F., McIntosh, D. H., Katz, N., & Weinberget, M. D. 2003, ApJS, 149, 289

Bell, E. F. & de Jong, R. S. 2001, ApJ, 550, 212

Beijersbergen, M., Hoekstra, H., van Dokkum, P. G., & van der Hulst, T. 2002, MNRAS, 329, 385

Bigiel, F. et al. 2011, ApJL, 730, 13

Biviano, A. 2000, "Constructing the Universe with Clusters of Galaxies," IAP meeting, ed. F. Durret, & D. Gerbal (Paris)

Biviano, A. & Katgert, P. 2004, A&A, 424, 779

Blain, A. W., Kneib, J.-P., Ivison, R. J., & Smail, I. 1999, ApJ, 512, 87

Blain, A. W., Smail, I., Ivison, R. J., Kneib, J.-P., & Frayer, David T. 2002, PhR, 369, 111

Blanton, M. R. & Roweis, S. 2007, AJ, 133, 734

Boselli, A. et al. 2005, ApJ, 629, 29

Boselli, A. & Gavazzi, G. 2006, PASP, 118, 517

Boselli, A., Boissier, S., Cortese, L., & Gavazzi, G. 2009, Astron. Nach., 330, 904

Bothwell, M. S. et al. 2011, MNRAS, 415, 1815

Bourdin, H. & Mazzotta, P. 2008, A&A, 479, 307

Bower, R. G., Benson, A. J., Malbon, R., Helly, J. C., Frenk, C. S., Baugh, C. M., Cole, S., & Lacey, C. G. 2006, MNRAS, 370, 645

Brand, K., Dey, A., & Weedman, D. et al. 2006, ApJ, 644, 143

Brand, K., et al. 2007, ApJ, 663, 204

Brandl, B. R., et al. 2004, ApJS, 154, 188

Bressan, A., Granato, G. L., & Silva, L. 1998, A&A, 332, 135

Bressan, A. et al. 2006, ApJ, 639, 55

Brinchmann, J., Charlot, S., White, S. D. M, Tremonti, C., Kaufmann, G., Heckman, T. & Brinkmann, J. 2004, MNRAS, 351, 1151

Bruzual, G. & Charlot, S. 2003, MNRAS, 344, 1000

Butcher, H. & Oemler, A., Jr. 1978, ApJ, 219, 18

Byrd, G., & Valtonen, M. 1990, ApJ, 350, 89

Calzetti, D. et al. 2010, ApJ, 714, 1256

Carlberg, R. G., Yee, H. K. C., Morris, S. L., Lin, H., Hall, P. B., Patton, D. R., Sawicki, M., & Shepherd, C. W. 2001, ApJ, 552, 427

Carlberg, R. G., Yee, H. K. C., Morris, S. L., Lin, H., Hall, P. B., Patton, D. R., Sawicki, M., & Shepherd, C. W. 2001, ApJ, 563, 736

Castellano, M. et al. 2011, A&A, 530, 27

Chapman, S., Blain, A., Ivison, R., & Smail, I. 2003, Nature, 422, 695

Chapman, S. C., Blain, A. W., Smail, I., & Ivison, R. J. 2005, ApJ, 622, 772

Charlot, S. & Fall, S. M. 2000, ApJ, 539, 718

Chary, R. & Elbaz, D. 2001, ApJ, 556, 562

Chiosi, C. & Carraro, G. 2002, MNRAS, 335, 335

Christlein, D. & Zabludoff, A. I. 2005, ApJ, 621, 201

Conselice, C. J., Bershady, M. A., & Jangren, A. 2000, ApJ,529, 886

Conselice, C. J., Bershady, M. A., Dickinson, M., & Papovich, C. 2003, AJ, 126, 1183

Cooper, M. C. et al. 2007, MNRAS, 376, 1445

Cortese, L., Gavazzi, G., & Boselli, A. 2008, MNRAS, 390, 1282

Cowie, L. L., & Songaila, A. 1977, Nature, 266, 501

Cucciati, O. et al. 2010, A&A, 524, 2

de Grijp, M. H. K., Lub, J., & Miley, G. K. 1987, A&AS, 70, 95

den Hartog, R. & Katgert, P. 1996, MNRAS, 279, 349

Devereux, N. A. & Hameed, S. 1997, AJ, 113, 599

Devriendt, J. E. G., Guiderdoni, B., & Sadat, R. 1999, A&A, 350, 381.

de Vaucouleurs, G., de Vaucouleurs, A., Corwin, H. G., Jr., Buta, R. J., Paturel, G., & Fouqué, P. 1991, Third Reference Catalogue of Bright Galaxies (New York: Springer) (RC3)

de Vries, W. H., Morganti, R., Röttgering, H. J. A., Vermeulen, R., van Breugel, W., Rengelink, R., & Jarvis, M. J. 2002, AJ, 123, 1784

Dietrich, J. P., Biviano, A., Popesso, P., Zhang, Y.-Y., Lombardi, M. & Böhringer, H. 2009, A&A, 499, 669

Dole, H., et al. 2001, A&A, 372, 364

Donas, J. et al. 2007, ApJS, 173, 597

Donley, J. L., Rieke, G. H., Pérez-Gonzáles, P. G., Rigby, J. R., & Alonso-Herrero, A. 2007 (in press; astro-ph/0612331)

Donley, J. L. et al. 2012, ApJ, 748, 142

Draper, A. R. & Ballantyne, D. R. 2012, ApJ, 753, 37

Dressler, A. 1980, ApJ, 236, 351

Dressler, A., Rigby, J. R., Oemler, A., Fritz, J., Poggianti, B. M., Rieke, G. H., & Bai, L. 2009, ApJ, 693, 140

Dwarakanath, K. S. & Nath, B. B. 2006, ApJL, 653, 9

Edwards, L. O. V. & Fadda, D. 2011, AJ, 142, 148

Egami. E., et al. 2004, ApJS, 154, 130

Eke, V. et al. 2004, MNRAS, 348, 866

Elbaz D., et al. 1999, A&A, 351, 37

Elbaz, D. et al. 2007, A&A, 468, 33

Ellingson, E., Lin, H., Yee, H. K. C., & Carlberg, R. G. 2001, ApJ, 547, 609

Fabricant, D. et al. 2005, PASP, 117, 1411

Farrah, D., Alfonso, J., Efstathiou, A., Rowan-Robinson, M., Fox, M., & Clements, D. 2003, MNRAS, 343, 585.

Fazio, G. G. et al. 2004, ApJS, 154, 10

Finn, R. A. et al. 2010, ApJ, 720, 87

Finoguenov, A. et al. 2009, ApJ, 704, 764

Franceschini, A., Aussel, H., Cesarsky, C. J., Elbaz, D., & Fadda, D. 2001, A&A, 378, 1

Geach, J. E., Smail, I., Moran, S. M., Treu, T., & Ellis, R. S. 2009, ApJ, 691, 783

Geller, M. & Huchra, J. 1983, ApJS, 52, 61

Genzel, R., et al. 1998, ApJ, 498, 579

Gerke, B. F. et al. 2007, MNRAS, 376, 1425

Gilbank, D. G., Baldry, I. K., Balogh, M. L., Glazebrook, K., & Bower, R. G. 2010, MNRAS, 405, 2594

Gómez, P. et al. 2003, ApJ, 584, 210

Gordon, K. D. et al. 2005, PASP, 117, 503

Gordon, K. D. et al. 2007, PASP, 119, 1019

Greggio, L. & Renzini, A. 1990, ApJ, 364, 35

Gruppioni, C., Pozzi, F., & Lari, C. et al. 2005, ApJ, 618, L9

Gunn, J. & Gott, J. 1972, ApJ, 176, 1

Gursky, H., Kellogg, E., Murray, S., Leong, C., Tananbaum, H. & Giacconi, R. 1971, ApJ, 167, 81

Habing, H. J. 1996, A&ARv, 7, 97

Haines, C. P. et al. 2009, ApJ, 704, 126

Hashimoto, Y., Oemler, A., Jr., Lin, H., & Tucker, D. L. 1998, ApJ, 499, 589

Henriksen, M. & Byrd, G. 1996, ApJ, 459, 82

Herschel, F. W. 1785, ”On the Construction of the Heavens,” *Philosophical Transactions of the Royal Society of London*, LXXV, 213.

Hicks, A. K., Mushotzky, R., & Donahue, M. 2010, ApJ, 719, 1844

Hoffer, A. S., Donahue, M., Hicks, A., & Barthelemy, R. S. 2012, ApJS, 199, 23

Hopkins, P. F., Hernquist, L., Cox, T. J., Di Matteo, T., Robertson, B., & Springel, V. 2006, ApJS, 163, 1

Hou, A., Parker, L. C., Harris, W. E., & Wilman, D. J.

Houck, J. R., et al. 2004, ApJS, 154, 18

Houck, J. R., et al. 2005, ApJ, 622, 105

Hubble, E. P. 1926, ApJ, 64, 321

Hubble, E. P. 1929, PNAS, 15, 168

Hubble, E. P. & Humason, M. L., 1931, ApJ, 74, 43

Imanishi, M. & Dudley, C. C. 2000, ApJ, 545, 701

Iovino, A. et al. 2010, A&A, 509, 40

Ivison, R. J., et al. 2004, ApJS, 154, 124

Jannuzi, B. T. & Dey, A. 1999, in ASP Conf. Ser. 191, Photometric Redshifts and the Detection of High Redshift Galaxies, ed. R. J. Weymann et al. (San Francisco: ASP), 111

Johnson, K. E., Hibbard, J. E., Gallagher, S. C., Charlton, J. C., Hornschemeier, A. E., Jarrett, T. H., & Reines, J. A. AJ, 2007, 134, 1522

Just, D., Zaritsky, D., Sand, D. J., Desai, V., & Rudnick, G. 2010, ApJ, 711, 192

Kartaltepe, J. S., Sanders, D. B., & Le Floc'h, E. et al. 2010, ApJ, 721, 98

Kauffmann, G. et al. 2003, MNRAS, 346, 1055

Kauffmann, G. et al. 2004, MNRAS, 353, 713

Kaviraj, S. et al. 2007, ApJS, 173, 619

Kaviraj, S. et al. 2008, MNRAS, 388, 67

Kaviraj, S., Devriendt, J. E. G., Ferreras, I., Yi, S. K., & Silk, J. 2009, A&A, 503, 445

Kawata, D. & Mulchaey, J. S. 2008, ApJ, 672, 103

Kennicutt, R. C., Jr. 1983, AJ, 88, 483

Kennicutt, R. C., Jr. 1983, ApJ, 272, 54

Kennicutt, R. C. 1998, ARA&A, 36, 189

Kennicutt, R. C. et al. 2003, PASP, 115, 928

Kennicutt, R. C. et al. 2009, ApJ, 703, 1672

Kewley, C. A., Heisler, C. A., Dopita, M. A., & Lumsden, S. 2001, ApJS, 132, 37

Kinney, J. D. P, van Gorkom, J. H., & Vollmer, B. 2004, AJ, 127, 3361

Ko, J. et al. 2009, ApJ, 695, 198

Kovač, K. et al. 2010, ApJ, 718, 86

Koyama, Y., Kodama, T., Shimasaku, K., Hayashi, M., Okamura, S., Tanaka, I., & Tokoku, C. 2010, MNRAS, 403, 1611

Kroupa, P. 2001, MNRAS, 322, 231

Lacy, M. et al. 2004, ApJS, 154, 166

Lagache, G., Dole, H., & Puget, J.-L. 2003, MNRAS, 338, 555

Lake, G., Katz, N., & Moore, B. 1998, ApJ, 495, 152

Larson, R. 1974, MNRAS, 166, 585

Larson, R. et al. 1980, ApJ, 237, 692

Laurent, O., Mirabel, I. F., Charmandaris, V., Gallais, P., Madden, S. C., Sauvage, M., Vigroux, L., & Cesarsky, C. 2000, A&A, 359, 887

Le Floc'h, E., Mirabel, I. F., Laurent, O., Charmandaris, V., Gallais, P., Sauvage, M., Vigroux, L., & Cesarsky, C. 2001, A&A, 367, 487

Le Floc'h, E., et al. 2005, ApJ, 632, 169

Le Floc'h, E., et al. 2007, ApJ, 660, 65

Lewis, A. D., Buote, D. A., & Stocke, J. T. 2003, ApJ, 586, 135

Limber, D. N. 1959, ApJ, 130, 414

Lin, H., Yee, H. K. C., Carlberg, R. G., Morris, S. L., Sawicki, M., Patton, D., Wirth, G., & Shepherd, C. W. 1999, ApJ, 518, 533

Loh, Y-S., Ellingson, E., Yee, H. K. C., Gilbank, D. G., Gladders, M. D., & Barrientos, L. F. 2008, ApJ, 680, 214

Longhetti, M. & Saracco, P. 2009, MNRAS, 394, 774

Lutz, D., Spoon, H. W. W., Rigopoulou, D., Moorwood, A. F. M., & Genzel, R. 1998, ApJ, 505, 103

Lutz, D., Valiante, E., Sturm, E., Genzel, R., Tacconi, L. J., Lehnert, M. D., Sternberg, A., & Baker, A. J. 2005, ApJ, 625, 83

Marcillac, D., Rigby, J. R., Rieke, G. H., & Kelly, D. M. 2007, ApJ, 654, 825

Marcillac, D. et al. 2008, ApJ, 675, 1156

Marshall, J. A., Herter, T. L., Armus, L., Charmandaris, V., Spoon, H. W. W., Bernard-Salas, J., & Houck, J. R. 2007, ApJ. (in press; arXiv:0707.2962)

Martig, M., Bournaud, F., Teyssier, R., & Dekel, A. 2009, ApJ, 707, 250

McCarthy, I. G., Frenk, C. S., Font, A. S., Lacey, C. G., Bower, R. G., Mitchell, N. L., Balogh, M. L., & Theuns, T. 2008, MNRAS, 383, 593

McGee, S. L., Balogh, M. L., Henderson, R. D. E., Wilman, D. J., Bower, R. G., Mulchaey, J. S., & Oemler, A., Jr. 2008, MNRAS, 387, 1605

McGee, S. L., Balogh, M. L., Bower, R. G., Font, A. S.,& McCarthy, I. G. 2009, MNRAS, 400, 937

McGee, S. L., Balogh, M. L., Wilman, D. J., Bower, R. G., Mulchaey, J. S. Parker, L. C., & Oemler, A., Jr. 2011, MNRAS, 413, 996

Meekins, J. F., Mushotzky, R. F., Boldt, E. A., Holt, S. S., Marshall, F. E., Pravdo, S. H., & Serlemitsos, P. J. 1971, *Nature*, 231, 107

Merritt, D. 1983, ApJ, 264, 24

Messier, C. 1784, "Catalogue des Nébuleuses & des amas d'Étoiles," *Connoissance des Temps* (Paris).

Melbourne, J., Soifer, B. T., & Desai, V. et al. 2012, AJ, 143, 125

Mihos, J. C. & Hernquist, L. 1996, ApJ, 464, 641

Miller, N. A., Hornschemeier, A. E., Mobasher, B., Bridges, T. J., Hudson, M. J., Marzke, R. O., Smith, R. J. 2009, AJ, 137, 4450

Morgan, W. W., 1961, PNAS, 47, 905

Moss, C. & Whittle, M. 2005, MNRAS, 357, 1337

Moustakas, J., Kennicutt, R. C., Jr., Tremonti, C. A. 2006, ApJ, 642, 775

Mulchaey, J. et al. (in prep)

Narayanan, D., Dey, A., & Hayward, C. C. et al. 2010, MNRAS, 407, 1701

Nardini, E., Risaliti, G., Watabe, Y., Salvati, M., & Sani, E. 2010, MNRAS, 405, 2505

Navarro, J. F., Frenk, C. S., & White, S. D. M. 1996, ApJ, 462, 563

Noeske, K. G. et al. 2007, ApJL, 660, 43

Nolthenius, R. & White, S. D. M. 1987, MNRAS, 235, 505

O'Donnell, J. E., 1994, ApJ, 422, 158

Oemler, A., Jr. 1974, ApJ, 194, 1

Papovich, C. et al. 2006, AJ, 132, 231

Papovich, C., et al. 2007, ApJ, 668, 45

Patel, S. G., Holden, B. P., Kelson, D. D., Illingworth, G. D., & Franx, M. 2009, ApJL, 705, 67

Pearson, C. 2005, MNRAS, 358, 1417

Peng, Y.-j. et al. 2010, ApJ, 721, 193

Pérez-González, et al. 2005, ApJ, 630, 82

Pérez-González, P. G., Trujillo, I., Barro, G., Gallego, J., Zamorano, J., & Conselice, C. J. 2008, ApJ, 687, 50

Petropoulou, V., Vilchez, J., Iglesias-Páramo, J., Papaderos, P., Magrini, L., Cedrés, B. & Reverte, D. 2011, ApJ, 734, 32

Piovan, L., Tantalo, R., & Chiosi, C. 2003, A&A, 408, 559

Plionis, M. & Tovmassian, H. M. 2004, A&A, 416, 441

Poggianti, B. M. et al. 2006, ApJ, 642, 188

Pope, A., et al. 2006, MNRAS, 370, 1185

Popesso, P., Biviano, A., Böhringer, H., & Romaniello, M. 2007, A&A, 461, 397

Postman, M. & Geller M. 1984, ApJ, 281, 95

Quintero, A. D. et al. 2004, ApJ, 602, 190

Rieke, G. H. & Low, F. J. 1972, ApJ, 176, 95

Rieke, G. H., et al. 2004, ApJS, 154, 25

Rieke, G. H., Alonso-Herrero, A., Weiner, B. J., Pérez-Gonzáles, P. G., Blaylock, M., Donley, J. L., & Marcillac, D. 2009, ApJ, 692, 556

Rigby, J. et al. 2008, ApJ, 675, 262

Rujopakarn, W. et al. 2010, ApJ, 718, 1171

Rujopakarn, W., Rieke, G. H., Eisenstein, D. J., & Juneau, S. 2011, ApJ, 726, 93

Salim, S. et al. 2007, ApJS, 173, 267

Sanders, D. B. Soifer, B. T., & Elias, J. H. 1988, ApJ, 325, 74

Sergeant, S., Carramiñana, A., Gonzáles-Solares, E., et al. 2004, MNRAS, 355, 813

Shi, Y., Rieke, G. H., Lotz, J., & Pérez-Gonzáles, P. G. 2009, in prep.

Silva, L., Granato, G. L., Bressan, A., & Danese, L. 1998, ApJ, 509, 103

Silverman, J. D. et al. 2009, ApJ, 695, 171

Simard, L. et al. 2009, A&A, 508, 1141

Sivanandam, S., Rieke, M. J., & Rieke, G. H. 2010, ApJ, 717, 147

Smail, I., Ivison, R. J., & Blain, A. W. 1997, ApJ, 490, 5

Soifer, B. T., Neugebauer, G., & Houck, J. R. 1987, ARA&A, 25, 187

Spinoglio, L., Malkan, M. A., Smith, H. A., González-Alfonso, E., & Fischer, J. 2005, ApJ, 623, 123

Spitzer, L. Jr., & Baade, W. 1951, ApJ, 113, 413

Spoon, H. W. W., Keane, J. V., Tielens, A. G. G. M., Lutz, D., & Moorwood, A. F. M. 2001, A&A, 365, 353

Spoon, H. W. W., et al. 2004, ApJS, 154, 184

Stansberry, J. A., et al. 2007, PASP, 119, 1038

Stern, D. et al. 2005, ApJ, 631, 163

Stetson, P. B. 1987, PASP, 99, 191

Sturm, E., Verma, A., & Graci-Carpio, J. et al. 2010, A&A, 518, L36

Temi, P., Brighenti, F., & Mathews, W. G. 2007, ApJ, 660, 1215

Temi, P., Brighenti, F., & Mathews, W. G. 2009, ApJ, 707, 890

Tempel, E., Saar, E., Liivamägi, L. J., Tamm, A., Einasto, J., Einasto, M., & Müller, V. 2011, A&A, 529, A53

Tomczak, A. R., Tran, K.-V. H., & Saintonge, A. 2011, ApJ, 738, 65

Tran, Q. D., et al. 2001, ApJ, 552, 527

Tran, K.-V. H., Saintonge, A., Moustakas, J., Bai, L., Gonzalez, A. H., Holden, B. P., Zaritsky, D., & Kautsch, S. J. 2009, ApJ, 705, 809

Tully, R. B. 1989, Nearby Galaxies Catalog (Cambridge University Press, Cambridge)

Tyler, K. D. et al. 2011, ApJ, 738, 56

Tyler, K. D., Rieke, G. H., & Bai, L. 2013, in prep.

van den Bergh, S. 1976, ApJ, 206, 883

van der Wel, A., Franx, M., Illingworth, G. D., & van Dokkum, P. G. 2007, ApJ, 666, 863

Veilleux, S., Kim, D.-C., & Sanders, D. B. 2002, ApJS, 143, 315

Vikhlinin, A., Markevitch, M., Murray, S. S., Jones, C., Forman, W., & Van Speybroeck, L. 2005, ApJ, 628, 655

Vulcani, B., Poggianti, B. M., Finn, R. A., Rudnick, G., Desai, V., & Bamford, S. 2010, ApJL, 710, 1

Weedman, D. W., et al. 2005, ApJ, 633, 706

Weedman, D. W., et al. 2006, ApJ, 651, 101

Werner, M. W., et al. 2004, ApJS, 154, 1

Whitmore, B. C., Gilmore, D. M., & Jones, C. 1993, ApJ, 407, 489

Wilman, D. J., Balogh, M. L., Bower, R. G.,Mulchaey, J. S., Oemler, A., Jr., Carlberg, R. G., Morris, S. L., & Whitaker, R. J. 2005, MNRAS, 358, 71

Wilman, D. J., et al. 2005, MNRAS, 358, 88

Wilman, D. J. et al. 2008, ApJ, 680, 1009

Wilman, D. J. et al. 2009, ApJ, 692, 298

Yan, L., et al. 2005, ApJ, 628, 604

Yee, H. K. C. et al. 2000, ApJS, 129, 475

Yi, S. K. et al. 2005, ApJ, 619, 111

Yumi, C., Goto, T., & Yoon, S.-J. 2009, MNRAS, 395, 637

Zabludoff, A. I. & Mulchaey, J. S. 1998, ApJ, 496, 39

Zabludoff, A. I. & Mulchaey, J. S. 2000, ApJ, 539, 136

Zhu, Y.-N., Wu, H., Cao, C., & Li, H.-N. 2008, ApJ, 686, 155

Zwicky, F. 1933, AcHPh, 6, 110